UNIVERSIDADE ESTADUAL DE CAMPINAS
Instituto de Física Gleb Wataghin

DANELISE DE OLIVEIRA FRANCO

SEARCH FOR POINT SOURCES OF NEUTRONS IN THE DATA OF THE PIERRE AUGER OBSERVATORY

PROCURA POR FONTES PONTUAIS DE NÊUTRONS EM DADOS DO OBSERVATÓRIO PIERRE AUGER

CAMPINAS
2023

DANELISE DE OLIVEIRA FRANCO

SEARCH FOR POINT SOURCES OF NEUTRONS IN THE DATA OF THE PIERRE AUGER OBSERVATORY

PROCURA POR FONTES PONTUAIS DE NÊUTRONS EM DADOS DO OBSERVATÓRIO PIERRE AUGER

Thesis presented to the Gleb Wataghin Institute of Physics of the State University of Campinas in partial fulfillment of the requirements for the degree of DOCTOR OF SCIENCE, in the area of PHYSICS.

Tese apresentada ao Instituto de Física Gleb Wataghin da Universidade Estadual de Campinas como parte dos requisitos exigidos para a obtenção do título de DOUTORA EM CIÊNCIAS, na Área de FÍSICA.

Supervisor: CAROLA DOBRIGKEIT CHINELLATO

ESTE TRABALHO CORRESPONDE À VERSÃO FINAL DA TESE DEFENDIDA PELA ALUNA DANELISE DE OLIVEIRA FRANCO E ORIENTADA PELA PROFA. DRA. CAROLA DOBRIGKEIT CHINELLATO.

CAMPINAS
2023

Ficha catalográfica
Universidade Estadual de Campinas
Biblioteca do Instituto de Física Gleb Wataghin
Lucimeire de Oliveira Silva da Rocha - CRB 8/9174

F848s

Franco, Danelise de Oliveira, 1994-
Search for point sources of neutrons in the data of the Pierre Auger Observatory / Danelise de Oliveira Franco. – Campinas, SP : [s.n.], 2023.

Orientador: Carola Dobrigkeit Chinellato.
Tese (doutorado) – Universidade Estadual de Campinas, Instituto de Física Gleb Wataghin.

1. Raios cósmicos. 2. Nêutrons. 3. Astrofísica. I. Chinellato, Carola Dobrigkeit, 1952-. II. Universidade Estadual de Campinas. Instituto de Física Gleb Wataghin. III. Título.

Informações Complementares

Título em outro idioma: Procura por fontes pontuais de nêutrons em dados do Observatório Pierre Auger
Palavras-chave em inglês:
Cosmic rays
Neutrons
Astrophysics
Área de concentração: Física
Titulação: Doutora em Ciências
Banca examinadora:
Carola Dobrigkeit Chinellato [Orientador]
Flávia Sobreira
Rogerio Menezes de Almeida
Aion da Escóssia Melo Viana
Pedro Cunha de Holanda
Data de defesa: 28-08-2023
Programa de Pós-Graduação: Física

Identificação e informações acadêmicas do(a) aluno(a)
- ORCID do autor: https://orcid.org/0000-0002-8435-7730
- Currículo Lattes do autor: https://lattes.cnpq.br/8415900368372228

INSTITUTO DE FÍSICA
GLEB WATAGHIN

MEMBROS DA COMISSÃO EXAMINADORA DA TESE DE DOUTORADO DA ALUNA DANELISE DE OLIVEIRA FRANCO - RA 164186, APRESENTADA E APROVADA AO INSTITUTO DE FÍSICA GLEB WATAGHIN, DA UNIVERSIDADE ESTADUAL DE CAMPINAS, EM 28/08/2023.

COMISSÃO JULGADORA:

- Profa. Dra. Carola Dobrigkeit Chinellato – Presidente e orientadora (IFGW/UNICAMP)

- Profa. Dra. Flávia Sobreira (IFGW/UNICAMP)

- Prof. Dr. Rogerio Menezes de Almeida (Universidade Federal Fluminense)

- Prof. Dr. Aion da Escóssia Melo Viana (USP – Universidade de São Paulo)

- Prof. Dr. Pedro Cunha de Holanda (IFGW/UNICAMP)

OBS.: Ata da defesa com as respectivas assinaturas dos membros encontra-se no SIGA/Sistema de Fluxo de Dissertação/Tese e na Secretaria do Programa da Unidade.

CAMPINAS

2023

Life need not be easy, provided only that it is not empty.

(Lise Meitner)

ACKNOWLEDGMENTS

I'm grateful to Professor Carola for all these years working together and for all the lessons, corrections, suggestions, and insights. She was a fundamental part of my formation not only as a researcher but as a human being. I want to thank her for always having patience with me and always having kind words to light the path. I'm grateful for her support and encouragement, which allowed me to finish this work. She always believed I could go farther and gave me the tools to do it. Most of all, I want to thank her for always inspiring me and being a role model as a woman and a scientist.

I want to thank Dr. Lorenzo Caccianiga for the collaboration that allowed me to finish this project and for inspiring me as a physicist. I'm grateful to Federico for a great partnership that improved my research in many different ways. I also want to thank Claudio for all the insightful conversations about physics, the universe, and much more. I'm grateful for my time with these three astounding people who made this journey a little lighter.

I cannot talk about acknowledgments without talking about my wonderful husband, Luis. He supported me every day along this path. His love and companionship allowed me to surpass all obstacles and overcome all challenges. I want to thank him for all the ideas that allowed me to finish this thesis. His teachings made me not only a better researcher but a better human. I'm grateful for all the conversations I had with him, for all the suggestions he made, for all the times he listened to me (even after a long day of work), and for the computational help he provided me during all these years. This work would not be the same without him. Above all, I want to thank him for making this journey easier, lighter, and a lot more fun.

I want to thank all my family members, especially my parents, Sonia and Zuriel. They gave me the structure I needed to pursue all my dreams. I carry with me all their teachings that allow me to make the proper decisions in life. Their support allowed me to go farther than I could ever imagine. The best gift they gave me was my sister, Alessandra. I'm thankful to have her in my life. I learned from her since the day she was born. I'm grateful for her companionship and her good sense of humor that lights up my days.

I want to thank Pedro and Gabriela for their friendship. During the difficult period caused by the pandemic, they made me believe we always have better days ahead of us. I want to thank Hitalo for continuously inspiring me to improve as a person and a researcher and William for all the delicious dishes he prepared for me and all the good times we had together. Talking with them almost daily gave me the structure to keep going. I want to thank Rafaela for being one of the most reasonable persons I know and always saying the right thing. I want to thank Paulinho for all the cups of coffee he gave me, allowing me to

work happily. I was lucky enough to have only incredible people by my side. It is impossible to mention all my friends here, but I'm grateful to each one of them. Their love and support allowed me to finish this work.

During the time I was developing this work, I had the opportunity to meet many marvelous scientists. I'm grateful for all the learning and inspiration I got from them. I want to thank especially Dra. Geraldina Golup and Professor Paul Sommers. They helped me in the development of this work. Their assistance was essential for the final result of this project.

This work was carried out with the support of "Ministry of Science, Technology and Innovation" and the "National Council for Scientific and Technological Development – CNPq", Proc. 140552/2018-9. This study was financed in part by the Coordenação de Aperfeiçoamento de Pessoal de Nível Superior - Brasil (CAPES) - Finance Code 001, as well as by CAPES/PRINT/DSE Proc. 88887.512347/2020-00.

RESUMO

Desde as primeiras medidas de raios cósmicos ultraenergéticos, várias colaborações estudaram suas distribuições de direções de chegada na tentativa de revelar a sua origem. Estudar partículas neutras é uma ferramenta interessante para determinar as fontes de raios cósmicos ultraenergéticos. Dado que elas não são defletidas por campos magnéticos, as suas direções de chegada preservam informação sobre a sua origem. Neste estudo, nós focamos no nêutron, um hádron que produz um chuveiro atmosférico indistinguível de um gerado por um próton. Já que somos incapazes de distinguir os chuveiros atmosféricos produzidos por estas duas partículas, nós identificamos um fluxo de nêutrons baseado em um excesso de eventos em torno da direção do alvo.

O Observatório Pierre Auger é o maior experimento de raios cósmicos do mundo. A sua configuração permite o estudo de raios cósmicos ultraenergéticos com energias a partir de 10^{17} eV. Os raios cósmicos primários interagem no topo da atmosfera, produzindo chuveiros atmosféricos. As partículas secundárias resultantes do desenvolvimento do chuveiro atmosférico são detectadas no nível do solo usando principalmente dois tipos de detectores: o detector de superfície e o detector de fluorescência.

Neste trabalho, usamos dados de chuveiros atmosféricos detectados no Observatório Pierre Auger para investigar fluxos de nêutrons vindos de direções pontuais do céu usando eventos detectados pelo detector de superfície. Investigamos todo o céu dentro do campo de visão do Observatório, pixelizando o céu para definir as direções dos alvos e procurando por excessos de eventos em pequenas regiões em torno destas direções que podem indicar um fluxo de nêutrons. Ademais, restringimos a procura olhando para direções específicas do céu onde existem fontes candidatas conhecidas. As fontes candidatas são objetos de interesse astrofísico, principalmente emissores de raios-γ, como pulsares, magnetares e microquasares. A região do Centro Galáctico também foi estudada devido ao interesse pelo buraco negro supermassivo central Sagitário A*. Também propomos um novo método para a procura de fontes pontuais de nêutrons, designando um peso para cada raio cósmico reconstruído, representando a densidade de probabilidade deste evento vir da direção da fonte candidata. Simulamos conjuntos de dados usando a técnica do embaralhamento para determinar a contribuição do sinal de fundo. Usando esta técnica, preservamos a exposição do Observatório ao mesmo tempo que apagamos qualquer anisotropia local. Procuramos por excessos de eventos comparando o sinal observado com a contribuição do sinal de fundo. Embora não encontremos evidências de um excesso significativo de eventos que possam indicar um fluxo de nêutrons provenientes de qualquer alvo testado, nós estabelecemos o limite superior para o fluxo de nêutrons em cada caso investigado.

ABSTRACT

Since the first measurements of ultra-high-energy cosmic rays, several collaborations have explored their arrival direction distribution to reveal their origin. Studying neutral particles is a compelling tool to determine sources of ultra-high-energy cosmic rays. Since they are not deflected by magnetic fields, their arrival directions preserve information about their origin. In this study, we focused on the neutron, a hadron that produces an air shower indistinguishable from one generated by a proton. Since we cannot distinguish air showers produced by these two particles, we identify a neutron flux based on an excess of events around the direction of the target.

The Pierre Auger Observatory is the world's largest cosmic ray experiment facility. Its design allows the study of ultra-high-energy cosmic rays with energies above 10^{17} eV. The primary cosmic rays interact at the top of the atmosphere, producing air showers. The secondary particles resulting from the air shower development are detected at the ground level using mainly two types of detector: the surface detector and the fluorescence detector.

In this work, we use data from air showers detected at the Pierre Auger Observatory to investigate neutron fluxes coming from point directions of the sky using events recorded by the surface detector. We search the whole sky within the field of view of the Observatory, pixelating the sky to define the direction of the targets and looking for excesses of events in small regions around these directions that could indicate a neutron flux. We narrow the search by looking for specific directions of the sky where known candidate sources lie. The candidate sources are objects of astrophysical interest, mainly γ-ray emitters such as pulsars, magnetars, and microquasars. We also investigate the Galactic center region due to the interest in the central supermassive black hole Sagittarius A^*. We propose a new method to search for point sources of neutrons, assigning a weight to each reconstructed cosmic ray representing the probability density of this event coming from the direction of the candidate source. We simulate data sets using the scrambling technique to determine the background contribution. Using this technique, we preserve the exposure of the Observatory while erasing any local anisotropies. We search for event excesses by comparing the observed signal with the background contribution. Even though we do not find evidence of a significant excess of events that could indicate a neutron flux from any tested target, we establish the upper limit for the neutron flux in each investigated case.

List of Figures

List of Tables

CONTENTS

1 INTRODUCTION

Cosmic rays are composed mostly of charged particles traveling through space. They can have energies from 10^9 eV up to 10^{21} eV. Neutral particles, such as photons, neutral pions, and neutrons, can be produced in decays or other interactions of charged particles. We expect the production of ultra-high-energy protons to be accompanied by the production of neutrons due to pion photo-production and nuclear interactions near the source. Since neutrons do not have an electric charge, they travel in straight lines, producing an excess of events around the direction of their sources. Hence, neutrons can be used as a messenger to identify sources of cosmic rays in the EeV range. As their primary interactions are hadronic, we are unable to differentiate between an air shower initiated by a proton and one initiated by a neutron. Therefore, we identify a neutron flux through an excess of air showers coming from a direction in the sky.

This work includes three methods to search for point sources of neutrons in the EeV range. We use data from cosmic rays detected at the Pierre Auger Observatory. The first method is a blind search, in which we search for neutron fluxes in target regions covering the sky within the field of view accessed using each data set. The other two methods are targeted searches, in which we look for excesses around the direction of candidate sources.

The Pierre Auger Observatory is the largest cosmic ray facility in the world designed to study ultra-high-energy cosmic rays, i.e., those with energies above 10^{17} eV. The study of such energetic particles impacts several areas of astrophysics. Data collected in the Observatory help to unravel their acceleration mechanisms, origin, propagation, and composition. We present the details about the Observatory in Chapter 3.

The main topic of this work is the sources of ultra-high-energy cosmic rays. We study the distribution of the arrival directions of cosmic rays, searching for candidate sources of neutral particles in this energy range. A flux of ultra-high-energy neutral particles would identify a source of ultra-high-energy cosmic rays.

Neutrons, although unstable through β-decay, can travel long distances when they reach ultra-high energies. For energies above 1 EeV (1 EeV $\equiv 1 \times 10^{18}$ eV), neutrons can travel distances longer than the distance to the Galactic center. Due to the neutron instability, we focused on Galactic candidate sources.

The Pierre Auger Collaboration has published two works about the search for point sources of neutrons. The first one, published in 2012 [1], presented results of a blind search method. In this paper, the sky was pixelized to define target directions covering the field of view of the Observatory. The other work was published in 2014 [2] and presented a targeted search method. The targets are astrophysical objects that are candidates to produce

ultra-high-energy cosmic rays. In this thesis, we update the results of these two methods using new data sets and candidate sources. We also propose a new strategy to search for point sources of neutrons.

In the next chapter, we present the main aspects of cosmic rays, such as the energy spectrum, composition, and air shower development. We discuss the most relevant effects of the study of ultra-high-energy cosmic rays and the main experiments that preceded the Pierre Auger Observatory. In Chapter 3, we will describe the Observatory, presenting details about the detectors used and the event reconstruction.

In Chapter 4, we describe the data sets used to produce the results presented in this thesis, followed by a discussion about the role of the neutron in the astroparticle physics scenario in Chapter 5. The first method, discussed in Chapter 6, is a blind search for point sources of neutrons. We present the results of this method in Chapter 7. For this first method, we explain how to define the target directions and the size of the target regions using a top-hat function. Since we are searching for an excess of events that could identify a neutron flux, we compare the observed number of events inside a target region with the expected signal from the background. We explain how to estimate the background signal using the recorded data set, preserving the exposure of the Observatory. Finally, we explain how we can estimate an upper limit of the neutron flux.

The targeted search is similar to the blind search. However, in this approach, we consider only specific directions where we know that candidate sources of ultra-high-energy cosmic rays lie. In Chapter 8, we describe the classes of astrophysical objects used in our search and discuss the details of the targeted search. The target sets include different types of pulsars, microquasars, and magnetars. We also investigate the Galactic center region and the Galactic plane as possible locations of neutron sources. We present the results of the targeted search in Chapter 9.

In Chapter 10, we propose a new method for the search of point sources of neutrons. Instead of using a top-hat function to limit a region in the sky, we define a weight that represents the probability density of an event coming from a specific direction of a target. This technique allows us to estimate the air shower density at the position of the target. Using simulations to estimate the background signal, we determine the significance of each candidate source. In addition, we stipulate an upper limit on the neutron flux for each target. We present the results of this method in Chapter 11. We present the final discussions and conclusions in Chapter 12.

The previous works published by the Collaboration [1, 2] studied vertical events. A vertical event has a zenith angle less than 60°, while an inclined event has a zenith angle between 60° and 80°. Our goal is to study the updated vertical data set, adding nine more years of observation, besides analyzing two new data sets: one composed of inclined events and the other of events recorded by the infilled array. We apply the methods presented in Chapters 8 and 10 on an updated version of the catalogs used in [2].

2 COSMIC RAYS

The origin of cosmic rays is one of the main questions since its discovery in 1912. They are ionized nuclei, mostly protons. Even though most cosmic rays have energy comparable to their masses, a small fraction has ultra-relativistic energies up to 10^{20} eV. Cosmic rays above 10^{17} eV are particularly interesting for astroparticle physics. In this work, we focus on particles in this energy range.

In this chapter, we discuss the most relevant aspects of cosmic rays, including their energy spectrum and composition. The energy spectrum covers over 12 decades of energy and presents important features at specific energy values. The most energetic cosmic rays, above 10^{15} eV, produce air showers that reach the ground. We discuss the most relevant aspects of air showers in Section 2.3. We discuss two relevant effects when studying ultra-high-energy cosmic rays: the GKZ effect and the Cherenkov effect. Lastly, we shortly describe the main experiments that preceded the Pierre Auger Observatory.

2.1 Introduction

Wilhelm Röntgen discovered X-rays in 1895 while studying a new kind of penetrating radiation [3]. He was investigating cathode rays when he realized that, even when covered with dark cardboard, the tube was able to emit radiation that produced a faint glow on a fluorescent screen. Due to the unknown nature of this radiation, he named them X-rays. The X-rays were more penetrating than cathode rays since they were not blocked by bodies opaque to visible light. Röntgen's discovery propelled the search for new sources of X-radiation. One of the scientists investigating new sources of X-rays was the French physicist Antoine Henri Becquerel. He discovered the natural radioactivity when studying samples of potassium uranyl disulphate (a uranium salt) in 1896 [4]. In 1899, the New Zealand physicist Ernest Rutherford demonstrated the existence of at least two types of radiation. He coined the terms α and β radiation [5]. The α-particles are composed of two protons and two neutrons and are the result of the decay of heavy nuclei such as uranium or plutonium. The β-radiation are electrons produced from radioactive decay. In 1900, Paul U. Villard discovered the γ-radiation [6]. The γ-radiation consists of energetic photons produced in nuclear decay without altering the number of protons or neutrons in the nuclei. At the beginning of the 1900s, it was known that these three types of radiation could ionize atoms.

Electroscopes are devices projected to study electric charges in a body or a medium using Coulomb's law. One version of the electroscope is a device with two metal leaves, usually gold, a metal rod, and a disk. An electrically charged body touching the disk induces

a charge accumulation in the metal leaves, causing a Coulomb repulsion that pushes the leaves apart. In the early 1900s, it was noticed that charged electroscopes discharged even when hidden from light and natural radioactivity sources, indicating the presence of some kind of ionizing radiation. Some scientists described this phenomenon, such as Charles T. R. Wilson in [7].

Trying to prove that the radiation was coming from the ores on the Earth's surface, Theodor Wulf made measurements in 1910 using an electroscope at the top of the Eiffel Tower. He found out that the measured ionization intensity decreased. However, the decrease was smaller than expected, going from 6×10^6 ions/m^3 at the ground level to 3.5×10^6 ions/m^3 at the top of the tower [8]. Since γ-rays were the most penetrating radiation known at the time, if the radiation was coming from the surface of the Earth, he should not measure any considerable ionization at this altitude. Two years later, Victor Hess made measurements in altitudes up to 5 km, using hydrogen-filled balloons that showed the intensity increasing above a certain height [9]. Due to the observed increase, he concluded correctly that the origin of this radiation was extraterrestrial.

Werner Heinrich Gustav Kolhörster made significant advances in the cosmic ray field. Kolhörster flew to higher altitudes than Hess, exceeding 9 km above sea level [10]. He also measured an increase of the ionization with altitude, apparently confirming the results obtained by Hess. Kolhörster and Walter Bothe demonstrated that cosmic rays were charged particles [11] using Geiger-Müller detectors [12].

Robert Millikan coined the term cosmic rays [13]. He made remarkable contributions to the measuring underwater technique. Millikan tried to study cosmic rays by measuring particles underwater in lakes inside mines. The thickness of the whole atmosphere corresponds to around 10 m of water. Millikan's results did not help him to disprove Kolhörster's measurements. Nowadays, it is easy to understand why the results from the two experiments were different: they measured distinct air shower components. Hess and Kolhörster detected the electromagnetic component in the atmosphere. On the other hand, underwater, Millikan measured the more penetrating component: the muonic one.

The invention of Geiger-Müller counters was also important for the first measurements of the secondary particles produced in the collision of the primary cosmic ray with molecules in the air. These particle cascades resulting from the interaction of the primary particle with the atmosphere receive the name of air showers. We discuss the most important characteristics of air showers in Section 2.3. In 1933, Bruno Rossi observed an increase of coincidences in a triangular Geiger-counter array when he placed a piece of a few centimeters of lead above the detectors, concluding that this increase was caused by cosmic particles interacting with the material and producing secondary particles [14]. A decrease in the coincidence rate happened by increasing the thickness of the material. Later, this result was known as *Rossi's transition curve*. One year later, in 1934, Rossi [15] found evidence of a correlation in the arrival times of particles in widely spread detectors and named

this phenomenon *sciami* (swarms in Italian). Schmeiser and Bothe noted that Rossi's transition curve implied the existence of cascades in the air [16]. They named this phenomenon *Luftschauer* (air shower, in German). The discovery of air showers is officially attributed to Pierre Auger and his collaborators [17], when they found coincidences in detectors spread about 300 m from each other.

Hess and Kolhörster's measurements in balloon flights pointed to an increase in the ionization of the air with the altitude. From these experiments, they concluded that the radiation was coming from outer space. This conclusion was correct. However, they were observing the development of air showers in the atmosphere. They were detecting the secondary particles produced from the primary cosmic rays. There is a point in the atmosphere where air showers begin to develop. Consequently, at altitudes higher than this point, secondary particles are absent. Since there are only the primary particles, the particle flux decreases. This point is known as the Regener-Pfotzer maximum or Pfotzer maximum [18]. It occurs around 20 km above sea level. In the 1940s, it was possible to determine the type of the primary particle using measurements with balloons at high altitudes. These direct measurements at the top of the atmosphere are only possible for low-energy cosmic rays since their flux decreases with energy, as we discuss in the next section. Marcel Schein showed that the positively charged primary particles were mostly protons [19].

Since its discovery, numerous experiments have been designed to investigate the properties of cosmic rays, which play a vital role in both particle physics and astrophysics. Many particles have been discovered through cosmic ray observations. For instance, the positron, the electron's antiparticle, was discovered in 1932 by Carl David Anderson, who used track photographs from a cloud chamber [20]. Similarly, in 1937, Anderson and Neddermeyer discovered the muon through observations of cosmic rays [21]. Cosmic ray observations also led to the discovery of the pion by César Lattes *et al.* [22]. The kaon, the first strange particle detected, was discovered as a secondary particle produced in an air shower by Clifford Butler and George Rochester in 1947 [23]. Additionally, the lambda baryon was discovered in 1950 through observations of cosmic ray air showers [24].

In recent years, experiments such as the Telescope Array and the Pierre Auger Observatory contributed to various fields of astrophysics. The arrival direction distribution can link cosmic rays with astrophysical sources. The Pierre Auger Collaboration recently published a study of the arrival direction distribution of cosmic rays at ultra-high energies [25]. Several works were published investigating the connection between neutral particles and sources of ultra-high-energy cosmic rays. Among the studied particles, we can cite neutrinos [26], neutrons [1, 2], and photons [27–29]. The study of the distribution of arrival directions proved the existence of a dipolar anisotropy pointing around 125° from the Galactic center. This discovery is evidence that the origin of ultra-high-energy cosmic rays can be extragalactic [30]. Cosmic rays can also be used in multi-messenger astronomy, as made in [31].

One intriguing characteristic of cosmic rays is their wide-ranging energy spectrum, covering around 12 decades of energy. Their differential flux decreases with energy, approximately following a power law. The index that describes this power law changes at some points. We discuss these changes in the spectral index and other relevant aspects of the cosmic ray energy spectrum in the next section.

2.2 Energy Spectrum

Cosmic rays cover a vast energy spectrum range, with primary particles going from around 10^9 eV to more than 10^{20} eV. The spectrum shape follows a power law in which the index depends on the energy. The different parts of the spectrum where the spectrum index changes receive specific names: the *knee* and the *ankle* features. Another change in the index occurs between these two features and is named the *second knee* or *iron knee*.

At GeV energies, the flux is greater than 1,000 particles per second and per square meter. However, as energy levels increase to PeV (1 PeV $\equiv 10^{15}$ eV), the flux decreases significantly to approximately one particle per square meter per year. At even higher energies, above 100 EeV, the flux drops even further to less than one particle per square kilometer per century [32].

The spectrum can be described as a power law in which the index changes with energy. The particle flux is proportional to $E^{-\gamma}$. At energies below several PeV, the spectral index is approximately 2.7. At the knee feature, the spectral index becomes steeper, around 3.1 [33]. At higher energies, a second knee is observed, resulting in a further steepening of the spectrum. At the ankle, the spectrum flattens again. Finally, around 4.6×10^{19} eV, a suppression is observed, where the spectrum index is around 5.1 [34].

Particles with low energy, below 1 GeV (1 GeV $\equiv 10^9$ eV), are sensitive to the solar wind. This phenomenon is known as solar modulation. There is an anti-correlation between the solar activity and the cosmic ray flux. During periods of intense solar activity, the cosmic ray flux decreases and vice versa [35]. Above this energy, this effect is suppressed.

The knee feature occurs around $10^{15.5}$ eV. This characteristic is a spectrum index change mentioned for the first time in [36]. In [37], the authors suggested that the knee feature can be fully explained by propagation effects in the Galaxy. The appearance of a knee in the all-particle energy spectrum can be attributed to a break in the spectra for lighter elements. Hence, this results in an increase in the average mass of cosmic rays around this energy. One prevalent hypothesis for the origin of the knee suggests that the spectra at the source experience a break [32].

The ankle feature occurs around $10^{18.5}$ eV. The most accepted explanation is that, at this energy, we are observing the transition from the Galactic to the extragalactic component of cosmic rays. The ankle was first suggested by Linsley [38], being later confirmed by the experiments such as the Haverah Park array [39] and the Fly's Eye experiment [40]. An-

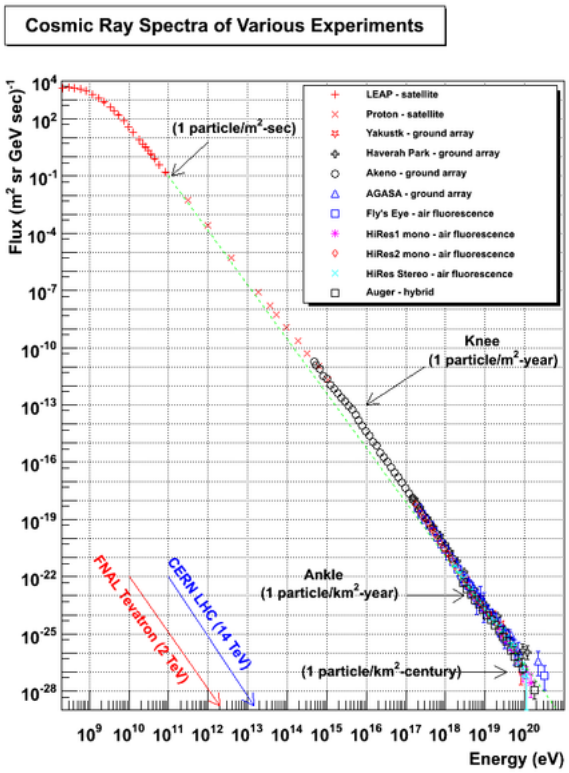

Figure 2.1: Cosmic ray spectra measured from various experiments. Figure extracted from [50].

other explanation for the ankle is the dip-model of the ankle. This model explains the ankle as an imprint of protons under electron-positron pair production in the Cosmic Microwave Background (CMB) [41]:

$$p + \gamma_{\text{CMB}} \rightarrow p + e^- + e^+. \tag{2.1}$$

Figure 2.1 shows a compilation of the cosmic ray spectrum as measured by several experiments. The information was extracted from these experiments: LEAP (Low Energy Antiproton) experiment [42], Proton satellite [43], Yakutsk Extensive Air Shower Array [44], Haverah Park [39], AGASA (Akeno Giant Air Shower Array) [45], Fly's Eye [46], HiRes (High Resolution Fly's Eye) [47], and the Pierre Auger Observatory [48, 49]. This compilation was made by William Hanlon, and it is available at [50].

The Pierre Auger Collaboration investigates the end of the cosmic ray energy spectrum [34, 51–54]. The characteristic of the second knee or iron knee is a bending in the spectrum that occurs around $10^{16.9}$ eV. Studies suggested that the composition of cosmic rays becomes heavier at the end of the spectrum, above the knee feature. Since low-energy cosmic rays are predominantly composed of light elements, this would imply that heavier elements up to iron are more accelerated. The second knee may also indicate that magnetic fields can no longer confine protons at high energies, leading to an escape of these protons that will not reach the Earth.

As shown in Figure 2.2, we have the ankle region around 5×10^{18} eV, and around a

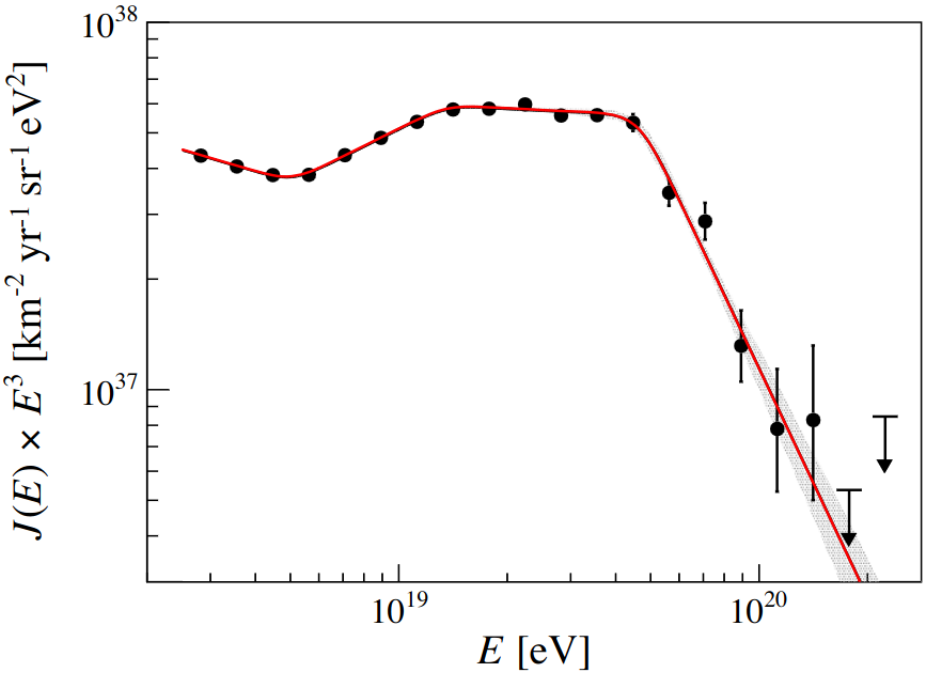

Figure 2.2: Cosmic ray spectrum for energies above 2.5×10^{18} eV. Figure extracted from [34].

decade further, we have the beginning of the suppression region. In this figure, the curve and the experimental data are multiplied by E^3 to highlight the features of the energy spectrum. More details about the spectrum for energies above 10^{17} eV are presented in Section 7.2.

2.3 Air showers

When a cosmic ray penetrates the atmosphere and collides with a molecule in the air, it initiates a cascade of particles produced by various interactions. Different types of primary cosmic rays create distinct air shower profiles. Neutrons and protons generate indistinguishable air showers because the main interactions at the beginning of the development are hadronic.

When the primary particle has enough energy, around above 10^{15} eV, the air shower can reach the ground level. In this case, it is an extensive air shower. Pierre Auger and other collaborators discovered extensive air showers in 1939 [17]. The low-energy cosmic ray flux is large enough to enable measurements at the top of the atmosphere. However, for energies above 10^{15} eV, experiments with detector arrays at the ground level are used to measure the development of the air showers due to the difficulties of directly measuring the events. ISS-CREAM (Cosmic Ray Energetics And Mass for the International Space Station) [55] is an example of a detector built to detect primary cosmic rays. On the other hand, the Telescope Array and the Pierre Auger observatories measure the secondary particles produced in extensive air showers.

Many interactions can take place during the air shower development. Electromagnetic and hadronic interactions are dominant. The number of secondary particles pro-

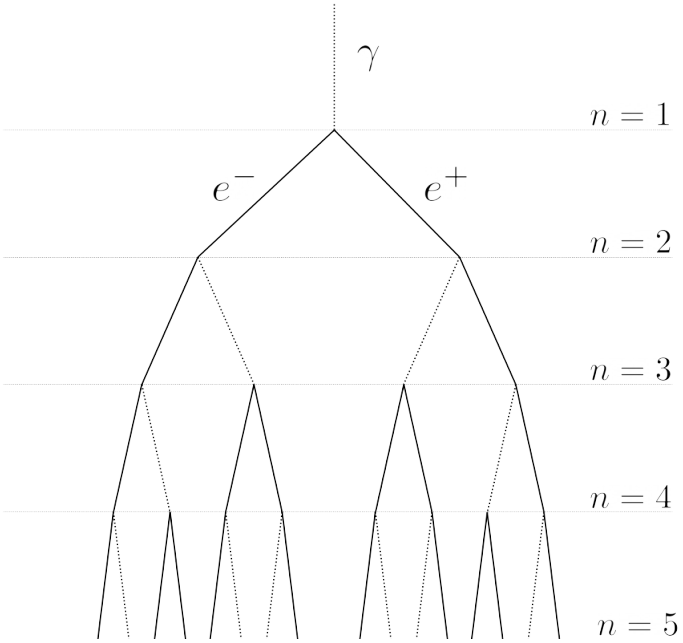

Figure 2.3: Heitler's toy model. Photons undergo electron-positron pair production and electrons/positrons produce photons via Bremsstrahlung.

duced in the air shower depends on the primary particle's energy. Ultra-high-energy primary particles can leave a footprint of around 25 km^2 at ground level [56].

A high-energy photon that decays into an electron-positron pair can initiate an electromagnetic cascade when each one of the leptons generates high-energy photons, and so on. The process will occur while the particles have enough energy to produce the next generation. Usually, air showers initiated by photons have a small fraction of muons. The muon deficiency can help distinguish an electromagnetic from a hadronic shower originated by a proton or a neutron. Heitler's model [57] is a simple way to understand electromagnetic air shower development. In this model, particles decay in pairs via two interactions: electron-positron pair production from a photon or one-photon production via Bremsstrahlung. A scheme of Heitler's model is presented in Figure 2.3. After n interactions, the shower has 2^n particles.

Hadronic interactions are the most relevant when studying cosmic rays since most of them are protons. When a proton with sufficient energy penetrates the atmosphere and collides with a nitrogen molecule present in the air, many pions are produced in the collision. Neutral pions decay into photon pairs that start an electromagnetic shower via electron-positron pair production, as explained above. Neutral pions have short lifetimes, having a mean life of 8.43×10^{-17} s [58]. Charged pions can decay into muons, which then can decay into electrons. High-energy muons can penetrate deeper into the atmosphere since they do not present nuclear interactions and have a small ionization loss, allowing their detection at ground level. The charged pions decay into muons via these processes:

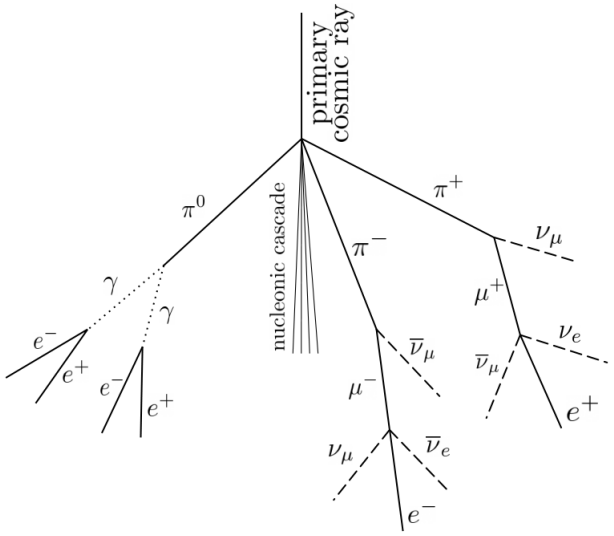

Figure 2.4: A nucleonic shower example. The primary proton produces pions after colliding with a molecule in the air. Neutral pions generate an electromagnetic cascade, while the charged ones decay into muons.

$$\begin{aligned} \pi^+ &\rightarrow \mu^+ + \nu_\mu \\ \pi^- &\rightarrow \mu^- + \overline{\nu}_\mu, \end{aligned} \tag{2.2}$$

with a mean life 2.6033×10^{-8} s [58]. The muons decay through these processes:

$$\begin{aligned} \mu^+ &\rightarrow e^+ + \nu_e + \overline{\nu}_\mu \\ \mu^- &\rightarrow e^- + \overline{\nu}_e + \nu_\mu, \end{aligned} \tag{2.3}$$

with a mean life time of 2.1969811×10^{-6} s. A scheme of a nucleonic shower is presented in Figure 2.4.

The number of particles in an air shower grows till the secondary particles do not have enough energy to produce new ones. The point where the air shower reaches its maximum size is known as the depth of the shower maximum, and it is denoted by $X_{\max}$. The parameter $X_{\max}$ carries relevant information about the primary cosmic ray, such as hints of their chemical composition. The $X_{\max}$ can be used to distinguish between hadronic showers and electromagnetic showers since the latter develop deeper in the atmosphere.

2.4 Composition

Most of the cosmic rays are protons, i.e., ionized hydrogen atoms. They correspond to about 90% of the composition of the cosmic rays. The α-particles are about 9% of the cosmic rays, and the remainder are heavier nuclei. The cosmic ray composition was studied mainly using low-energy cosmic rays since we have more statistics about them. A challenge in ultra-high-energy cosmic ray research is related to the uncertainties in the hadronic interactions at energies above those observed in human-made accelerators, posing a challenge in the mass composition study at these energies.

The abundance of elements in cosmic rays is similar to the one in the solar system. Some light elements, such as lithium, beryllium, and boron, are more abundant in cosmic rays than in the solar system. These elements result from the disintegration of heavier nuclei. This process is called spallation. For these three elements, the primary heavier nuclei are mainly carbon, nitrogen, and oxygen. Right below iron ($Z = 26$) and lead ($Z = 82$), a higher element abundance in cosmic rays relative to the solar system is also observed because of the spallation of these nuclei. The Pierre Auger Collaboration has found a dependence on the energy of the composition of UHECRs. The composition gets lighter up to $10^{18.3}$ eV and, after this point, becomes heavier [59].

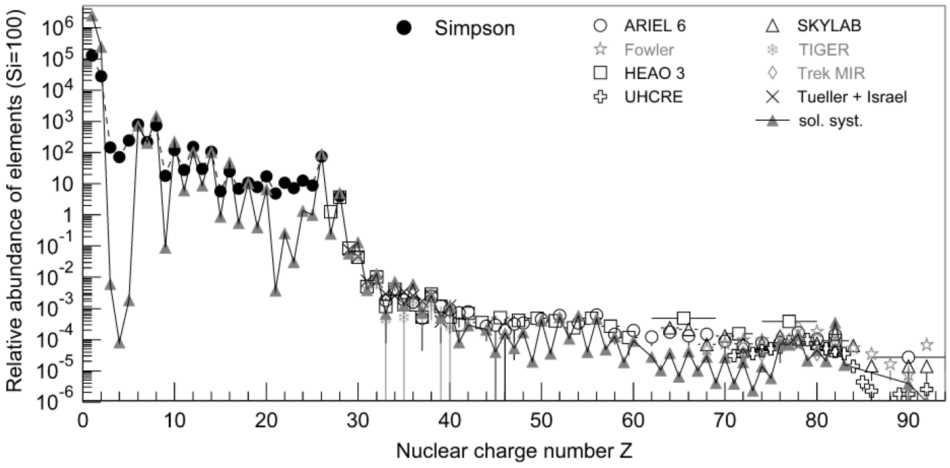

Figure 2.5: The abundance of elements in cosmic rays as a function of their nuclear charge number. The energies are around 1 GeV/nucleon. The abundances are normalized to Si = 100 ($Z = 14$) [60]. Data for $Z \leq 28$ according to [61]. For heavier nuclei, the data is extracted from the following experiments: ARIEL 6 [62, 63], HEAO 3 [64], SKYLAB [65], TIGER [66], TREK/MIR [67, 68], and UHCRE [69]. The solar system abundance was extracted from [70]. Figure extracted from [32].

2.5 GZK effect

In 1965, Arno Allan Penzias and Robert Woodrow Wilson discovered the cosmic microwave background (CMB) radiation. Soon after, two works predicted that the cosmic ray spectrum would end near 10^{20} eV because cosmic rays should lose energy in collisions with the pho-

tons from the CMB. The works of Kenneth Greisen [71], and Georgiy Zatsepin and Vadim Kuzmin [72] were published almost simultaneously, and both studies described what is known as the GZK effect or GZK cutoff. The theoretical limit established on energy considers that cosmic rays are protons. However, results from cosmic ray experiments using giant arrays of detectors such as the Pierre Auger Observatory show that the composition becomes heavier for energies above 10^{17} eV.

Ultra-high-energy protons have such large Lorentz factors that even photons from the CMB radiation have enough energy for the photo-pion production to take place in their rest frame. The CMB radiation has a thermal black body spectrum at a temperature of about 2.7 K [73], resulting in photons with an energy of about

$$E_\gamma = k_\mathrm{B} T = 2.35 \times 10^{-4} \text{ eV}. \tag{2.4}$$

The threshold for photo-pion production is the energy at which the resulting particles are at rest. Using total 4-momentum conservation, the process $p + \gamma_\mathrm{CMB} \rightarrow p + \pi$ results in

$$(\mathbf{p}_p + \mathbf{p}_\gamma)^\mu (\mathbf{p}_p + \mathbf{p}_\gamma)_\mu = (\mathbf{p}_p + \mathbf{p}_\pi)^\mu (\mathbf{p}_p + \mathbf{p}_\pi)_\mu, \tag{2.5}$$

where $\mathbf{p} \equiv (E, \vec{p})$ is the 4-momentum, E is the energy, and $\vec{p}$ is the three-dimensional momentum of the particle[1]. From this equation, we obtain

$$\mathbf{p}_p^2 + 2\mathbf{p}_p \cdot \mathbf{p}_\gamma + \mathbf{p}_\gamma^2 = (m_p + m_\pi)^2, \tag{2.6}$$

where we can use the fact that $\mathbf{p}^\mu \mathbf{p}_\mu = m^2$, and the 4-vector product is given by

$$\mathbf{p}_p \cdot \mathbf{p}_\gamma = E_p E_\gamma - \vec{p}_p \cdot \vec{p}_\gamma = 2E_p E_\gamma. \tag{2.7}$$

In the last part of Equation 2.7, we use the approximation of $|\vec{p}_p| = \sqrt{E_p^2 - m_p^2} \approx E_p$. Therefore, the threshold energy for the proton is

$$E_\mathrm{p} = \frac{m_\pi^2 + 2m_\pi m_\mathrm{p}}{4E_\gamma} \approx 3 \times 10^{20} \text{ eV}. \tag{2.8}$$

The proper calculation of this threshold energy involves integrating over the whole Planck spectrum for a black body since the photons with the highest energies contribute considerably. Considering the higher energy photons, the threshold energy for photo-pion production falls to around 5×10^{19} eV [74].

The Pierre Auger [34, 51–54] and the Telescope Array [75–77] collaborations observe a suppression in the cosmic ray flux around $10^{19.5-19.7}$ eV. However, it is still debated if this suppression is an observation of the GZK effect, representing the end of the cosmic ray

[1] For simplicity, in this section, we use the natural units for the speed of light ($c = 1$).

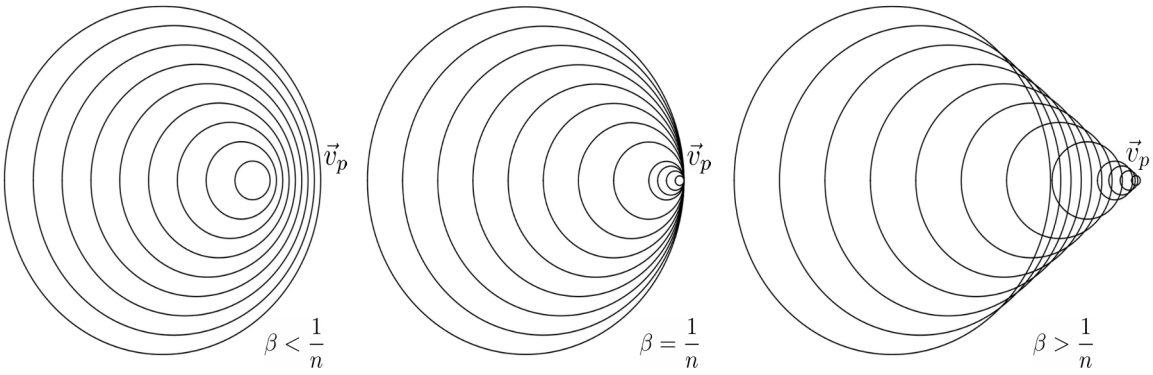

Figure 2.6: A particle moving in a dielectric medium, with a velocity smaller, equal, and higher than the speed of light in this medium. In the last case, when $v_p > c/n$, there is the emission of Cherenkov radiation.

energy spectrum [78]. Another possible explanation is that the sources reached their acceleration limit, causing the suppression [79].

2.6 Cherenkov Effect

The Cherenkov effect occurs when a charged particle traverses a dielectric medium faster than the speed of light in this medium. The emitted photons are mostly in the ultraviolet part of the spectrum. Several particle physics experiments, such as the H.E.S.S. experiment [80], Antares [81], and the Pierre Auger Observatory [82], use the Cherenkov effect to detect charged particles.

In 1934, Pavel A. Cherenkov observed flashes of blue light in liquid mediums when they were under the action of high-energy electrons [83]. Il´ja Mikhailovich Frank and Igor Y. Tamm deduced the formula that gives the quantity of Cherenkov radiation emitted at a given frequency, helping to develop the theory behind this effect [84].

When the particle travels inside a material, it excites the molecules in the medium. When the molecules return to their ground states, they emit photons as electromagnetic radiation. Following the Huygens principle, this radiation propagates with a spherical-shaped shower front. The speed of light in a medium with the refraction index n is $v = c/n$. When the particle moves with a velocity, v_p, higher than the light speed in the medium, occurs emission of Cherenkov light as shown in Figure 2.6. The reason behind this phenomenon is that the emitted waves combine constructively, resulting in coherent radiation with angle θ with respect to the particle direction, as we can see in Figure 2.7. We can geometrically obtain the emission angle θ, as we can observe in Figure 2.7. This angle is given by

$$\cos\theta = \frac{1}{\beta n}, \text{ with } \beta = v_p/c. \tag{2.9}$$

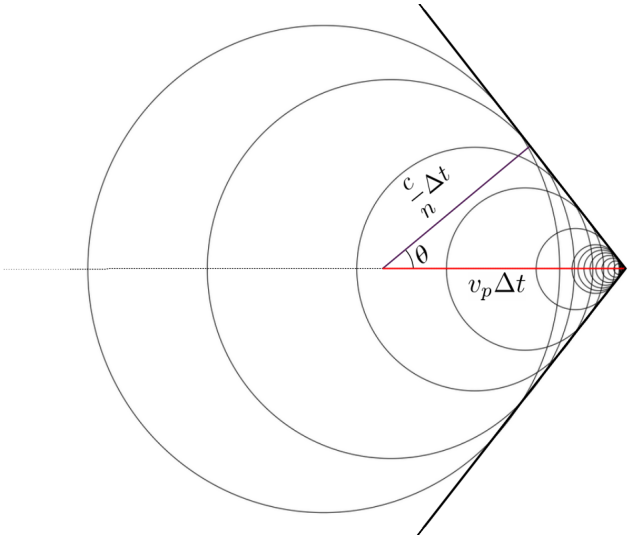

Figure 2.7: Cherenkov emission angle. A particle going faster than the speed of light in a medium produces Cherenkov light with an angle $\theta = \arccos[(\beta n)^{-1}]$.

2.7 Acceleration mechanisms

The comprehension of the mechanisms behind ultra-high-energy particle acceleration is essential to identifying sources of cosmic rays. In this work, we focus on cosmic rays around the EeV decade. In this range, the energy flux is much lower than for energies in the GeV or TeV ($1\,\text{TeV} \equiv 10^{12}\,\text{eV}$) range. For this reason, it is not possible to directly detect cosmic rays in this energy range. There are some techniques to indirectly observe them through the secondary particles produced in the air showers they initiate.

There are two main theories of how charged particles are accelerated close to light speed. In the top-down scenario, cosmic rays are produced in the decay of heavy particles [85]. In the bottom-up scenario, cosmic rays gain energy while accelerating in intense magnetic fields in the interstellar medium [86]. Supernova remnants are the foremost candidates for cosmic ray sources since they have higher magnetic fields than the average interstellar medium. We discuss in more detail the features of the supernova remnants in Chapter 8.

The acceleration mechanisms must explain the observed cosmic ray characteristics. For example, they have to explain why all types of particles in the cosmic ray composition present a power-law energy spectrum, as well as the fact that we observe particles with an energy up to $10^{20}\,\text{eV}$.

2.7.1 Fermi acceleration mechanisms

The Fermi mechanism is a stochastic acceleration method proposed first by the physicist Enrico Fermi in 1949 [87]. This mechanism explains how particles can be accelerated in interstellar clouds. There are two types of Fermi mechanisms: the first- and the second-order mechanism. The first-order has a linear dependence on the velocity of the cloud and

the second-order has a quadratic dependence.

We can formulate the Fermi mechanism in a way that is valid for both the first- and the second-order mechanisms [88]. Let us assume that a particle repeatedly crosses a gas cloud and suffers a variation of energy $\Delta E = \xi E$ after crossing it each time. After n collisions, the particle has an energy

$$E_n = E_0(1+\xi)^n, \tag{2.10}$$

where E_0 is the initial energy before entering the acceleration region. Then, the number of collisions needed to gain an energy E is given by

$$n = \frac{\ln(E/E_0)}{\ln(1+\xi)}. \tag{2.11}$$

The number of particles with an energy larger than E is proportional to

$$N(\geq E) \propto \sum_{m=n}^{\infty} (1-P_{\text{esc}})^m = \frac{(1-P_{\text{esc}})^n}{P_{\text{esc}}}, \tag{2.12}$$

where P_{esc} is the probability of the particle escaping the acceleration region and $m \geq n$. We can replace the number of collisions in Equation 2.12, and we obtain the power-law spectrum

$$N(\geq E) \propto E^{-\gamma}, \tag{2.13}$$

where γ is given by the following expression

$$\gamma = \frac{\ln(1/(1-P_{\text{esc}}))}{\ln(1+\xi)}. \tag{2.14}$$

Second-order Fermi acceleration mechanism

We can deduce the second-order Fermi mechanism using the classical expression for the energy [89]. We start assuming that the particle and the gas cloud are moving in one dimension. In this case, we have two situations: the gas and the cloud are moving in the same direction or opposite directions. If the cloud is moving with a velocity u and the particle with a velocity v, the first scenario leads to a gain of energy equal to

$$\Delta E_1 = \frac{1}{2}m(v+u)^2 - \frac{1}{2}mv^2 = \frac{1}{2}m(u^2+2uv), \tag{2.15}$$

while in the second case, we have

$$\Delta E_2 = \frac{1}{2}m(v-u)^2 - \frac{1}{2}mv^2 = \frac{1}{2}m(u^2-2uv). \tag{2.16}$$

In average, the particle gains $\Delta E = mu^2$, resulting in a relative gain of energy equal to

$$\frac{\Delta E}{E} = \frac{mu^2}{\frac{1}{2}mv^2} = 2\left(\frac{u}{v}\right)^2. \tag{2.17}$$

Since the gas cloud is moving much slower than the particle, $u \ll v$, this mechanism requires a long time to accelerate particles. This process is called second-order mechanism because the relative gain of energy is proportional to $(u/v)^2$.

We also can deduce the relative gain of energy using the relativistic expression for the energy [74]. If the gas cloud is moving with a velocity V, and the cloud is massive enough to not move after the collision, the energy in the frame of the cloud is given by

$$E' = \gamma(V)(E + Vp\cos\theta), \tag{2.18}$$

with $\gamma(V) = (1 - V^2/c^2)^{-1/2}$. In this frame, the x-component of the momentum of the particle is given by

$$p'_x = \gamma(V)\left(p\cos\theta + \frac{V}{c^2}E\right). \tag{2.19}$$

Transforming the energy to the particle frame and expanding to second order in V/c, we obtain

$$\begin{aligned} E'' &= \gamma(V)(E' + Vp'_x) = \gamma^2(V)\left(E + 2Vp\cos\theta + \left(\frac{V}{c}\right)^2 E\right) \\ &= \gamma^2(V)E\left(1 + 2\frac{Vv}{c^2}\cos\theta + \left(\frac{V}{c}\right)^2\right) \\ &\approx E\left[1 + 2\frac{Vv}{c^2}\cos\theta + 2\left(\frac{V^2}{c^2}\right)\right]. \end{aligned} \tag{2.20}$$

Then the difference of energy after the collision is

$$\Delta E \equiv E'' - E = \left[2\frac{Vv}{c^2}\cos\theta + 2\left(\frac{V}{c}\right)^2\right]E, \tag{2.21}$$

and the relative gain is

$$\frac{\Delta E}{E} = 2\frac{Vv}{c^2}\cos\theta + 2\left(\frac{V}{c}\right)^2. \tag{2.22}$$

Averaging in all the possible values for the angle θ between 0 and π and considering the limit $v \to c$, we obtain

$$\left\langle\frac{\Delta E}{E}\right\rangle = \frac{8}{3}\left(\frac{V}{c}\right)^2. \tag{2.23}$$

If the mean free path between clouds is L, the average time between collisions is $2L/c$, and

the rate of energy increase is

$$\frac{dE}{dt} = \frac{4V^2}{3cL}E = \alpha E. \tag{2.24}$$

The diffusion-loss equation assuming that the particle remains in the acceleration region for a characteristic time τ_{esc} is given by

$$\frac{dN}{dt} = D\nabla^2 N(E) + \frac{\partial}{\partial E}[b(E)N(E)] - \frac{N(E)}{\tau_{\text{esc}}} + Q(E), \tag{2.25}$$

and since we are interested in the steady-state solution, we have $dN/dt = 0$. If we don't have diffusion, $D\nabla^2 N = 0$, and assuming that there are no sources, we have $Q(E) = 0$. The energy-loss term is $b(E) = -dE/dt$, which reduces this equation to

$$\frac{dN}{dE} = -\left(1 + \frac{1}{\alpha\tau_{\text{esc}}}\right)\frac{N(E)}{E}. \tag{2.26}$$

Solving this equation, we obtain a power-law energy spectrum,

$$N(E) \propto E^{-[1+(\alpha\tau_{\text{esc}})^{-1}]}. \tag{2.27}$$

Even though the second-order mechanism can explain the power law of the energy spectrum, it is still incomplete since the spectrum index is a function of the product $\alpha\tau_{\text{esc}}$. Since the relative gain in energy is proportional to $(V/c)^2$, this mechanism is much less effective than the first-order mechanism to accelerate particles.

First-order Fermi acceleration mechanism

The first-order mechanism has a linear dependence on the velocity making the acceleration process more effective, especially for higher values of V. When we have head-on collisions only, we can conclude that the linear dependence on the velocity in Equation 2.22 does not disappear. Assuming that the average energy that the particle gains is $E = \xi E_0$, and P is the probability of the particle remaining in the acceleration site after one collision, after n collisions, we will have $N = N_0 P^n$ particles with an energy $E = E_0\xi^n$. Therefore, we obtain the following relation

$$\frac{\ln(N/N_0)}{\ln(E/E_0)} = \frac{\ln P}{\ln \xi} \implies \frac{N}{N_0} = \left(\frac{E}{E_0}\right)^{\ln P/\ln\xi}, \tag{2.28}$$

implying in a differential spectrum following

$$N(E)dE \propto E^{(\ln P/\ln\xi)-1}dE. \tag{2.29}$$

Strong shock waves can be a mechanism to accelerate cosmic rays. They can be produced in astrophysical environments, such as in supernova explosions. When a star ex-

plodes, it deposits around 10^{51} ergs of energy in the interstellar medium as a material propagating with speeds of about 5,000 - 10,000 km/s [90]. The shock wave propagates with a speed much larger than the speed of sound in the medium (about 10 km/s). We can relate the speed of the shock wave using the continuity equation,

$$\rho_1 v_1 = \rho_1 U = \rho_2 v_2, \tag{2.30}$$

where ρ_1 and v_1 are the density and the velocity of the gas downstream (region behind the shock wave), while ρ_2 and v_2 are the density and velocity of the gas upstream (the region ahead). Using the kinetic theory of gases, we conclude that $\rho_2/\rho_1 = 4$. Therefore, $v_2/v_1 = 1/4$, considering a particle crossing the shock wave from the upstream to the downstream region. The velocity of the gas on the downstream side as it approaches the particle is $V = 3U/4$, which implies the Lorentz's transformation energy of the particle passing to the downstream region is

$$E' = \gamma(V)(E + p_x V). \tag{2.31}$$

Since for relativistic particles we have $p \approx E/c$, we can write

$$p_x = p\cos\theta = \frac{E}{c}\cos\theta. \tag{2.32}$$

The relative energy gain is given by

$$\frac{\Delta E}{E} \equiv \frac{E' - E}{E} = \frac{V}{c}\cos\theta. \tag{2.33}$$

The probability of the particle crossing the shock wave is proportional to the x-component of its velocity, i.e., proportional to $\cos\theta$. Normalizing the probability for head-on collisions ($0 \leq \theta \leq \pi/2$), we obtain $p(\theta)d\theta = 2\sin\theta\cos\theta d\theta$. Hence, the average energy gain is given by

$$2\frac{V}{c}\int_0^{\pi/2} \cos^2\theta \sin\theta d\theta = \frac{2}{3}\frac{V}{c}. \tag{2.34}$$

On average, the relative energy increase when making one round trip across the shock and back again is

$$\left\langle \frac{\Delta E}{E} \right\rangle = \frac{4}{3}\frac{V}{c}. \tag{2.35}$$

The fraction of lost particles per unit of time is $4v_2/c = U/c$ [91], implying in an escape probability $P = 1 - U/c$. From Equation 2.35, we conclude that $\xi = 1 + 4V/3c$. Therefore, we obtain

$$\ln P = \ln\left(1 - \frac{U}{c}\right) = -\frac{U}{c} \text{ and } \ln\xi = \ln\left(1 + \frac{4V}{3c}\right) = \frac{4}{3}\frac{V}{c} = \frac{U}{c}. \tag{2.36}$$

Thus, the fraction in Equation 2.28 can be written as

$$\frac{\ln P}{\ln \xi} = -1. \tag{2.37}$$

Replacing this result in Equation 2.29, we recover the differential energy spectrum as

$$N(E)dE \propto E^{-2}dE. \tag{2.38}$$

Even though the exponent -2 does not fully explain the cosmic ray spectrum, since the spectral index is around $2.5 \sim 2.7$ for a great part of the spectrum, it provides a good approximation.

2.8 Previous Experiments

In particle physics, different energies of interest require different types of experiments. The flux of cosmic rays reaching the Earth is strongly energy-related. Therefore, independent experiments investigate each part of the energy spectrum. This work uses data collected at the Pierre Auger Observatory. Thus, we present a complete description of the Observatory in Chapter 3. Below, we briefly describe the most relevant cosmic ray experiments preceding the Auger Observatory.

Volcano Ranch was the first experiment to detect an air shower with energy exceeding 10^{20} eV in February 1962 [92]. Located in New Mexico, USA, the experiment was composed of nineteen scintillators covering an area of 8 km^2. Built by John Linsley and Livio Scarsi in 1959, the experiment ran until 1978.

Haverah Park [93] was projected and built by the University of Leeds in England. With a total area of 34 km^2, it started its operation in 1962. Using Cherenkov detectors, the experiment measured extensive air showers. The Haverah Park experiment made several important contributions to the field of astroparticle physics, such as measuring the cosmic ray spectrum up to energies around 10^{17} eV [39].

The Sydney University Giant Air Shower (SUGAR) array [94] was the first cosmic ray experiment projected to study extensive air showers placed in the southern hemisphere. It operated from 1968 to 1979, having an effective area of 70 km^2.

The Akeno Giant air shower Array (AGASA) was a surface array projected to study ultra-high-energy cosmic rays. The detector covered an area of about 100 km^2 [95]. AGASA was located Akeno Village, 100 km west of Tokyo. It operated between 1990 and 2004. The array had 111 detector stations. The experiment measured the cosmic ray spectrum for energies going up to $10^{18.5}$ eV, besides the study of the chemical composition of cosmic rays [96].

The Fly's Eye [97] was a fluorescence detector operated by the University of Utah between 1981 and 1993. Located in the West Desert of Utah, it was built after a successful test of three prototypes at Volcano Ranch in 1976. Fluorescence light is the product of the

passage of secondary particles in the atmosphere. The array had 67 modules inside steel barrels on motor-driven rotary mounts equipped with spherical mirrors and photomultipliers. The experiment compiled the largest ultra-high-energy cosmic ray data set at the time of its shutdown. The experiment studied the end of the cosmic ray energy spectrum, large and small-scale arrival direction anisotropies, and measured the average depth at which the showers reach the maximum size as a function of the energy. The High-Resolution Fly's Eye (Hires) [98] was the second-generation of the Fly's Eye detector. It operated between 1997 and 2006 on the U.S. Army Dugway Proving Ground in Utah. The experiment was divided into two sites separated 12.6 km from each other. In total, 64 telescope modules were pointed in different sky positions. HiRes-I (HiRes-II) had 22 (42) telescope modules covering 360° in azimuth, and $3° - 17°$ ($3° - 31°$) in elevation. The HiRes Collaboration is alleged to be the first one to observe the GZK suppression [99].

The Telescope Array (TA) experiment [100] is a hybrid detector system located in Millard County, Utah, USA, composed of a set of surface detectors and an array of fluorescence detectors. Its design allows the study of the energy spectrum, the arrival direction distribution, and the composition of ultra-high-energy cosmic rays. Since the site is in the northern hemisphere, TA can complement the field of view of the Pierre Auger Observatory. The surface detector consists of 576 scintillation detectors covering an area of 762 km^2, and there are three fluorescence detector stations. The TA is passing through an upgrade to lower the energy threshold of the experiment. This upgrade is called TALE (Telescope Array Low energy Extension) [101].

3 THE PIERRE AUGER OBSERVATORY

The Pierre Auger Observatory was designed to study ultra-high-energy cosmic rays (UHECRs). It detects secondary particles produced in air showers initiated by cosmic rays interacting at the top of the atmosphere. The Observatory is located in Argentina, in the province of Mendoza, between the latitudes 35.0° and 35.3° S and between the longitudes 69.0° and 69.4° W [56]. It has an average altitude of 1,400 m. Its hybrid design allows the detection of air showers by more than one technique.

The Observatory has two main types of detectors: a Surface Detector (SD) and a Fluorescence Detector (FD). There are four types of data sets recorded in the Observatory. The vertical full-array data set includes events[1] with a zenith angle[2] up to 60°, leading to a field of view from −90° up to 25° in declination. The inclined full-array data set includes events with zenith angles between 60° and 80°, reaching declinations up to 45°. Events recorded with the infilled array form the infill data set. In this chapter, we describe the full and the infilled array. The hybrid data set includes events recorded simultaneously by the SD and the FD arrays. In this work, we use events recorded at the SD of the Pierre Auger Observatory, investigating three data sets: the vertical, the inclined, and the infill. Hybrid events are used to calibrate the energy.

Cosmic rays penetrating the Earth's atmosphere are mainly protons, nuclei, and photons. Each type of primary particle produces an air shower with different characteristics, allowing us to obtain information about the primary particle. Properties such as the energy and the arrival direction of the primary particle affect the shower development. Therefore, the data collected at the Observatory from the secondary particles allow us to recover information about the cosmic rays penetrating the atmosphere.

The arrival directions of the primary particles are reconstructed based on the times when the SD stations are triggered by the secondary particles in the air shower. Knowing the position of the SD detectors and the arrival times of the secondary particles, it is possible to fit a plane front moving at the speed of light to estimate the arrival direction of the shower. The energy of the primary cosmic ray is reconstructed by fitting the signals of the individual SD stations to a lateral distribution function, using hybrid events. The fit parameters are then used for all the events recorded by the SD.

In this Chapter, we describe the detectors used at the Pierre Auger Observatory. We also discuss the energy and the arrival direction reconstruction. The Observatory is passing through an upgrade. We briefly describe the upgrade in Section 3.5. In the next section, we present the details of the SD.

[1] In this work, an *event* refers to an air shower detected at the Pierre Auger Observatory.
[2] We present a description of the coordinate systems used in this work in Appendix A.

3.1 Surface Detector

The Surface Detector is an array of 1,660 water-Cherenkov stations covering an effective area of about 3,000 km^2. In Figure 3.1a, we show a picture of an SD station with the main components, and in Figure 3.1b, we show a scheme of the surface array. The SD allows the study of cosmic rays above 10^{17} eV. Of the 1,660 water-Cherenkov tanks, around 1,600 are spaced 1.5 km from each other in triangular arrays, and the other 60 have a smaller distance between them of about 750 m. The smaller array is called the *infilled* array and covers an area of around 24 km^2 [102].

Each water-Cherenkov detector is a station equipped to detect the signals produced by the secondary particles of an extensive air shower traversing the station. UHECRs can create showers with a footprint at the ground of about 25 km^2, activating almost simultaneously several detector stations. The time difference between the signal reception in the various water-Cherenkov stations is used to determine the arrival direction of the primary particle.

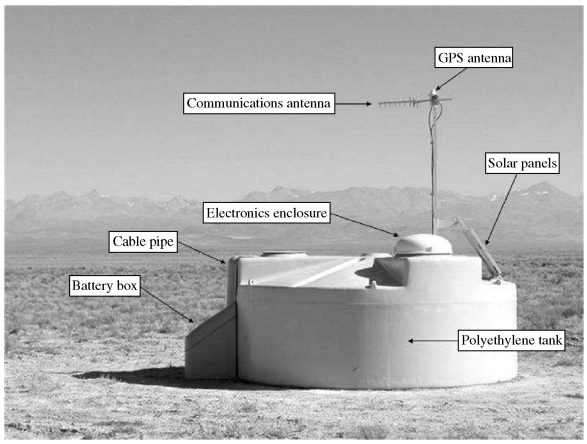

(a) An SD station. Figure extracted from [82].

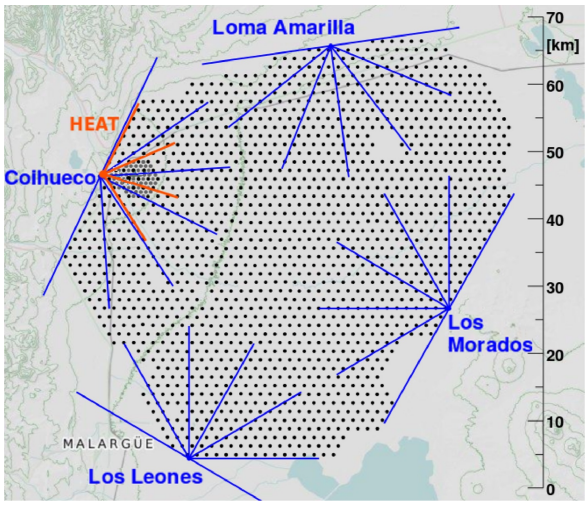

(b) A scheme of the Pierre Auger Observatory array. The dots represent the SD stations and the lines represent the field of view of the FD telescopes. Figure extracted from [103].

Figure 3.1: An SD station and a scheme of the SD array.

The detector stations are composed of a water tank with a liner bag containing around 12,000 liters of ultra-pure water, and an electronic package with a solar panel, batteries, and three 9-inch diameter photomultiplier tubes (PMTs) symmetrically distributed. The water tank is a 3.6 m diameter cylinder with a 1.2 m depth of water. The liner has a reflective surface. The ultra-pure water avoids the bacteria grown inside the tank that would interfere with the measurement of the Cherenkov light. The photomultipliers detect the light produced by the Cherenkov effect, and the signal is used to reconstruct the energy of the primary particle. The SD stations work almost all the time, having a duty cycle ~ 100% [82].

A wireless system is used to transfer the information recorded by an SD station to the Central Data Acquisition System (CDAS). To determine if the signals detected in the

tanks are from an actual cosmic ray event, a series of triggers is used. In the next subsection, we describe the trigger system.

3.1.1 The trigger system

A trigger system is used to select the signals produced in the water-Cherenkov tanks that correspond to an actual cosmic ray event. A full description of the trigger system can be found at [104]. The data acquisition (DAQ) trigger satisfies technical and physical requirements. The trigger system works hierarchically, being composed of five levels.

The charged particles produced in the air showers reach the SD stations with a speed higher than the speed of light in the water in the tank, causing the Cherenkov radiation emission. We discuss the Cherenkov effect in Section 2.6. The photons from the Cherenkov radiation produce an electrical signal in the PMTs through the photoelectric effect. The signals provided by the PMTs are digitized by the Flash Analog-to-Digital Converters (FADCs). Each detector has a local calibration performed automatically. Each FADC bin corresponds to 25 ns [105]. An example of a FADC trace of a PMT is shown in Figure 3.3.

The average charge collected by a PMT from the Cherenkov light produced by a vertical and central through-going muon is called Q_{VEM} or VEM (Vertical Equivalent Muon). The distribution of the light produced by the atmospheric background muons creates a peak in the charge distribution, $Q^{\mathrm{peak}}_{\mathrm{VEM}}$, and in the pulse height, $I^{\mathrm{peak}}_{\mathrm{VEM}}$. The measurement of 1 VEM in electronic units is obtained from the $Q^{\mathrm{peak}}_{\mathrm{VEM}}$.

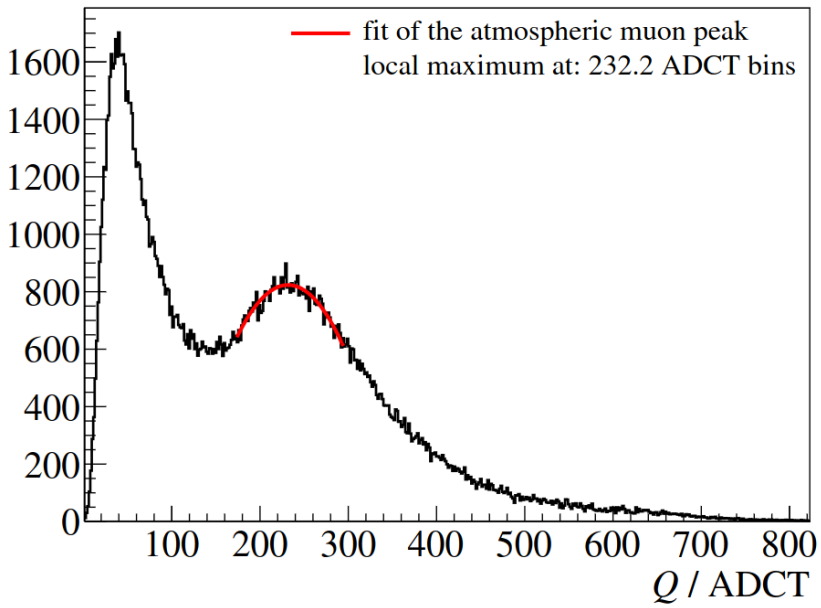

Figure 3.2: The integrated signals used to convert the station signals into VEM units. The peak caused by the atmospheric background muons is used as a reference value for the VEM unit. Figure extracted from [106].

The first level trigger T1 is at the station level. There are two modes designed for different features: the Threshold (TH) trigger and the Time-over-Threshold (ToT) trigger.

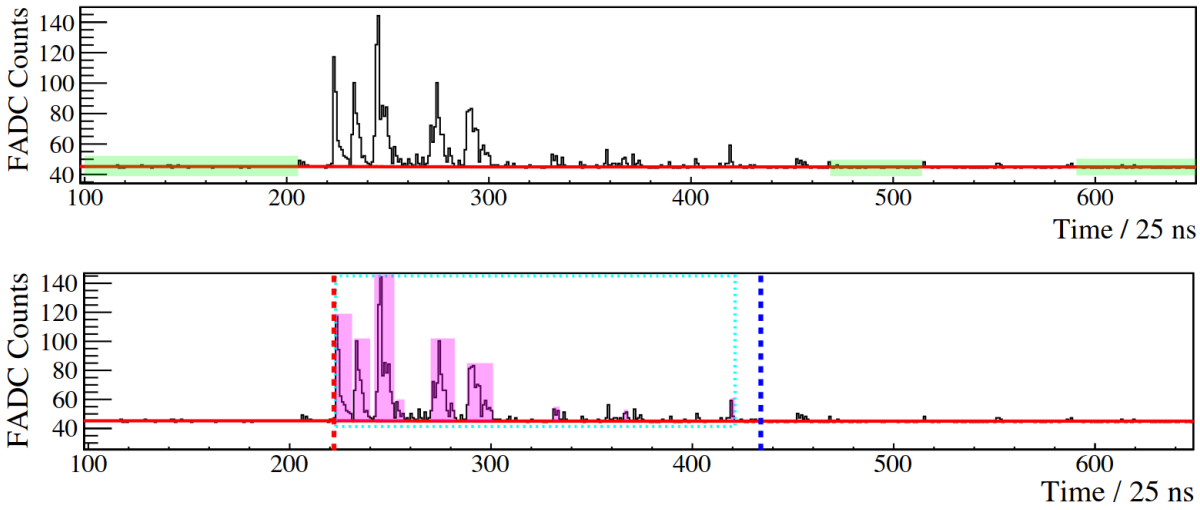

Figure 3.3: The FADC trace of a PMT. Considering the peaks, this trace probably contains around five muons and some electromagnetic component. Figure extracted from [106].

The TH trigger is activated when the PMTs detect a signal above $1.75 I_{\mathrm{VEM}}^{\mathrm{peak}}$ in at least a time bin (25 ns). This trigger is sensitive to signals that are not spread in time, as it occurs in inclined showers in which the electromagnetic component is absorbed by the atmosphere and only muons arrive at the stations on the ground. The ToT trigger requires a signal $> 0.2 I_{\mathrm{VEM}}^{\mathrm{peak}}$ in 13 bins (325 ns), being effective in detecting vertical showers with a large electromagnetic component. The ToT is used to identify low-energy showers or those with high-energy in which the detector stations are farther from the core. Since ToT is not that sensitive to the muonic component, it is useful to remove the muon background.

The next trigger level, T2, is also at the station level. All the ToT-T1 events are promoted to the T2 trigger level, while the TH-T1 must have a signal greater than $3.2 I_{\mathrm{VEM}}^{\mathrm{peak}}$ in all the three PMTs. If a station has only two or one working PMTs, the threshold used is $3.8 I_{\mathrm{VEM}}^{\mathrm{peak}}$ in both or $4.5 I_{\mathrm{VEM}}^{\mathrm{peak}}$ in that one.

The next trigger level looks for temporal and spatial coincidences among the events passing the T2 trigger. The information from the T2 events is sent to CDAS. The T3 trigger works in two modes. The first one requires the coincidence of at least three stations passing the ToT-T2 that satisfy a minimum criterion of spatial compactness. It is required that at least one station from the first-neighbor set and one from the second-neighbor set be activated. A temporal coincidence is required to ensure that the particles in the front of the shower plane can travel that distance. The second mode requires at least four stations respecting the same time window as the other mode and passing any of the T2 trigger levels, but it is more relaxed in terms of spatial compactness. From the four stations, one is the reference, at least one needs to be in the first set of neighbors from that one, one in the second set, and the last one can be as far as the fourth set of neighbors.

The T4 trigger level is the physics trigger. It requires that at least three nearby stations, which were promoted by the ToT-T2 and the T3 triggers, form a triangular pattern,

fitting a plane front moving at the speed of light. The other mode requires that four nearby stations, which passed the T3 trigger, fit a plane front moving at the speed of light.

The last level is the T5 fiducial trigger. It requires that the six closest stations to the one with the highest signal are active at the moment of the event. Events satisfying this condition are called 6T5 events. Some analyses can be more relaxed, requiring only five active stations out of the six closest stations. These are the 5T5 events. If all six stations are active, it is possible to ensure a good reconstruction of the core of the shower, improving the reconstruction of the energy. It also ensures that the shower core is within the SD array. In this work, we use only 6T5 events.

3.2 Fluorescence Detector

The Fluorescence Detector is a set of 27 telescopes overviewing the Observatory designed to study the development of air showers in the atmosphere. A scheme of a fluorescence telescope is presented in Figure 3.4a. The fluorescence telescopes are distributed at four sites: *Los Leones*, *Loma Amarilla*, *Coihueco*, and *Los Morados*. In each location, a building houses six telescopes. In Figure 3.4b, we show a picture of one of these buildings. Each telescope has a field of view of 30° in elevation and 30° in azimuth. The six telescopes combined have a field of view of 180° in azimuth [107]. We can see a representation of the field of view of the FD telescopes in Figure 3.1b. The other three telescopes are located in Cerro Coihueco and are the High Elevation Auger Telescopes (HEAT), described in section 3.3.

The secondary particles of the air shower traveling through the atmosphere excite the nitrogen molecules in the air. In the de-excitation, the nitrogen molecules emit photons in the UV range. The telescopes can detect this fluorescence light. A key characteristic observed using the FD is the maximum depth of the showers. This feature is related to the mass composition of the primary particle.

The FD uses the atmosphere as a quasi-calorimeter to determine the energy of the primary particle, allowing the energy calibration of events recorded by the SD through hybrid events. We present more details of the energy reconstruction in Section 3.4. The telescopes are used in nights without moonlight. The duty cycle of the FD is ~ 15%.

3.3 Other detectors

Besides the SD and the FD arrays, the Observatory has other detector arrays. We listed them below.

Auger Muon and Infilled Ground Array (AMIGA)

The AMIGA detectors were designed to study the muon content of showers in which the primary cosmic ray has energy ~ 10^{17} eV [108]. AMIGA is an array of detector pairs composed of a surface water-Cherenkov detector of the infilled array and a buried 30 m^2 muon counter

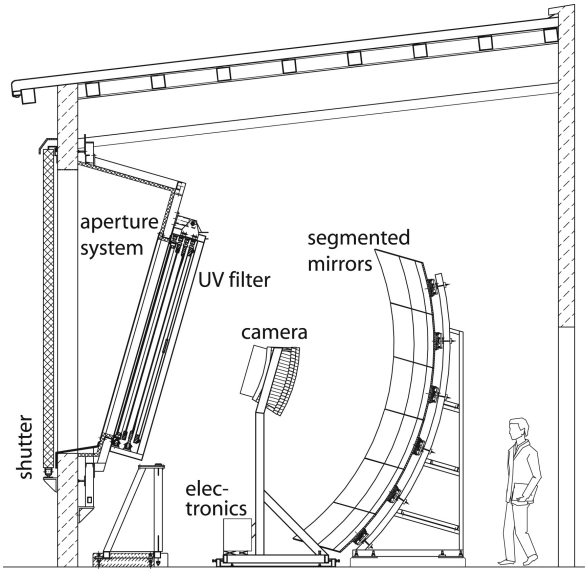

(a) A scheme of a fluorescence telescope. Figure extracted from [107]

(b) A picture of one of the buildings that house the fluorescence telescopes. Figure extracted from [56]

Figure 3.4: A scheme of one of the FD telescopes and a picture of one of the buildings that house the FD telescopes.

nearby. While the surface detector full-array has a spacing of 1,500 m between the water-Cherenkov detectors, the infilled area has a spacing of 750 m, covering an area of approximately 24 km^2. First planned to contain 61 SD detectors spaced 750 m between each other, the first infilled array was completed in 2012. A denser array covering an area of 1.9 km^2 spaced 433 m was included in 2019 [109].

High Elevation Auger Telescopes (HEAT)

The High Elevation Auger Telescopes (HEAT) are projected to study the development of air showers with an energy lower than 10^{18} eV. HEAT consists of three fluorescence detectors installed at Cerro Coihueco that can be tilted upwards, allowing to observe the sky up to 60° elevation [110]. By looking at higher positions in the sky, the telescopes can detect the maximum development of air showers with energies $\sim 10^{17}$ eV. HEAT oversees the infilled part of the SD, allowing cosmic ray events with lower energy, around 0.1 EeV, to be recorded by both the SD and the FD arrays.

Auger Engineering Radio Array (AERA)

AERA is an antenna system projected to measure short radio pulses emitted by cosmic ray air showers. This system is co-located with the infilled array of water-Cherenkov detectors and is overlooked by the HEAT telescopes. It is a system composed of around 150 radio antenna stations spread over an area of 17 km^2 able to detect events with energies above 0.1 EeV [111]. The main advantage over the fluorescence telescope technique is that the radio antennas work nearly 100% of the time, while the telescopes have a $\sim$ 15% duty cycle.

3.4 The event reconstruction

In this section, we describe the reconstruction of the energy and the arrival direction of a cosmic ray event recorded by the SD array. We can find a complete description of the event reconstruction in [106]. The event reconstruction depends on the signals and times recorded by the individual water-Cherenkov stations. The usage of the differences in the arrival times of the air shower front to determine the arrival direction is a technique used since the 1950s [112].

The shower size is the number of particles at a given observation level and depends on the energy of the primary particle. However, the relation between the number of particles and the energy of the primary particle is not simple, presenting a dependence on the development of the shower. A cosmic ray interacting deeper in the atmosphere can produce an air shower with the same number of events at the ground level as a more energetic shower that starts developing earlier at the top of the atmosphere.

The unit used to measure the Cherenkov light produced during the passage of charged particles resulting from the air shower development is the *Vertical Equivalent Muon* (VEM) as explained in Subsection 3.1.1. The first step to reconstructing the event is to roughly estimate its arrival direction and the impact position of its core.

The barycenter can be defined as the signal-weighted center-of-mass of the stations involved in an event. Assuming that the core of the shower is traveling in the direction $-\hat{a}$ and hits the ground at barycenter $\vec{x}_{\mathrm{b}}$ at the time t_{b}, and that the front of the shower is a plane perpendicular to the shower axis moving with the speed of light c, we have the relation between the time t_{sh} that the front passes at the position $\vec{x}$ from the projection onto the shower axis:

$$c\,t_{\mathrm{sh}}(\vec{x}) = c\,t_{\mathrm{b}} - \hat{a}\cdot(\vec{x}-\vec{x}_{\mathrm{b}}). \tag{3.1}$$

The exact solution of the Equation 3.1 is obtained using the *seed triangle*. The seed triangle is obtained by taking three stations, in a non-aligned configuration, in which all three have passed the station level trigger. The three stations with the highest signal sum form the seed triangle. The i-th station is triggered at the instant t_i (Figure 3.5). Using the position $\vec{x}_i$ of the station and the time at which it was triggered t_i, the approximation of the direction of the shower axis is obtained.

3.4.1 Shower geometry

The reconstruction of the shower geometry is the reconstruction of the arrival direction $\hat{a}$ and the impact point of the shower core $\vec{x}_{\mathrm{c}}$. Equation 3.1 gives a rough estimation of these two parameters, since the barycenter $\vec{x}_{\mathrm{b}}$ can be used as the approximated position of the impact point of the core. It is possible to model a curved shower front. Since the furthest

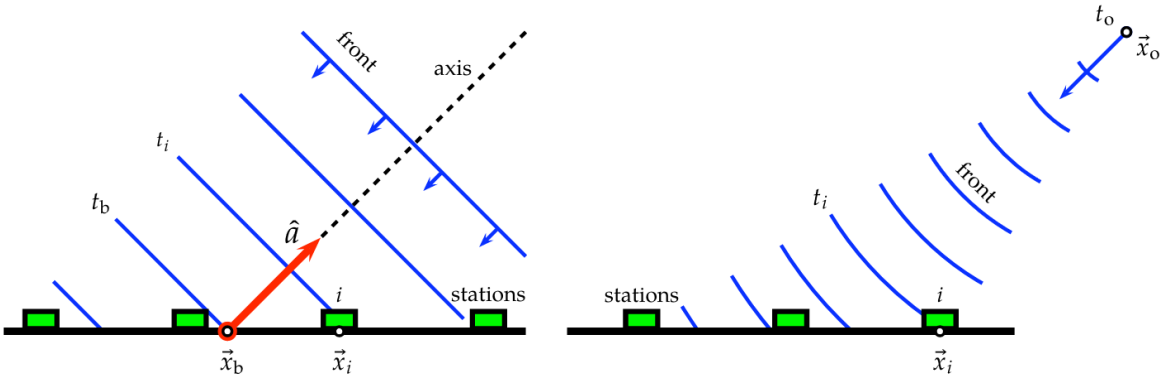

Figure 3.5: A scheme of the arrival direction reconstruction. On the left, the front of the shower is approximately a plane. On the right, a curvature is included. Figure extracted from [106].

particles of the shower have a delay in their arrival time, it is possible to include this curvature in the event reconstruction. In the *Herald* framework, the curvature is considered constant. Considering the radius of curvature R_o, we can define the curvature parameter $k_o = 1/2R_o$. Then, the paraboloidal extension of Equation 3.1 is given by

$$c\,t_{sh}(\vec{x}) = c\,t_c - \hat{a}\cdot(\vec{x}-\vec{x}_c) + k_o[r_{\hat{a}}(\vec{x}-\vec{x}_c)]^2, \tag{3.2}$$

where the quantity $r_{\hat{a}}(\vec{x}) = |\hat{a}\times\vec{x}|$ is the perpendicular distance between the point $\vec{x}$ and the shower axis $\hat{a}$. Using the arrival times of the secondary particles in an air shower and the position of the stations in Equation 3.2 determines the arrival direction of the event. The reconstructed arrival direction demonstrated an angular resolution on the order of 1°, approaching 0.5° for the largest shower sizes [106].

3.4.2 Shower size

After the geometry reconstruction, we can use the information about the direction of the shower axis, $\hat{a}$, and the position of its impact at the ground, $\vec{x}_c$, to estimate the shower size. The shower size is inferred from the lateral distribution function (LDF). The shower size at a distance r of the shower axis is given by:

$$S(r) = S(r_{opt})\,f_{LDF}(r), \tag{3.3}$$

where $r_{opt} = 1{,}000$ m for the full array (stations spaced 1,500 m from each other) and $r_{opt} = 450$ m for the infill array (stations spaced 750 m from each other). In the *Herald* framework, the LDF is described by a log-log parabola function:

$$\ln f_{LDF}(r) = \beta\rho + \gamma\rho^2, \quad \text{with} \quad \rho = \ln\left(\frac{r}{r_{opt}}\right), \tag{3.4}$$

and the parameters β and γ are the average slope parameters of the function. The β parameter is obtained in a data-driven way, while the γ parameter is obtained from Monte Carlo

studies. Finally, both parameters are parameterized in terms of the zenith angle and $S(r_{opt})$.

Since the FD provides an almost-calorimetric energy measurement, the hybrid events, i.e., those detected both by the FD and the SD, are used to calibrate the energy. Due to geometrical effects, the value of $S(1000)$ is attenuated with the zenith angle. Events with a larger zenith angle travel a longer distance in the atmosphere, increasing the absorption of the electromagnetic content of the shower. The function $f_{CIC}(\theta)$ that describes the attenuation is obtained using the Constant Intensity Cut (CIC) method [113]. The attenuation factor as a function of the secant of the zenith angle is presented in Figure 3.6. The median zenith angle of $\overline{\theta} = 38°$ is used (for the infill array $\overline{\theta} = 35°$ is used [102]) to convert $S(1000)$ to $S_{38} \equiv S(1000)/f_{CIC}(\theta)$. Using the measured energies obtained with the FD, we can extract the fit parameters A and B from the relation $E_{FD} = A(S_{38}/\text{VEM})^B$. We show the relation between the S_{38} parameter and the energy E_{FD} in Figure 3.7. Finally, we obtain the SD energy estimator as:

$$E_{SD} = A(S(1000)/f_{CIC}(\theta)/\text{VEM})^B. \tag{3.5}$$

The fit parameter A is approximately 1.9×10^{17} eV and the fit parameter B is approximately 1.03 [34]. The resolution in the reconstructed shower size is ~ 15% for the smallest showers and ~ 6% for the largest ones [106].

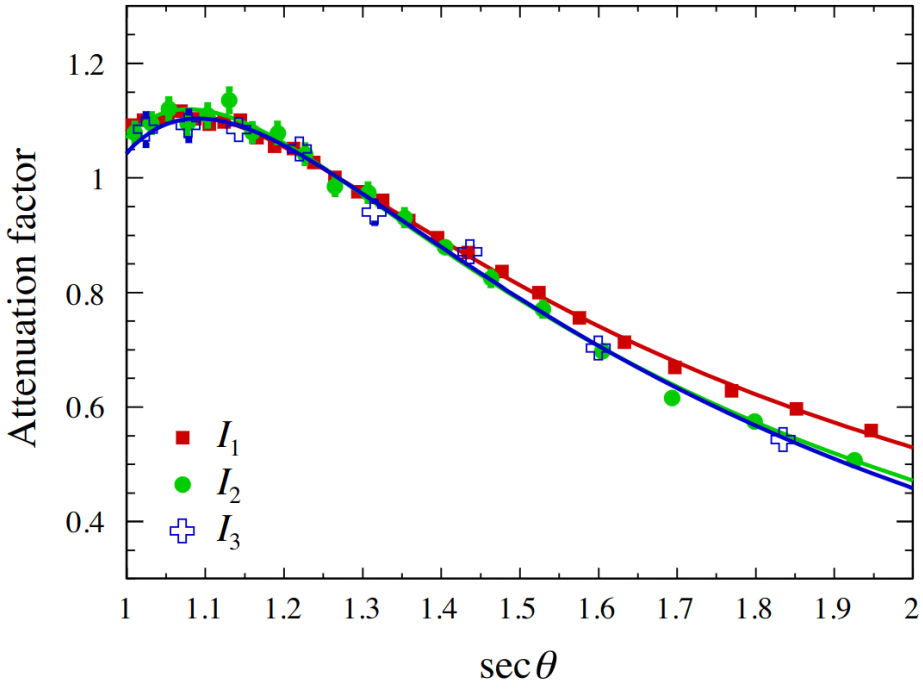

Figure 3.6: The attenuation factor as a function of the secant of the zenith angle. The curves are normalized to 1 at $\theta = 38°$. The plot shows the attenuation factor for three different intensities ($I_1 > I_2 > I_3$). Figure extracted from [34].

Inclined showers, i.e., those with $\theta > 60°$, have a different reconstruction. Since a more inclined shower will travel a longer distance through the atmosphere than a vertical

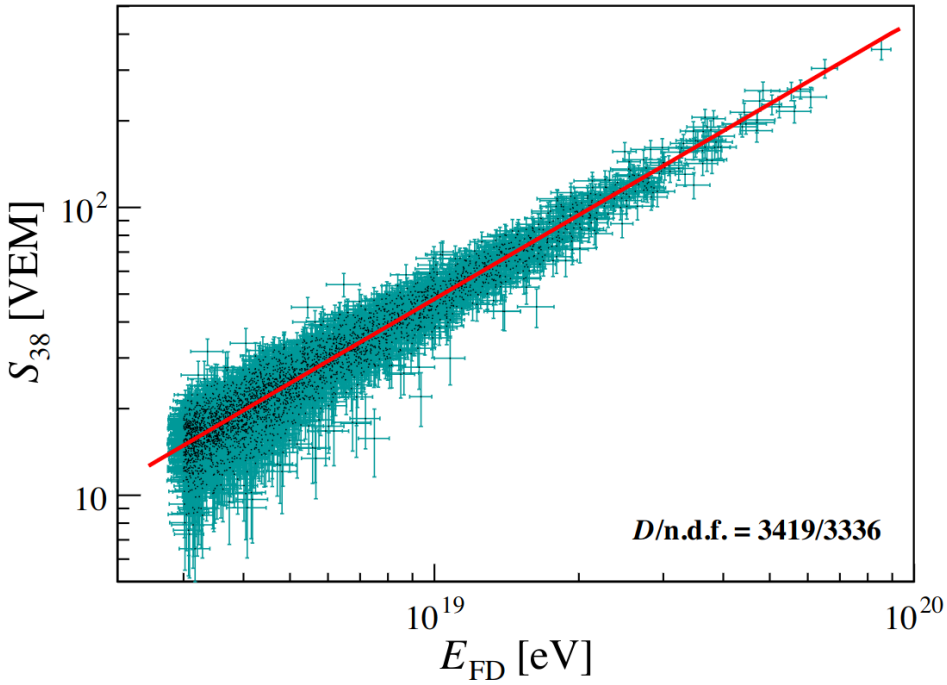

Figure 3.7: The S_{38} as a function of the energy E_{FD}. The red line represents the best fit for the data used in this analysis. The parameters A and B are obtained from this fit. Figure extracted from [34].

shower, the electromagnetic component is more absorbed in inclined showers. Due to this absorption, inclined showers arrive at ground level with a front dominated by muons. A full description of the event reconstruction for inclined showers can be found in [114].

The arrival direction of an inclined shower is obtained through the fit of the times recorded at the triggered SD stations. Events with a large zenith angle trigger more SD stations. Hence, inclined air showers provide a better estimation of the arrival direction of the event, resulting in a smaller angular resolution. The signals produced in the water-Cherenkov stations are fitted using the two-dimensional distribution of the muon number density (number of muons per unit of area),

$$\rho_\mu(\vec{r}) = N_{19}\ \rho_{\mu,19}(\vec{r};\theta,\varphi), \tag{3.6}$$

where the distances are defined with respect to the position of the reconstructed shower core (x_c, y_c), i.e, $\vec{r} = (x - x_c, y - y_c)$. The parameter N_{19} is the shower size and represents a normalization with respect to a reference distribution of the muon number density $\rho_{\mu,19}(\vec{r};\theta,\varphi)$. This reference distribution is chosen as the average muon density obtained with protons of 10^{19} eV simulated using the shower model QGSJetII-03. It is possible to write Equation 3.6 because the muon density escalates almost linearly with energy, $\rho_\mu \propto E^\alpha$, with α between 0.90 and 0.95 [115].

The muonic signal measured by an individual station, S_μ^{meas}, is estimated from the total signal S^{meas} using the ratio between the electromagnetic and muonic component.

This ratio is obtained from Monte Carlo simulations, and it is given by

$$R_{\mathrm{EM}/\mu} = \frac{S_{\mathrm{EM}}(r,\theta)}{S_{\mu}(r,\theta)}. \tag{3.7}$$

Using this ratio, we can estimate the muonic contribution to the total signal,

$$S_{\mu}^{\mathrm{meas}} = \frac{S^{\mathrm{meas}}}{1+R_{\mathrm{EM}/\mu}}. \tag{3.8}$$

The expected number of muons in a station can be estimated from the muon density and the projected detector area, $A_{\perp}$,

$$n_{\mu} = \rho(\vec{r})A_{\perp} = N_{19}\rho_{\mu,19}(\vec{r},\theta,\varphi)A_{\perp}. \tag{3.9}$$

From the expected number of muons, the shower size N_{19} and the position of the shower core $(x_{\mathrm{c}}, y_{\mathrm{c}})$ are extracted. The procedure is made by fitting the expected number of muons to the muonic contribution (Equation 3.8) performing a maximum-likelihood method. Finally, the energy reconstruction is made using hybrid events in a similar procedure to the one used for vertical events. The relation between the shower size N_{19} and the energy measured using the FD, E_{FD}, is

$$N_{19} = A(E_{\mathrm{FD}}/10^{19}\ \mathrm{eV})^{B}, \tag{3.10}$$

where the fit parameters A and B are obtained from hybrid events. The relation between the parameter N_{19} and the energy E_{FD} is presented in Figure 3.8. Equation 3.10 can be used to estimate the energy of all the inclined events recorded by the SD. The value for the fit parameter A is 1.723, and for the fit parameter B is 0.984 [114].

3.5 AugerPrime

The Observatory is undergoing an upgrade called AugerPrime. In this section, we describe the main upgrades. AugerPrime encompasses various enhancements. These enhancements consist of the installation of a plastic scintillator detector and a radio antenna on top of each water-Cherenkov station, the inclusion of a small PMT, accompanied by the new electronics, and an array of underground detectors to measure the muonic component of lower energy air showers [116].

The Pierre Auger Collaboration made huge advances in the understanding of the highest energy cosmic rays, such as the spectrum, showing clearly a suppression around 5×10^{19} eV [34] and the presence of a dipole in the arrival direction distribution of cosmic rays, pointing around 125° away from the Galactic center for energies above 8×10^{18} eV [30]. However, the study of mass composition and the understanding of the hadronic models for the highest energies are still a challenge. The upgrade of the Observatory aims to help un-

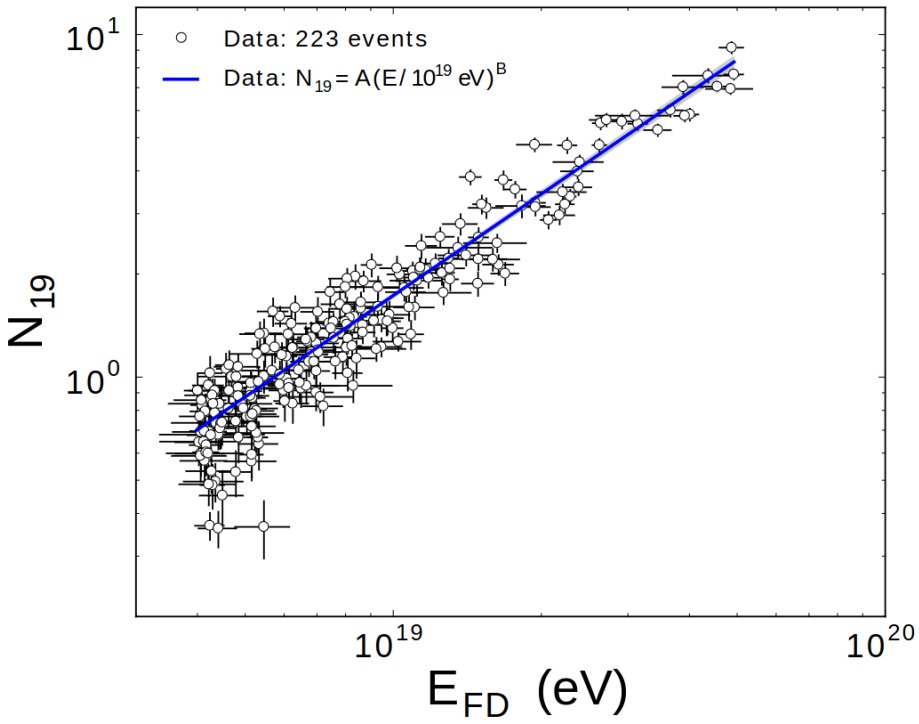

Figure 3.8: The N_{19} parameter as a function of the energy E_{FD}. The blue line represents the best fit. The fit parameters are used to estimate the energy of the inclined events recorded by the SD. Figure extracted from [114].

ravel these questions. The main questions addressed by AugerPrime include understanding the nature and the origin of UHECRs, the origin of the observed suppression in the cosmic ray flux, the investigation of ultra-high-energy (UHE) photons and neutrinos, explaining the origin of the muon puzzle, and searching for physics beyond the standard model.

By improving anisotropy studies using the new information regarding mass composition, the enhancements will increase the potential of detecting UHECR sources. AugerPrime will open the possibility of discovering both point sources and source regions. In addition, the enhanced mass composition results will allow to set constraints in the source models, potentially having consequences in cosmological models.

The suppression of the cosmic ray flux is well-established. However, the origin of this suppression remains unclear. A pure proton GZK effect seems disfavored. AugerPrime data is expected to shed light on this matter. This suppression can be caused by propagation effects caused by photon-dissociation of heavier nuclei or the limitation of the sources. Another possibility is a combination of both. AugerPrime is expected to provide information about the transition in mass composition from light to heavy primaries and provide new information on the evolution of the spectrum as a function of energy.

AugerPrime data will be used in the search for UHE photons and neutrinos. In particular, the improved neutrino-specific triggers will increase the chances of detecting UHE neutrinos, providing new information for multi-messenger astronomy.

Recent results on the muon content of UHE extensive air showers have demon-

strated a muon deficit in the air shower simulations with respect to data. This phenomenon is called the muon puzzle. Many theories try to explain its origin [117–120]. Higher quality measurements reached with AugerPrime can help to investigate the muon deficit's origin in hadronic models.

AugerPrime can reveal physics beyond the standard model in topics such as the search for dark matter candidates and quantum gravity. UHE photons and neutrinos would be produced in super-heavy dark matter decay. Therefore, detecting such particles could be evidence of the existence of super-heavy dark matter.

The AugerPrime elements are:

Scintillator Surface Detector (SSD): A 3.8 m^2 plastic scintillator detector on top of each existing water-Cherenkov detector. The two detectors have different responses for the electromagnetic and the muonic contents. This upgrade will help to determine the muon density for vertical showers.

Radio Detector (RD:) A 30 to 80 MHz antenna on top of each water-Cherenkov detector. The radio signals detected by the antennas provide a measurement of the electromagnetic component of air showers with a zenith angle larger than 65°. Since most of the electromagnetic content is absorbed by the atmosphere at these zenith angles, the water-Cherenkov detectors detect mainly the muon content of these showers.

Underground Muon Detector (UMD): Plastic scintillator detectors for muon counting are installed in the portion of the array in which the stations are spaced 750 m from each other. The scintillators are shielded by a 2.3 m layer of soil. They provide a direct measurement of the muon content of the showers.

Upgraded Unified Board (UUB): The stations of the SD are upgraded with new electronics, increasing the data quality, in addition to enhancing the monitoring and processing capabilities. UUB will process the signals from the water-Cherenkov detectors, besides the SSD and RD.

4 DATA SETS

In the next chapters, we will describe three methods to search for point sources of neutrons. We perform the searches using data collected in the Pierre Auger Observatory. We describe the Observatory in Chapter 3, with details about the Surface Detector (SD) and the Fluorescence Detector (FD). The results presented in this work are obtained with events recorded by the SD array. In this chapter, we describe the data sets used.

We use three data sets for the analysis presented in this work: the vertical, the inclined, and the infill ones. The vertical and the inclined data sets were recorded using the SD detector from January 1 2004 to July 31 2022[1]. The vertical data set has 2,535,932 events with a zenith angle satisfying $0° \leq \theta \leq 60°$ and energy $E \geq 1$ EeV. The inclined data set contains 353,227 events with zenith angle $60° \leq \theta \leq 80°$ and energy $E \geq 1$ EeV. Both the vertical and the inclined data set were recorded by the full array of the Observatory, i.e., the array in which the detector stations are spaced by 1,500 m. The infill data set was recorded in the smaller array in which the detector stations are separated by 750 m from each other. The infill data set has 2,235,796 events with a zenith angle satisfying $0° \leq \theta \leq 55°$ and energy $E \geq 0.1$ EeV.

We split each data set in four energy ranges: $1\,\text{EeV} \leq E < 2\,\text{EeV}$ ($0.1\,\text{EeV} \leq E < 0.2\,\text{EeV}$), $2\,\text{EeV} \leq E < 3\,\text{EeV}$ ($0.2\,\text{EeV} \leq E < 0.3\,\text{EeV}$), $E \geq 3$ EeV ($E \geq 0.3$ EeV), and $E \geq 1$ EeV ($E \geq 0.1$ EeV) for the vertical and inclined (infill) data sets. The last energy range is the combination of the data sets in the other three energy ranges. Table 4.1 presents the number of events in each energy range. The data sets were treated independently.

Table 4.1: Number of events in each data set by energy range.

Number of events in each data set				
Energy range	**Vertical**	**Inclined**	**Energy range**	**Infill**
$E \geq 3$ EeV	238,570	81,212	$E \geq 0.3$ EeV	238,266
$1 \leq E/\text{EeV} \leq 2$	1,948,058	180,598	$0.1 \leq E/\text{EeV} \leq 0.2$	1,627,227
$2 \leq E/\text{EeV} \leq 3$	349,304	91,417	$0.2 \leq E/\text{EeV} \leq 0.3$	370,303
$E \geq 1$ EeV	2,535,932	353,227	$E \geq 0.1$ EeV	2,235,796

The work published by the Auger Collaboration in 2014 about the neutron search for point sources of neutrons [2] studied only vertical events. The total number of events was 854,270. In our analysis, we updated the vertical data set increasing the total number to 2,535,932 events. In this thesis, we use 6T5 events, i.e., those in which all the six closest

[1] The infill data set was recorded from August 1 2008 to July 31 2022.

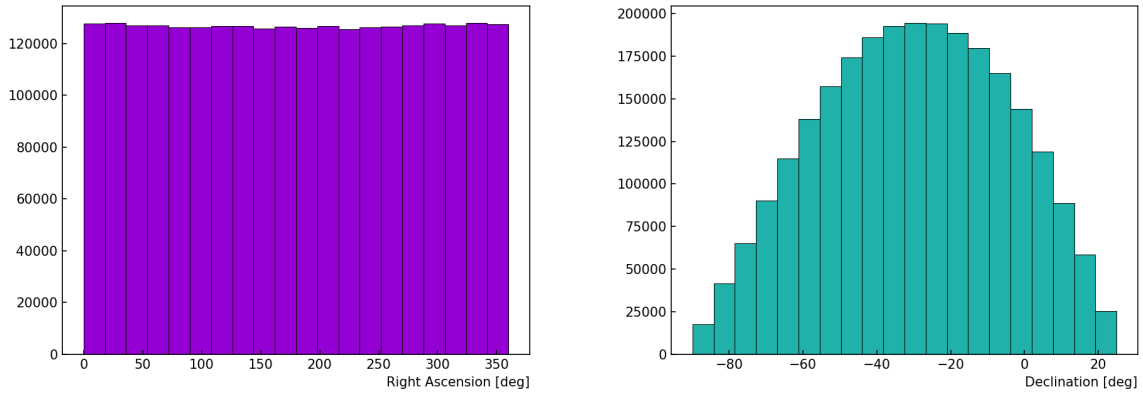

Figure 4.1: Angular distribution of the events in the cumulative vertical data set in equatorial coordinates. On the left (right), we show the right ascension (declination) histogram.

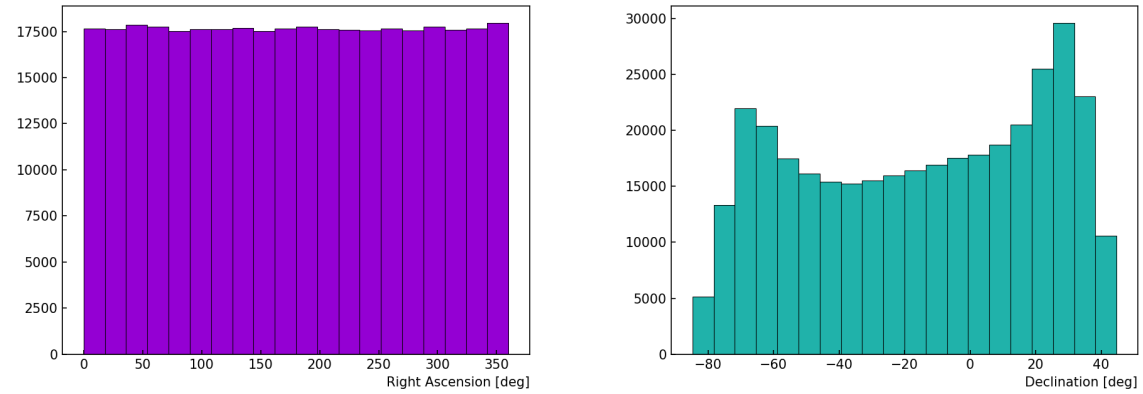

Figure 4.2: Angular distribution of the events in the cumulative inclined data set in equatorial coordinates. On the left (right), we show the right ascension (declination) histogram.

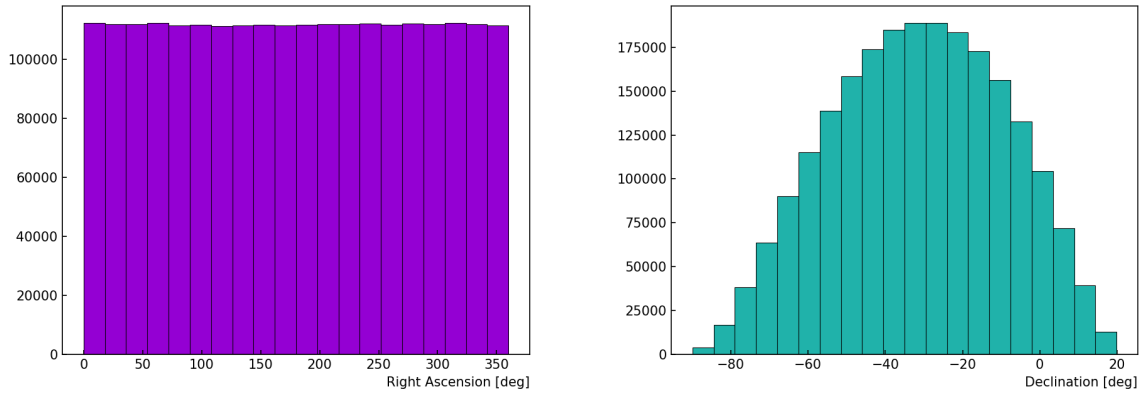

Figure 4.3: Angular distribution of the events in the cumulative infill data set in equatorial coordinates. On the left (right), we show the right ascension (declination) histogram.

stations to the one with the highest signal were active when the event occurred. The angular distribution of the cumulative vertical data set ($E \geq 1$ EeV), in equatorial coordinates,

is presented in Figure 4.1. In Figures 4.2 and 4.3, we show the angular distribution for the cumulative inclined and infill data sets, respectively.

5 NEUTRON AS A COSMIC RAY MESSENGER

Ernest Rutherford studied the structure of the atom in his famous gold foil experiment, publishing the results in 1911 [121]. Using a beam of α-particles, he investigated the deflection of such particles. He correctly interpreted the results, concluding that most part of the atom's mass was in its inner region constituting a positively charged nucleus. In 1911, it was noticed by Antonius van den Broek that since the ordinal number Z in the periodic table corresponded to half of the atomic mass and was equal to the number of electrons in each atom, Z also represented the number of positive charges in the nucleus [122]. In 1919, Francis William Aston discovered isotopes using his mass spectrograph [123], and enunciated the whole-number rule, saying that the mass of an isotope is a whole number multiple of the mass of the hydrogen atom. Due to these developments in atomic theory, in the early 1920s, Rutherford speculated that the core was constituted of protons and a type of neutral particle with a similar mass. These suspicions led to the development of experiments to identify these neutral particles. In 1932, James Chadwick discovered neutrons [124] and, three years later, won the Nobel Prize for this achievement [125]. Since then, neutrons have played a vital role in many fields of chemistry and physics. In this chapter, we discuss their importance for astroparticle physics.

Neutrons are baryons composed of three valence quarks, of which, two are quarks down and one is a quark up (ddu) [126]. Since neutrons do not have an electric charge, they are undeflected by magnetic fields, providing an appealing feature to study the arrival direction of cosmic rays – they point directly to their sources. Neutrons are heavier than protons, therefore free neutrons can decay. In general, when neutrons are bound within a nucleus, they behave as stable particles because the nuclear binding energy surpasses the mass difference between the proton and the neutron. The first observation of neutron decay was made by Snell and Miller in 1948 [127]. Free neutrons suffer β-decay through the process

$$n \rightarrow p + e^- + \overline{\nu}_e. \tag{5.1}$$

In this work, we are interested in neutrons in the EeV range. In this energy range, neutrons travel close to the speed of light. From the relativistic equation of the total energy, we can extract the Lorentz factor as a function of the energy E,

$$E = \gamma mc^2 \implies \gamma = \frac{E}{mc^2}. \tag{5.2}$$

Then, in the laboratory frame, the neutrons will travel a distance of

$$\Delta x = \gamma \Delta x_0 \approx \gamma c \Delta t_0, \tag{5.3}$$

where $\Delta t_0 = 878.6 \pm 0.6$ s is the mean lifetime for free neutrons [58]. Therefore, they can travel a distance around

$$\Delta x = \frac{c\Delta t_0}{mc^2} E = 9.2 \left(\frac{E}{\text{EeV}} \right) \text{ kpc}. \tag{5.4}$$

Since the distance to the Galactic center is around 8.3 kpc [128], neutrons with an energy of about 1 EeV can travel from the Galactic center to the Earth. Given that neutrons with energies in this range can travel distances in the order of the size of our Galaxy, we investigate Galactic candidate sources. We present more details about the candidate sources in Section 8.1. Photons in this energy range can travel longer, and for this kind of analysis, it is possible to look for extragalactic sources like the point sources at the Large Magellanic Cloud at ~ 50 kpc from Earth [27].

5.1 Neutron production in ultra-high-energy hadronic interactions

Since neutrons do not have an electric charge, they cannot be directly accelerated, which implies the existence of charged particles to explain the presence of neutron fluxes. Neutrons may be produced by heavy nuclei disintegration while interacting with matter and photons in the vicinity of the sources. However, in a spallation or photodisintegration process, the neutron will carry an energy similar to the energy per nucleon of the original nucleus. Therefore, to observe a neutron flux around 1 EeV it is necessary to turn to nuclei with several times this energy. A more efficient way to produce neutrons is in ultra-high-energy proton collisions with ambient protons or photons [129]. The possible processes to produce neutrons are the hadronic interactions with matter in proton-proton collisions, described as

$$p + p \rightarrow n + p + \pi^+, \tag{5.5}$$

and the hadronic interactions with radiation in photopion production, described as

$$p + \gamma \rightarrow n + \pi^+. \tag{5.6}$$

Both mechanisms can lead to the production of a neutron flux in the EeV range. Since proton-proton interactions can produce both γ-rays and neutrons, we can investigate γ-ray sources as candidates for EeV neutrons.

An air shower initiated by a neutron in the EeV range is indistinguishable from one initiated by a proton. A slight difference in the number of detected μ^+ and μ^- is expected at the ground level [130]. A proton shower will generate an excess of π^+, leading to an excess of μ^+, while a neutron shower will produce an excess of π^-, causing an excess of μ^-. However, the current detectors are not able to separate the μ^+/μ^- ratio, making it impossible

to distinguish between the two types of showers. Thus, we search for an excess of air shower events around a specific direction to look for evidence of neutron fluxes. The charged particles produced by a source will propagate diffusively while the neutral particles will travel in straight lines, producing local excesses pointing to the direction of the source. In the next chapters, we present three techniques to search for local excesses that could indicate a neutron flux. In the next chapter, we discuss the blind search method, looking for neutron fluxes in all the sky exposed to the Observatory. The other two methods are targeted searches, and we present them in Chapters 8 and 10.

6 BLIND SEARCH FOR POINT SOURCES OF NEUTRONS

Identifying sources of ultra-high-energy cosmic rays (UHECRs) is one of the most important questions for astroparticle physics. One tool to understand the origin of these particles is to study neutral particles. Since they are undeflected by magnetic fields, they travel in straight lines pointing directly to their sources. Due to the undeflected neutral particles, an event excess around a specific direction could indicate a neutron flux.

Free neutrons are unstable due to the β-decay process. However, ultra-high-energy neutrons can travel astronomical distances. Considering relativistic effects, neutrons can travel a distance of $9.2 \times E/\text{EeV}$ kpc. Therefore, neutrons with 1 EeV can reach Earth from the Galactic center, and above 2 EeV, we are considering neutrons from almost the whole volume of our Galaxy.

Since air showers initiated by protons are indistinguishable from those generated by neutrons, we expect to observe local excesses of events caused by a neutral particle flux from the direction of a source. Charged particles in the EeV range are slightly deflected by magnetic fields in the Galaxy, while neutrons travel in straight lines, possibly causing an excess in a solid angle around their sources. In this chapter, we present a method to study the arrival direction distribution of cosmic rays to identify surpluses of events that could indicate a neutron flux.

In this chapter, we present a method to search for point sources of neutrons in the sky exposed to the Observatory. The procedure consists of defining target regions, maximizing the signal-to-noise ratio, and comparing the observed number of events with the one expected from the background. The expected number of events is obtained from simulations smoothing the arrival direction distribution to erase small-scale anisotropies, providing a background signal. We also present a procedure to estimate the upper limit of the neutron flux.

6.1 Estimating the size of the target region

The angular resolution is the angle containing 68% of the arrival directions from a source. Assuming a density signal spread proportional to a symmetrical two-dimensional Gaussian distribution, the total signal collected inside a solid angle with opening angle ψ is propor-

tional to

$$\mathscr{S} \propto \int_0^{2\pi}\int_0^{\psi} \frac{1}{2\pi\overline{\sigma}^2}\exp\left[-\frac{\zeta^2}{2\overline{\sigma}^2}\right]\sin\zeta\, d\zeta\, d\upsilon = \int_0^{\psi}\frac{\zeta}{\overline{\sigma}^2}\exp\left[-\frac{\zeta^2}{2\overline{\sigma}^2}\right]d\zeta, \tag{6.1}$$

where we used the approximation $\sin\zeta \approx \zeta$ for small values of ζ. Even though ζ and υ are equivalent to the usual spherical coordinates, we do not call them θ and φ to avoid confusing them with the local coordinates. For the angle ψ to represent the angular resolution, we impose that the signal collected inside the solid angle defined by ψ is 68% of the total signal. Therefore,

$$\int_0^{\psi}\frac{\zeta}{\overline{\sigma}^2}\exp\left[-\frac{\zeta^2}{2\overline{\sigma}^2}\right]d\zeta = 0.68 \implies \psi = 1.51\overline{\sigma}. \tag{6.2}$$

Equation 6.2 relates the angular resolution with the width $\overline{\sigma}$. We can obtain the $\overline{\sigma}$ parameter from the uncertainties in the zenith and azimuth angles,

$$\overline{\sigma} = \sqrt{\frac{(\Delta\theta)^2 + (\sin\theta_0\Delta\varphi)^2}{2}}, \tag{6.3}$$

where θ_0 is the reconstructed zenith angle, $\Delta\theta$ and $\Delta\varphi$ are the uncertainties in the zenith and the azimuth angles, respectively. We present the details of the local coordinate system in Appendix A. We present the deduction of the Equation 6.3 in Section B.1.

Let us consider a source emitting N cosmic rays and impose that, within a solid angle defined by ψ, we will collect 68% of the signal:

$$\int_0^{\psi}\sum_{i=1}^{N}\frac{\zeta}{\overline{\sigma}_i^2}\exp\left[-\frac{\zeta^2}{2\overline{\sigma}_i^2}\right]d\zeta = 0.68N. \tag{6.4}$$

Manipulating Equation 6.4, we obtain

$$\frac{1}{N}\int_0^{\psi}\sum_{i=1}^{N}\frac{\zeta}{\overline{\sigma}_i^2}\exp\left[-\frac{\zeta^2}{2\overline{\sigma}_i^2}\right]d\zeta = 0.68 \implies \frac{1}{N}\sum_{i=1}^{N}\exp\left[-\frac{\psi^2}{2\overline{\sigma}_i^2}\right] = 0.32. \tag{6.5}$$

From the last part, we can obtain the angular resolution ψ numerically. The uncertainties in the local angles have a slight dependence on declination. We use events in 5-degree bins of declination to estimate the angular resolution. We fit curves using the results from the 5-degree intervals to determine the angular resolution for the declination of each target. In Section 7.3, we present more details about the angular resolution estimation.

Our goal is to obtain the angle χ that maximizes the signal-to-noise ratio. In a region defined by the angle χ, the number of events collected is proportional to χ^2. Since the noise is roughly proportional to the square root of this number, the noise is proportional to

χ. On the other hand, the signal inside this region is

$$\mathscr{S} \propto \int_0^{\chi} \frac{\zeta}{\overline{\sigma}^2} \exp\left[-\frac{\zeta^2}{2\overline{\sigma}^2}\right] d\zeta = 1 - \exp\left(-\frac{\chi^2}{2\overline{\sigma}^2}\right). \tag{6.6}$$

Therefore, by maximizing the signal-noise ratio, we have

$$\frac{d}{d\chi}\left(\frac{1-\exp\left(-\frac{\chi^2}{2\overline{\sigma}^2}\right)}{\chi}\right) = 0. \tag{6.7}$$

Solving this equation, we obtain

$$\chi = 1.59\overline{\sigma} = 1.05\psi, \tag{6.8}$$

where, in the last step, we used the result from Equation 6.2. The angle χ represents the optimized opening angle to define the target region. From the curve fits of the angular resolution, we can estimate the angular resolution for each target region, using the declination of the target, and then scale this value by 1.05 to obtain the size of the opening angle that defines the target region.

6.2 Determining the target directions in the sky

The work published by the Collaboration in 2012 [1] uses the HEALPix library [131] to pixel the sky. HEALpix stands for **H**ierarchical **E**qual **A**rea iso**L**atitude **Pix**elation of a sphere. It divides the surface of a sphere into quadrilateral pixels of equal area. The number of pixels is defined by the N_{side} parameter. For computational reasons, in this work, we used Healpy [132], a library in Python used to pixelate a map in spherical coordinates based on HEALPix. The sky is pixelated using the N_{side} parameter equal to 128. The center of each pixel defines a target direction.

Once defined the target region, by scaling the angular resolution obtained with the curve fits, as explained in Section 6.1, by 1.05 (Equation 6.8), we use a finer pixelation using $N_{\text{side}} = 512$ and count the number of events inside these pixels. In this way, each target region is the union of the smaller pixels within the circle defined by the angle χ and centered in the direction of the target.

6.3 Producing the background estimation

To evaluate the background, we use the scrambling technique [133]. This method uses the observed data set to preserve the exposure of the Observatory. We shuffle the observed data set, thus erasing local anisotropies. By repeating this procedure enough times, we can obtain

a reliable background signal. For this thesis, we simulate 10,000 data sets, and the mean value obtained inside a target region is used to estimate the expected signal.

To simulate a direction in the sky, we sample two events from the actual data set. From the first event, we extract information about its detection time, and from the second, the zenith angle. We sample an azimuth angle from a uniform distribution between 0 and 2π. Using the time information combined with the local coordinates of the simulated event, we obtain a unique direction in the sky. We build data sets with sizes identical to the observed ones.

6.4 The Li-Ma significance

The Li-Ma significance was first used to study γ-ray bursts. The method proposed by Ti-Pei Li and YuQian Ma uses the time of observation of a candidate source, t_{on}, and the time observing the background contribution, t_{off}. Then, the ratio α is defined as the on- and off-source time, i.e., $\alpha \equiv t_{\text{on}}/t_{\text{off}}$. In the time t_{on} (t_{off}), N_{on} (N_{off}) photons are observed. Since we expect the background contribution in the time t_{on} to be αN_{off}, the probable number of photons produced by the source is $N_S = N_{\text{on}} - \alpha N_{\text{off}}$.

Using the statistical hypothesis called "null hypothesis", Li and Ma proposed in [134] the following significance of an observed result:

$$S = \sqrt{2}\left\{N_{\text{on}} \ln\left[\frac{1+\alpha}{\alpha}\left(\frac{N_{\text{on}}}{N_{\text{on}}+N_{\text{off}}}\right)\right] + N_{\text{off}} \ln\left[(1+\alpha)\left(\frac{N_{\text{off}}}{N_{\text{on}}+N_{\text{off}}}\right)\right]\right\}^{1/2}. \tag{6.9}$$

In our analysis, we are looking for excesses in regions of the sky, i.e., we are doing a spatial search instead of a temporal one, as is done for γ-ray bursts. To adapt the procedure to our analysis, we can replace the observed number of photons in the on-source time, N_{on} by the observed number of events in a target region, n, and redefine α as $\alpha \equiv b/N_{\text{off}}$ where b is the expected number of events in the background and N_{off} is the expected number of events outside the target region. In this way, the significance is given by

$$S = \frac{n-b}{|n-b|}\sqrt{2}\left[n \ln\left(\frac{n+\alpha n}{b+\alpha n}\right) + \frac{b}{\alpha}\ln\left(\frac{b+\alpha b}{b+\alpha n}\right)\right]^{\frac{1}{2}}. \tag{6.10}$$

The interpretation of S is the number of standard deviations of the observed signal from the expected one. We can have positive and negative values of S. The positive values are associated with an excess of events, while the negative ones are interpreted as a deficit of events. For example, if we obtain for a target $S = +4$, that means that we are observing an excess of events around this target. In this case, the observed result deviates 4σ from the expected (a 4σ significance). If S is equal to -4, this result is also deviating 4σ from the expected, but instead of an excess, we are observing a deficit of events. If $S = 0$, we are

observing exactly what is expected from the background ($n = b$). In our analysis, we are searching for neutron fluxes through excesses. So, we are interested in the positive values of S. The larger the value of S, the more significant is the target.

6.5 Upper limit on the neutron flux

The chosen definition for the signal upper limit, s_{UL}, was the Zech's procedure [135] to avoid negative values:

$$P(\leq n|b+s_{UL}) = (1-\mathrm{CL})\cdot P(\leq n|b), \tag{6.11}$$

where CL represents the confidence level. In this work, we will use CL = 0.95. Here, $P(\leq n|b)$ represents the probability of getting n or fewer events in the presence of a background following a Poisson distribution with mean b. For a Poisson process, this definition agrees with the Bayesian upper limit with flat prior,

$$\int_0^{s_{UL}} P(n|b+s)ds = \mathrm{CL}\int_0^{\infty} P(n|b+s)ds, \tag{6.12}$$

where $P(n|b+s)$ represents the probability mass function of a Poisson distribution,

$$P(n|b+s) = \frac{(b+s)^n e^{-(b+s)}}{n!}. \tag{6.13}$$

If the target region is a solid angle with opening angle χ, the collected signal inside the region is given by

$$\mathscr{S} \propto \int_0^{\chi} \frac{\zeta}{\overline{\sigma}^2}\exp\left[-\frac{\zeta^2}{2\overline{\sigma}^2}\right]d\zeta = 1-\exp\left(-\frac{\chi^2}{2\overline{\sigma}^2}\right) \approx 0.717, \tag{6.14}$$

where we used $\chi = 1.59\overline{\sigma}$ (Eq. 6.8). Therefore, the signal inside the target region is 71.7% of the total, and we must scale the upper limit on the number of neutrons by a factor $1/0.717 = 1.39$. The upper limit on the flux of neutrons is the upper limit on the number of neutrons obtained from Equation 6.12 divided by the directional exposure.

To determine the directional exposure, we take the expected number of events within a target region and divide it by the cosmic ray intensity and the solid angle of the target region. We can estimate the cosmic ray intensity by integrating the energy spectrum in the energy range of interest. The Pierre Auger Collaboration published several works regarding the cosmic ray energy spectrum for energies above 0.1 EeV. We present more details about the cosmic ray intensity calculation in Section 7.2. The solid angle of the target region is given by

$$\Delta\Omega = \int_0^{2\pi}\int_0^{\chi} \sin\zeta\, d\zeta\, d\upsilon = 2\pi(1-\cos\chi). \tag{6.15}$$

Finally, the directional exposure is given by

$$\omega_{dir} = \frac{b}{I \cdot \Delta\Omega}, \tag{6.16}$$

and the upper limit on the neutron flux is given by

$$\Phi_{UL} = 1.39 \frac{s_{UL}}{\omega_{dir}}, \tag{6.17}$$

where we estimated s_{UL} using Equation 6.12.

We performed the blind search on three different data sets: the vertical, the inclined, and the infill set. We present a description of the data sets used in Chapter 4. The results obtained with the method described in this chapter are presented in Chapter 7. After performing a blind search, we can restrict the tested targets, focusing on directions where we have candidate sources. In Chapter 8, we describe a method to search only in specific directions, explaining which are the astrophysical objects that are candidates to produce UHECRs.

7 RESULTS FOR THE BLIND SEARCH

In this chapter, we discuss the main results obtained using the data sets described in Chapter 4 for the blind search described in Chapter 6. We try to identify a neutron flux searching for excesses around the direction of each one of the tested targets, giving its significance. The larger the target significance, the larger the excess from its position. In addition to the significance of each target, we can estimate an upper limit on the neutron flux from its position. This upper limit depends on the cosmic ray intensity obtained by integrating the known spectrum and normalizing using the total exposure of the array above the full efficiency energy and the number of events for this energy range. In Section 7.1, we present the results for the total exposure of the array, considering the full array and the infilled portion, that are used in the cosmic ray intensity estimation, presented in Section 7.2. We use a top-hat function to determine the size of the target region in which we search for an excess. This target size depends on the angular resolution. The results for the angular resolution as a function of the declination are presented in Section 7.3. In Section 7.4, we present the results for the blind search, including the significance obtained with the Li-Ma formula and the upper limit for the field of view reached with each data set.

7.1 Total Exposure

The total exposure is the effective area of the Observatory integrated in time. For events above 3×10^{18} eV, the Observatory reaches full efficiency[1], and it is possible to estimate the total exposure geometrically. We can define a *cell* based on a sub-array of detectors. We estimate the total exposure by integrating the number of active cells at each instant in time and in solid angle:

$$\omega_{\text{total}} = \int_{\Delta t}\int_{\Delta\Omega} a_{\text{cell}} \cdot \cos\theta \cdot N_{\text{cell}}(t)\, d\Omega\, dt. \tag{7.1}$$

The factor $a_{\text{cell}} \cdot \cos\theta$ indicates the projection of the area of each cell for an air shower arriving at a zenith angle θ. The total number of active cells $N_{\text{cell}}(t)$ is constantly monitored at the Observatory. The area of each cell depends on the number of active stations. In the analysis presented in this work, we selected only events in which all six stations around the one with the highest signal were active at the instant the event had occurred. For this configuration, the area of the unit cell, a_{cell}, is 1.95 km^2 for the full array and 0.49 km^2 for the infilled one. In Figure 7.1, we present a scheme of the unit cell and a representation of a set of active cells. We integrate Equation 7.1 over all possible values for the azimuth and the zenith angles. The

[1] The infilled array reaches full efficiency above 3×10^{17} eV.

azimuth angles vary from $-180°$ to $180°$ for all data sets, and the zenith angles from 0 to $60°$ for the vertical data set, resulting in

$$\int_{\Delta\Omega} a_{\text{cell}} \cos\theta \, d\Omega = 4.59 \text{ km}^2 \text{ sr}. \tag{7.2}$$

For the inclined data set, in which we have $60° \leq \theta \leq 80°$, we have an integrated projected area of $1.35\,\text{km}^2$ sr, and for the infill ($0 \leq \theta \leq 55°$), we have $1.03\,\text{km}^2$ sr. We present the results for the total exposure for each data set used in this work in Table 7.1. We use the total exposure to estimate the cosmic-ray intensity as presented in the next section.

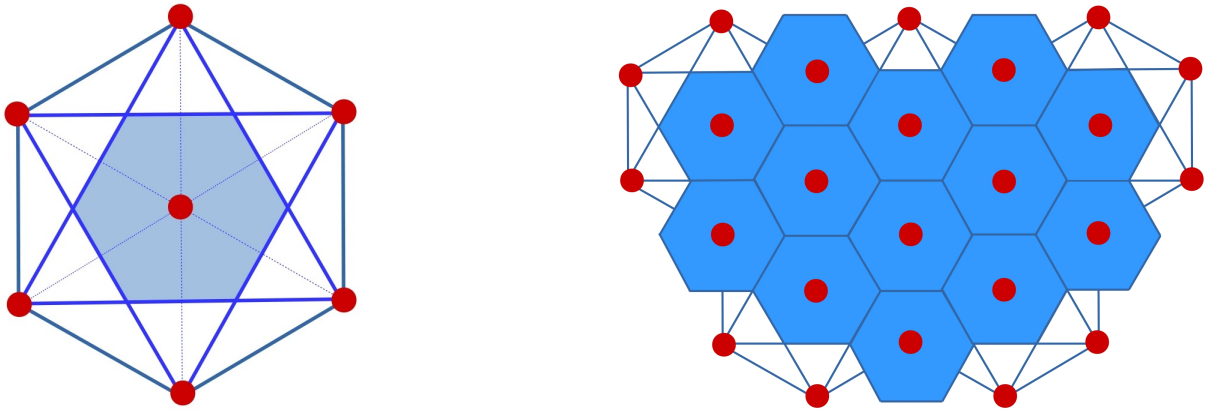

Figure 7.1: Scheme of the cells of the SD detector. On the left, we have a single cell defined by the central station and its six neighbors. The area of the cell corresponds to the region shaded in blue. On the right, we have an array of active cells. Each dot represents a water-Cherenkov station.

Table 7.1: Total exposure for the Pierre Auger Observatory array for each data set.

Total exposure [km^2 yr sr]		
Vertical	**Inclined**	**Infill**
79,865	23,411	405

7.2 Cosmic-ray Intensity

We obtain the cosmic-ray intensity by integrating the spectrum shape. The Auger Collaboration has studied extensively the energy spectrum for cosmic rays with the highest energies. From one of these works [34], we extracted the equation that fits the cosmic ray data in the energy range we are interested in:

$$J(E;\mathbf{s}) = J_0 \left(\frac{E}{E_0}\right)^{-\gamma_1} \prod_{i=1}^{3} \left[1 + \left(\frac{E}{E_{ij}}\right)^{\frac{1}{\omega_{ij}}}\right]^{(\gamma_i - \gamma_j)\omega_{ij}}. \tag{7.3}$$

In this equation, $\mathbf{s}$ represents the fit parameters. We report the parameters of the best fit for the function in Equation 7.3 in Table 7.2. The cosmic-ray intensity is estimated using the

relation given by

$$I = I_0 \int_{E_i}^{E_f} J(E;\mathbf{s})\,dE, \tag{7.4}$$

and normalized using the constant I_0. We obtain I_0 using the following condition: the cosmic-ray intensity above the energy of full efficiency times the total exposure (Section 7.1) of the array must result in the total number of events for this energy range,

$$N_{\text{ev}}(E \geq E_{\text{full eff}}) = \omega_{\text{total}} \cdot I(E \geq E_{\text{full eff}}). \tag{7.5}$$

Table 7.2: Parameters for the spectrum energy fit extracted from [34].

Parameters for the spectrum energy fit	
Parameter	**value** $\pm\sigma_{stat} \pm \sigma_{sys}$
γ_1	$3.29 \pm 0.02 \pm 0.10$
γ_2	$2.51 \pm 0.03 \pm 0.05$
γ_3	$3.05 \pm 0.05 \pm 0.10$
γ_4	$5.1 \pm 0.3 \pm 0.1$
E_{12} [eV]	$(5.0 \pm 0.1 \pm 0.8) \times 10^{18}$
E_{23} [eV]	$(13 \pm 1 \pm 2) \times 10^{18}$
E_{34} [eV]	$(46 \pm 3 \pm 6) \times 10^{18}$

Using Equation 7.4 with the energy spectrum shape given by Equation 7.3 and the parameters for $J(E;\mathbf{s})$ presented in Table 7.2, we obtained the results for the cosmic-ray intensity. These results are displayed in Table 7.3. The cosmic ray intensity is used to estimate the upper limit of the neutron flux.

Table 7.3: Cosmic ray intensity for each data set and each energy range.

Cosmic-ray intensity [km^{-2} yr^{-1} sr^{-1}]				
Energy range	**Vertical**	**Inclined**	**Energy range**	**Infill**
$E \geq 1$ EeV	33.06	38.40	$E \geq 0.1$ EeV	7276.94
$E \geq 3$ EeV	2.99	3.47	$E \geq 0.3$ EeV	588.31
$1 \leq E/\text{EeV} \leq 2$	26.03	30.23	$0.1 \leq E/\text{EeV} \leq 0.2$	5788.67
$2 \leq E/\text{EeV} \leq 3$	4.05	4.70	$0.2 \leq E/\text{EeV} \leq 0.3$	899.96

7.3 Angular Resolution

We define a target region to search for excesses of cosmic ray events to investigate a neutron flux. The opening angle that defines this region is given by a factor times the angular

resolution (Equation 6.8). We use the declination of the target to calculate the angular resolution. The first step to obtaining the angular resolution is to divide the events into 5-degree declination intervals and estimate the angular resolution using the procedure described in Section 6.1, using Equation 6.5 for the N showers inside each bin. The vertical data sets result in Gaussian distributions, and we use Gaussian functions to fit the data. The dots are obtained with the data, and the curves are the results of the Gaussian fits. We present the results for the fit parameters in Table 7.2. Figure 7.2 shows both the results using the data and the Gaussian fits.

Table 7.4: Parameters for the angular resolution for the Gaussian fit for the vertical data set.

Angular resolution parameters - Vertical			
Energy range	**peak [deg]**	**center [deg]**	**sigma [deg]**
$E \geq 1$ EeV	1.36	−34.7	55.8
$E \geq 3$ EeV	0.72	−34.3	53.9
$1 \leq E/\text{EeV} \leq 2$	1.49	−34.8	57.1
$2 \leq E/\text{EeV} \leq 3$	1.06	−34.4	55.8

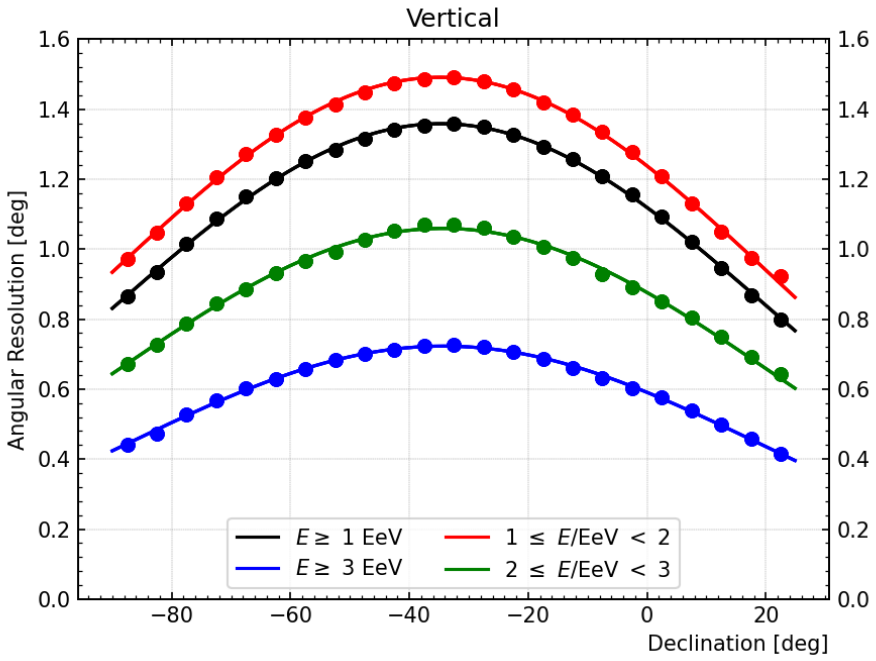

Figure 7.2: Angular resolution as a function of the declination for each energy range for the vertical data set. The continuous curves represent the Gaussian fits, and the dots represent the results for 5-degree intervals in declination.

For the inclined and the infill data sets, the angular resolution as a function of declination does not follow a Gaussian distribution. Hence, for these two data sets, we use

instead a polynomial fit using a function of degree 9, as we can observe in Figures 7.3 and 7.4. For all three data sets, we take the declination of the target and use the fit parameters of the angular resolution to estimate the angular resolution at the position of the target, and then use Equation 6.8 to calculate the size of the target region.

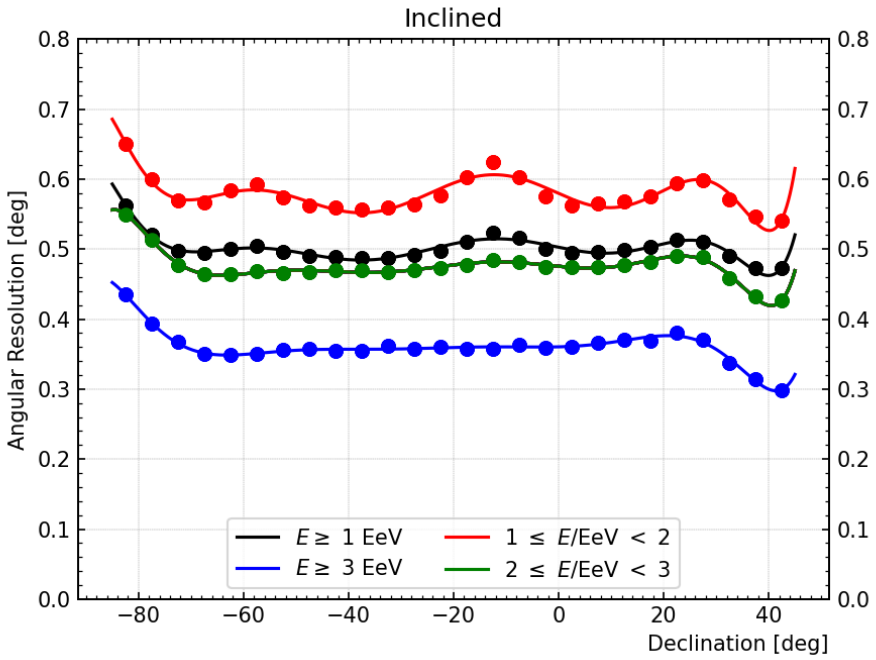

Figure 7.3: Angular resolution as a function of the declination for each energy range for the inclined data set. The continuous curves represent the polynomial fit using a function of degree 9, and the dots represent the results for 5-degree intervals in declination.

7.4 Results for the blind search

The blind search is used to investigate neutron fluxes from targets covering the whole field of view allowed by each data set. The first step is to define the target centers using HealPy, respecting the field of view that each data set allows. Then, we use the results for the angular resolution presented in Figures 7.2, 7.3, and 7.4 to estimate the target size using Equation 6.8. In the following, we compare the observed number of events in this target region with the expected value. The expected number of events is obtained using 10,000 simulated data sets produced with the scrambling method.

We apply this method on three data sets: the vertical (events with a zenith angle $\theta \leq 60°$), the inclined (events with a zenith angle between 60° and 80°), and the infill (events recorded by the infilled portion of the array). These data sets were described in Chapter 4. In the following subsections, we report the results obtained with each one of them.

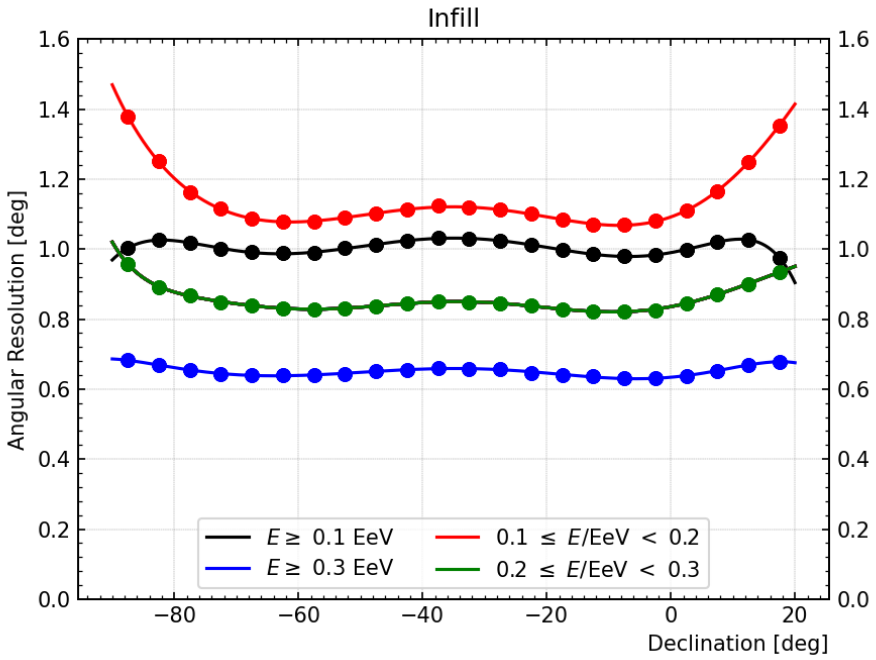

Figure 7.4: Angular resolution as a function of the declination for each energy range for the infill data set. The continuous curves represent the polynomial fit using a function of degree 9, and the dots represent the results for 5-degree intervals in declination.

7.4.1 Vertical data set

The mean directional exposure for the vertical data set falls below 2,500 km^2 yr for declination angles above 20°, as we can observe in Figure 7.5, and because of this, we considered targets with declinations below this value. We obtained this figure by taking the mean value in 3-degree intervals in declination. For the vertical data set, we used the parameters from the fit of the angular resolution presented in Table 7.4 and Figure 7.2 combined with Equation 6.8 to obtain the size of each target region as a function of declination. The next step is to determine the observed number of events n and the expected number of events b using 10,000 simulated data sets obtained with the scrambling technique. Then, we evaluated the significance of each target using the Li-Ma formula presented in Equation 6.9. Figure 7.6 presents the results for the Li-Ma significance for each energy range for the vertical data set. On the left, we have the histograms with the Li-Ma significance. As we can see in this figure, in all energy ranges, the histograms follow a Gaussian distribution, indicating that the targets present a significance distribution as expected if we do not have significant excesses. The figure also presents the expected distribution of the significance values. The expected distribution is obtained by taking each one of the simulated data sets and using it as the observed data set in Li-Ma's formula (Equation 6.9). We used the remainder data sets as background. The expected distribution represents the mean of this procedure using 10,000 simulations. The integral curves are useful to study the tails of the distributions since one is the number of targets above a certain σ value, and the other is the number of targets below

this value. The gray shaded areas represent the expectation of 95% of the simulations.

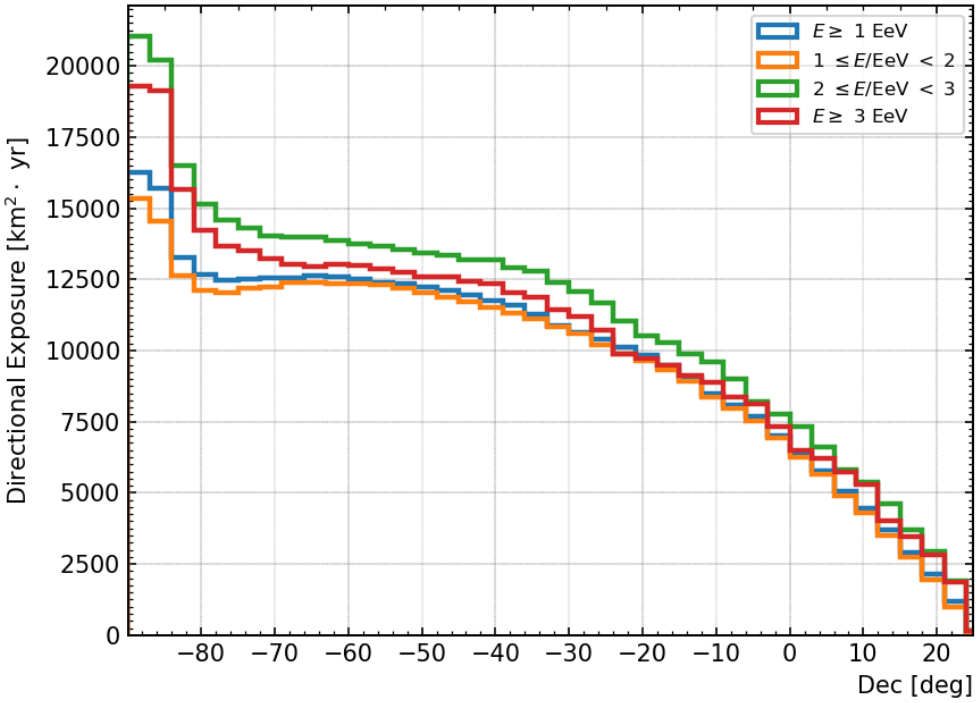

Figure 7.5: Mean directional exposure as a function of the declination for the vertical data set. The mean is obtained by taking 3-degree intervals in declination.

The mean expected number of events within the target regions as a function of declination is presented in Figure 7.7. The work published by the Auger Collaboration in [1] investigated neutron fluxes using vertical events recorded from 2004 to 2011. For this thesis, we include events recorded by the SD up to 2022. In [1], no evidence of a neutron flux was found. Our results obtained with the updated vertical data set reinforce these previous results.

We can estimate the flux upper limit using the procedure described in Section 6.5. Figure 7.8 represents the results for the vertical data set in the four energy ranges in Galactic coordinates. The flux upper limits obtained by the Collaboration in [1] vary from $0.0025\,\mathrm{km^{-2}\,yr^{-1}}$ to $0.035\,\mathrm{km^{-2}\,yr^{-1}}$ ($E \geq 1$ EeV), $0.0027\,\mathrm{km^{-2}\,yr^{-1}}$ to $0.037\,\mathrm{km^{-2}\,yr^{-1}}$ ($1\,\mathrm{EeV} \leq E < 2\,\mathrm{EeV}$), $0.00072\,\mathrm{km^{-2}\,yr^{-1}}$ to $0.017\,\mathrm{km^{-2}\,yr^{-1}}$ ($2\,\mathrm{EeV} \leq E < 3\,\mathrm{EeV}$), and $0.00071\,\mathrm{km^{-2}\,yr^{-1}}$ to $0.011\,\mathrm{km^{-2}\,yr^{-1}}$ ($E \geq 3\,\mathrm{EeV}$). Figure 7.9 presents the mean upper limit flux as a function of the declination. The mean value is obtained by averaging the results obtained for the targets within 3-degree intervals.

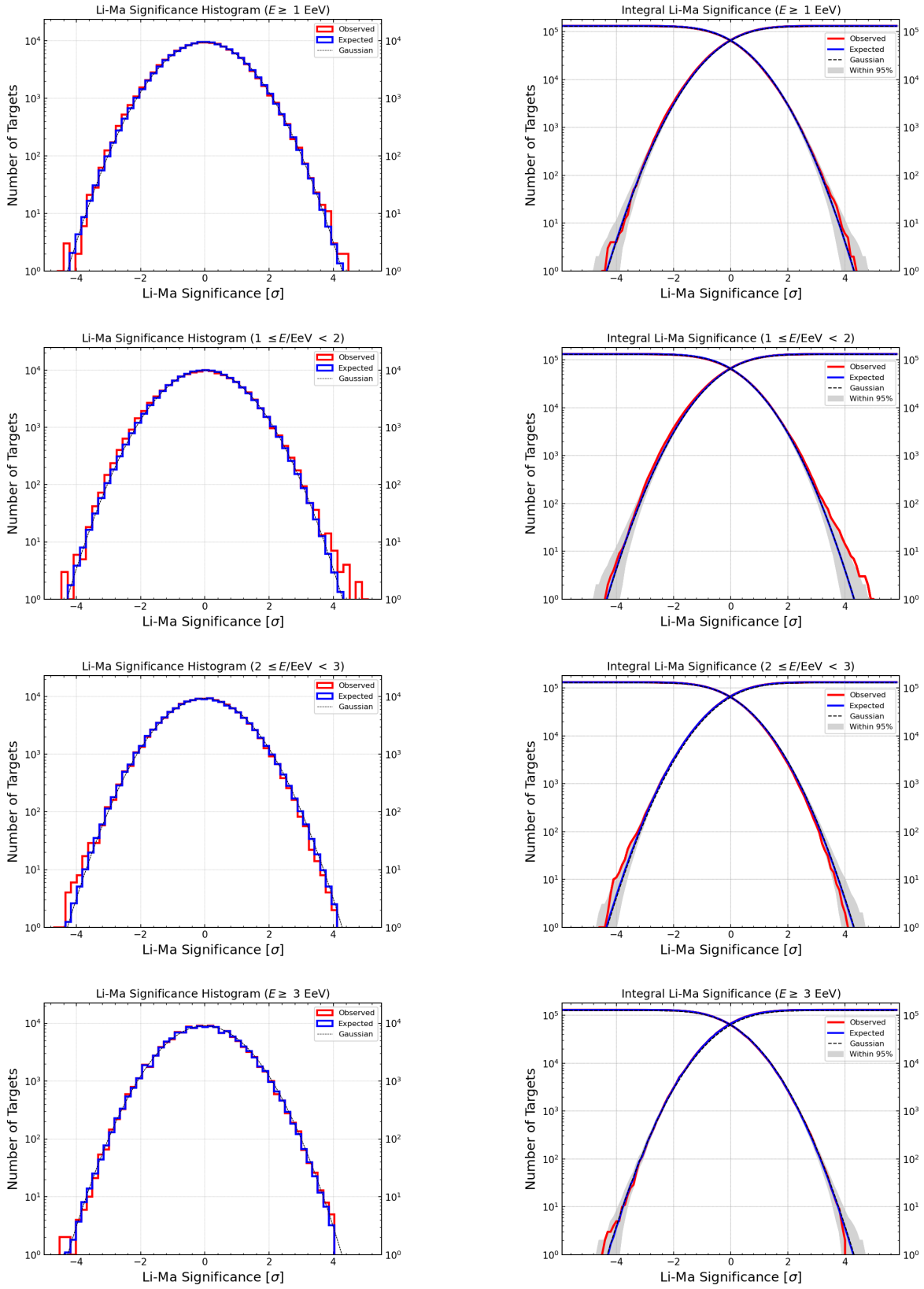

Figure 7.6: Li-Ma significance results for the vertical data set.

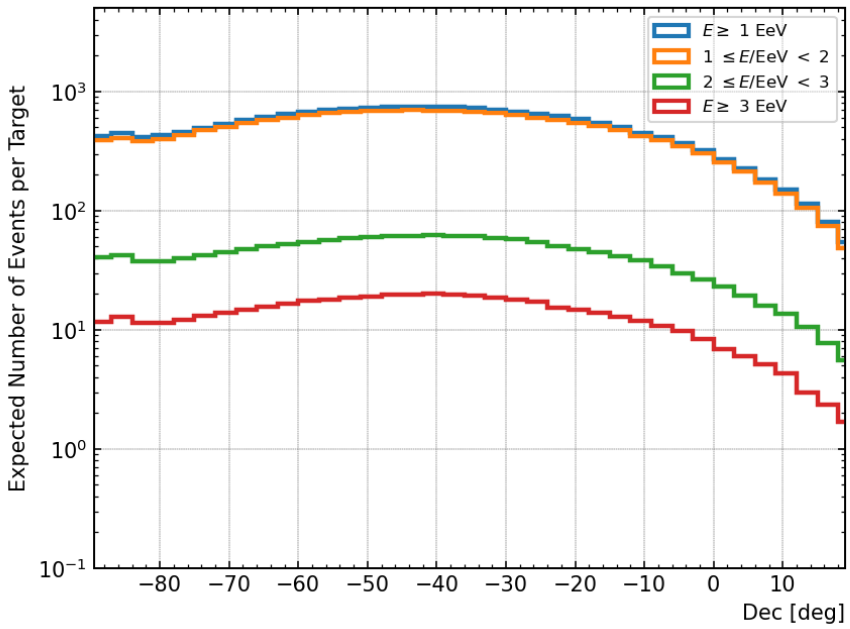

Figure 7.7: Expected number of events in each target region as a function of the declination for the vertical data set. The mean is obtained by taking 3-degree intervals in declination.

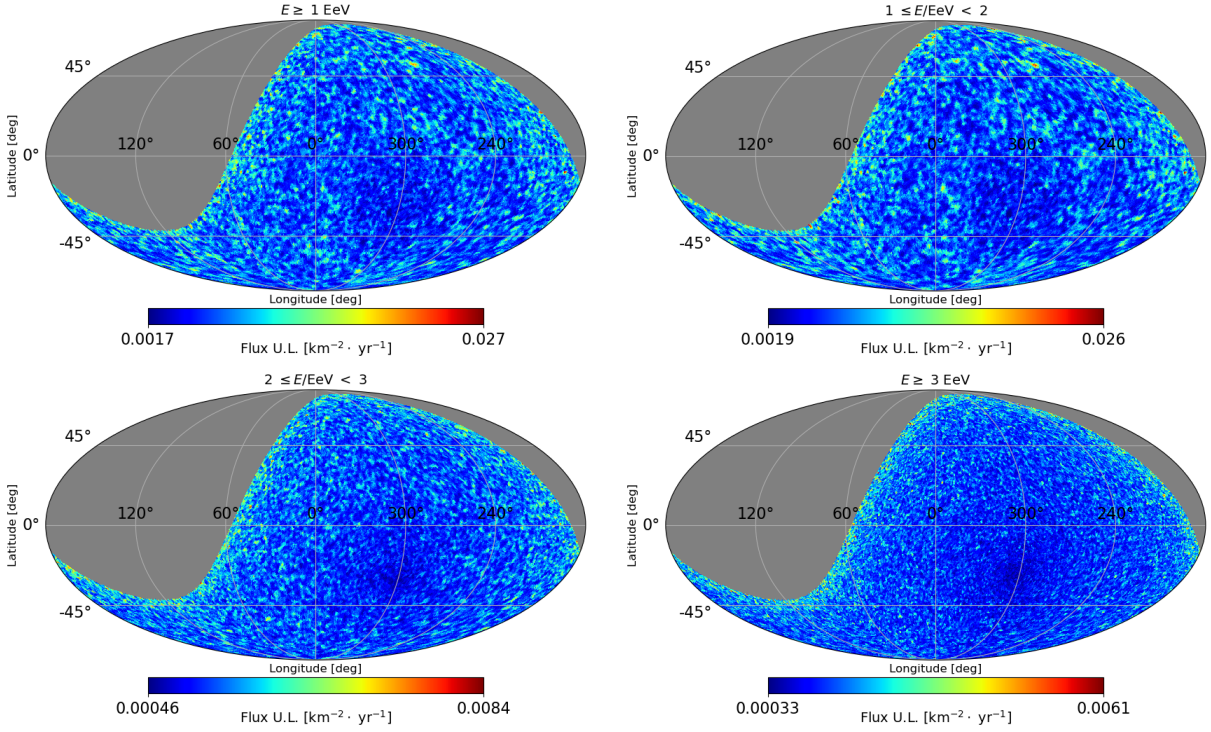

Figure 7.8: The upper limit on the flux of neutrons for each energy range for the vertical data set in Galactic coordinates.

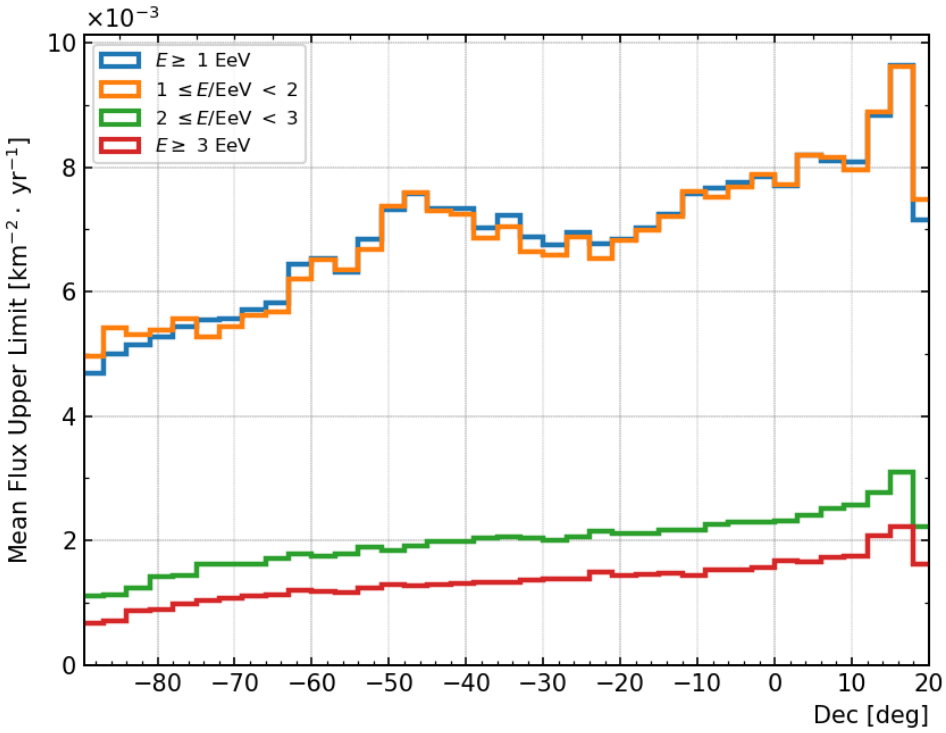

Figure 7.9: Mean flux upper limit as a function of the declination for the vertical data set. The mean is obtained by taking 3-degree intervals in declination.

7.4.2 Inclined data set

We studied the inclined data set in the neutron analysis for the first time. In Figure 7.10, we can observe the directional exposure as a function of the declination for the inclined events. Based on the directional exposure, we used the targets between $-80°$ and $35°$ to estimate the Li-Ma significance, presented in Figure 7.12, and the upper limit on the flux of neutrons shown in Figure 7.13. Figure 7.11 presents the mean value for the number of events inside each target region. We obtained the mean value by taking the expected number of events inside each target region for the targets within a 3-degree interval in declination and averaging.

Figure 7.12 shows the histograms with the significance of the targets obtained with Equation 6.9 for each energy range and the integral curves. The distributions follow the same pattern that would be expected from a Gaussian distribution, indicating that we do not have significant targets for this data set. For the inclined events, we have fewer events than the vertical and infill data sets, as we presented in Table 4.1. Since we have fewer events, we have more statistical fluctuations.

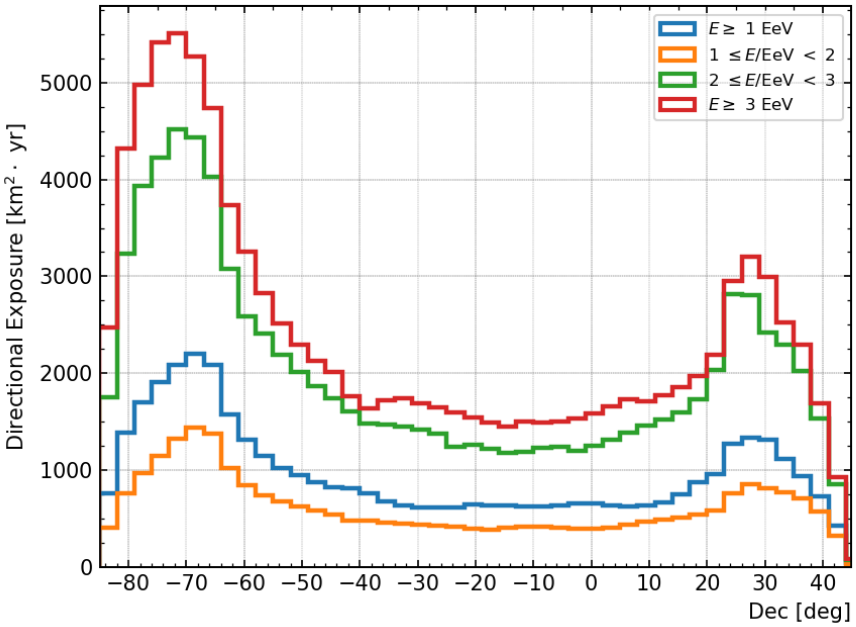

Figure 7.10: Mean directional exposure as a function of the declination for the inclined data set. The mean is obtained by taking 3-degree intervals in declination.

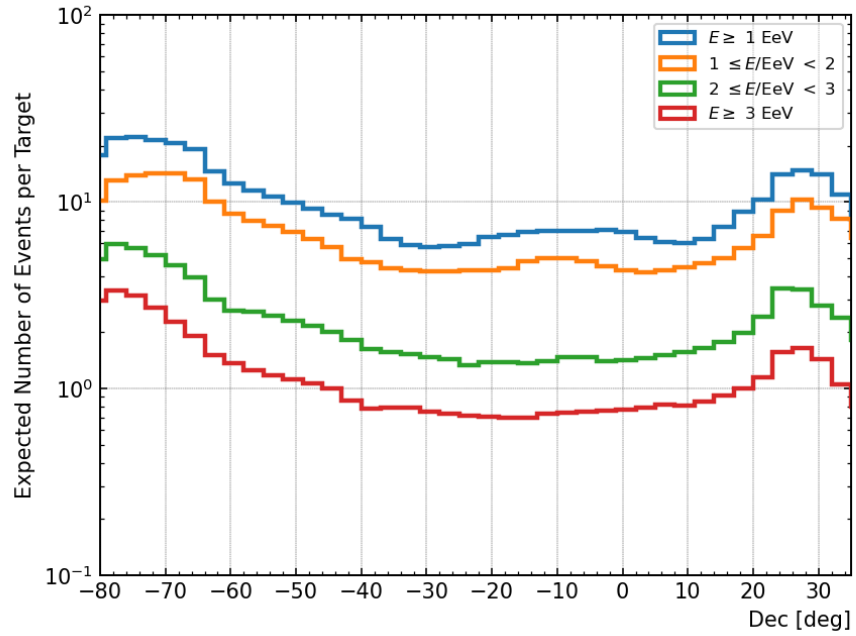

Figure 7.11: Expected number of events in each target region as a function of the declination for the inclined data set. The mean is obtained by taking 3-degree intervals in declination.

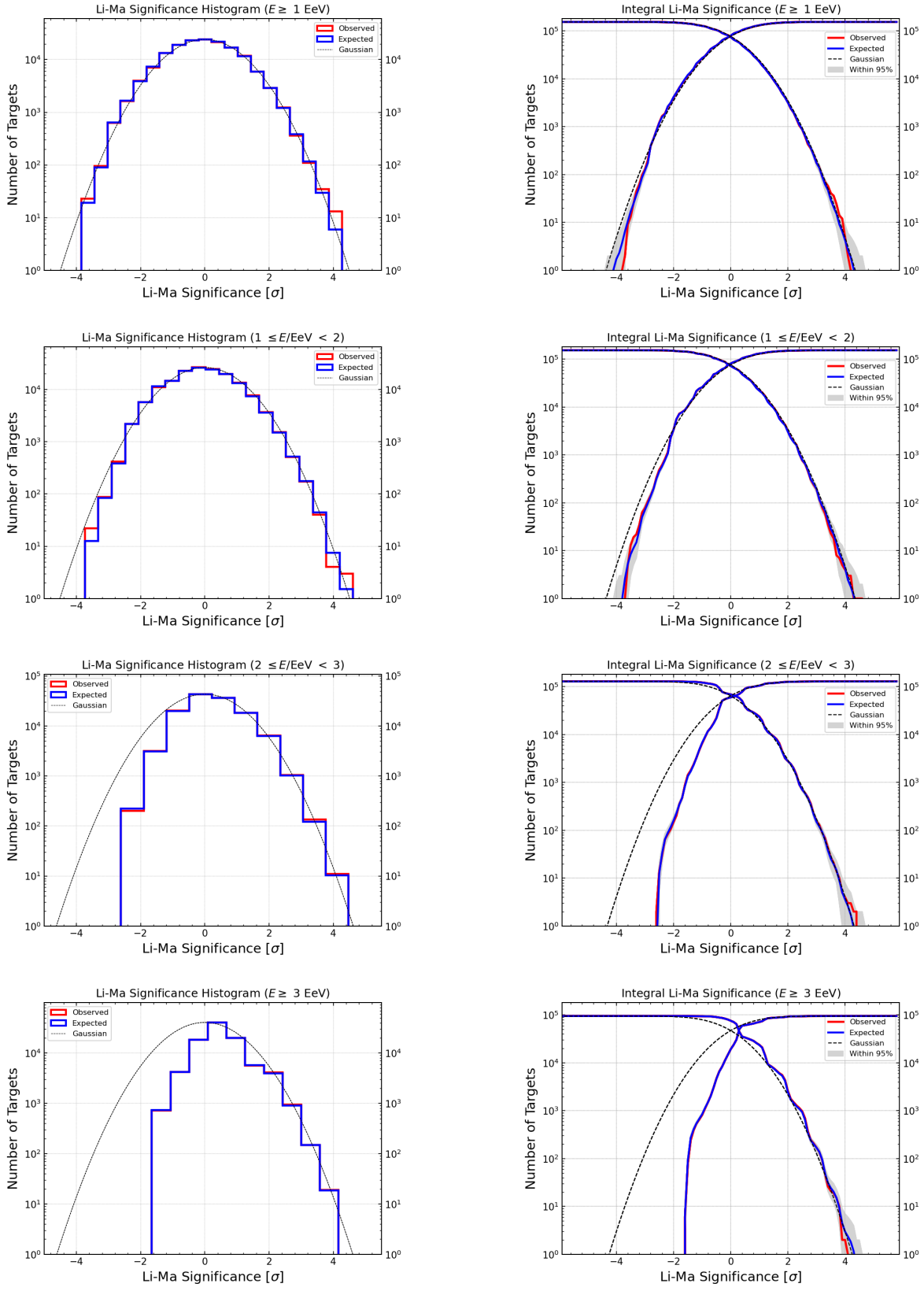

Figure 7.12: Li-Ma significance results for the inclined data set.

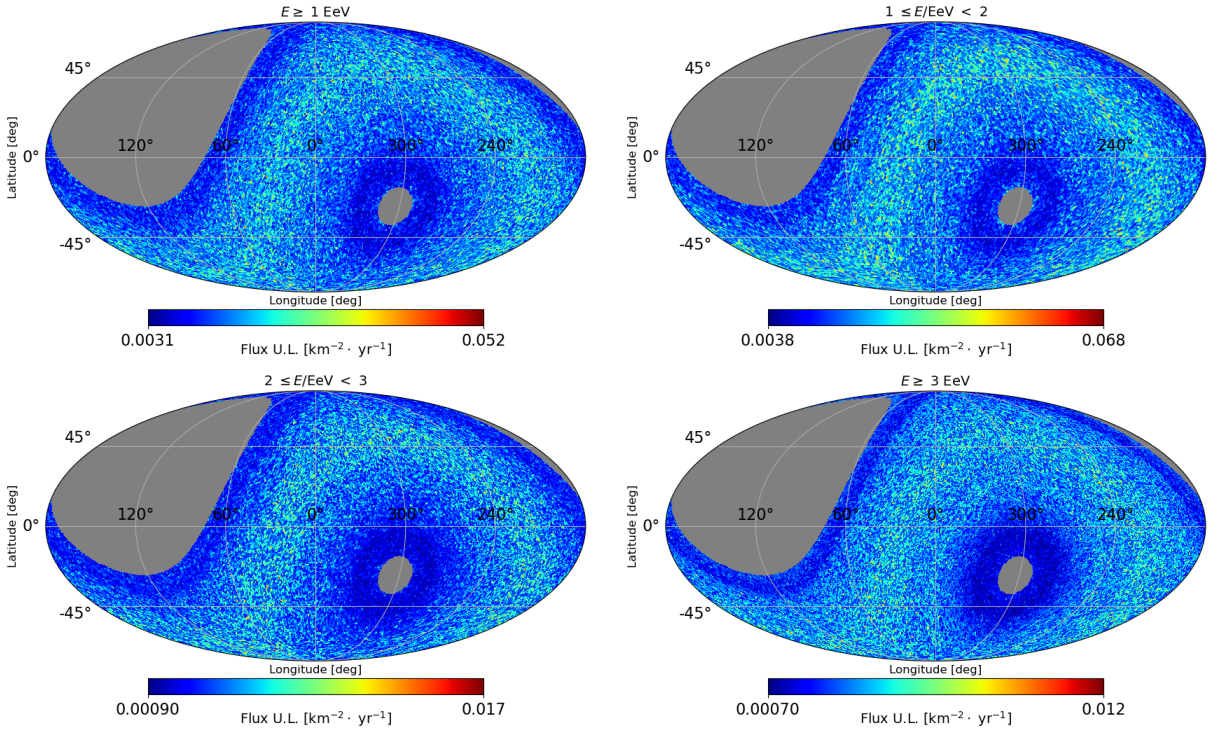

Figure 7.13: Upper limit on the flux of neutrons for each energy range for the inclined data set in Galactic coordinates.

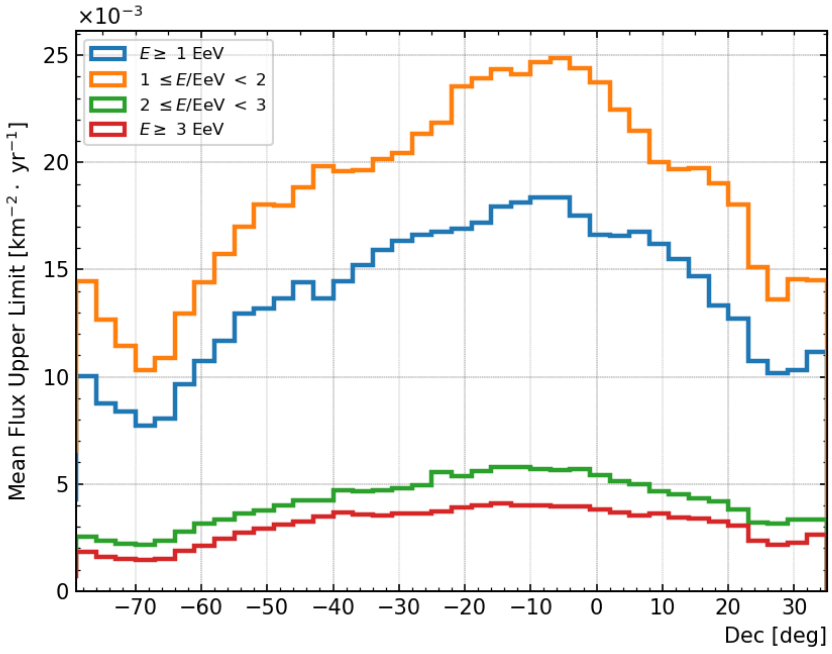

Figure 7.14: Mean flux upper limit as a function of the declination for the inclined data set. The mean is obtained by taking 3-degree intervals in declination.

7.4.3 Infill data set

The areas of the full and the infilled arrays are around 3,000 km^2 and 24 km^2, respectively. This size difference impacts the directional exposure, as we can observe in Figure 7.15 and compare it with Figure 7.5. The infill data set contains events with lower energies, resulting in a greater flux of cosmic rays than the other two data sets. Due to this, we have more statistics to work with when compared to the inclined data set presented in Subsection 7.4.2. Based on the directional exposure presented in Figure 7.15, we considered targets with declination between $-80°$ and $0°$ to estimate the Li-Ma significance. Figure 7.17 presents the mean expected number of events inside each target averaged in 3-degree intervals in declination. We present the results for the Li-Ma significance in Figure 7.16 and for the upper limit on the neutron flux in Figure 7.18.

Figure 7.16 presents the results for the Li-Ma significance for the infill data set for the four energy ranges considered here. Since the histograms follow a Gaussian distribution, as we would expect if the arrival direction distribution of the data set did not present local anisotropies, we do not have an indication of an excess that could point to a neutron flux. The integral curves demonstrate that the results for the observed data set are within the expected results obtained in 95% of the simulations.

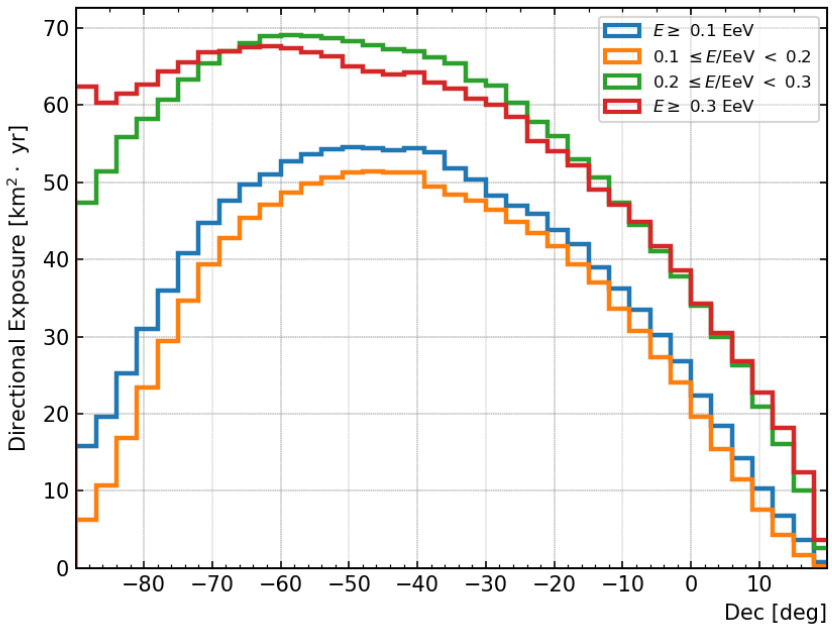

Figure 7.15: Mean directional exposure as a function of the declination for the infill data set. The mean is obtained by taking 3-degree intervals in declination.

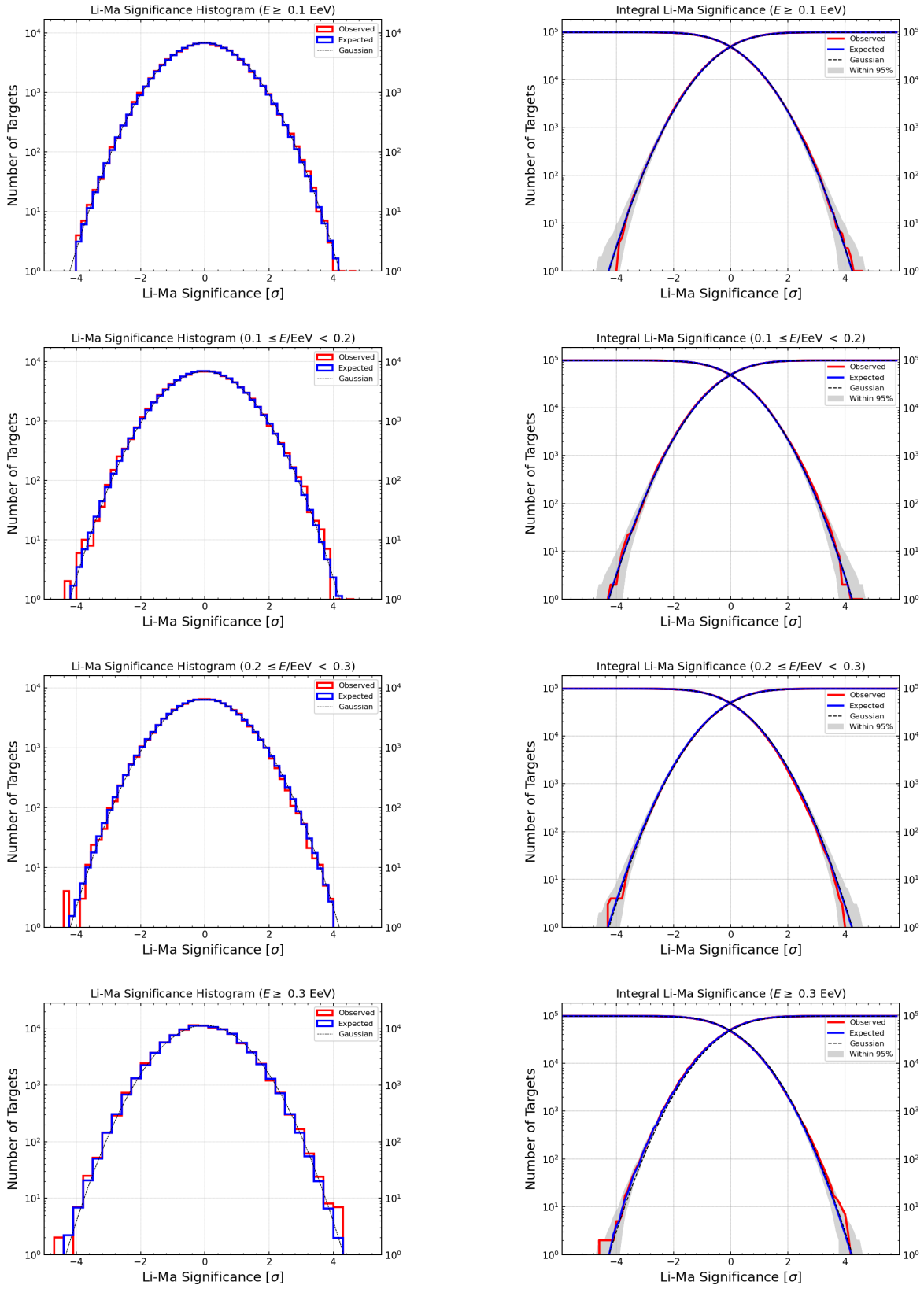

Figure 7.16: Li-Ma significance results for the infill data set.

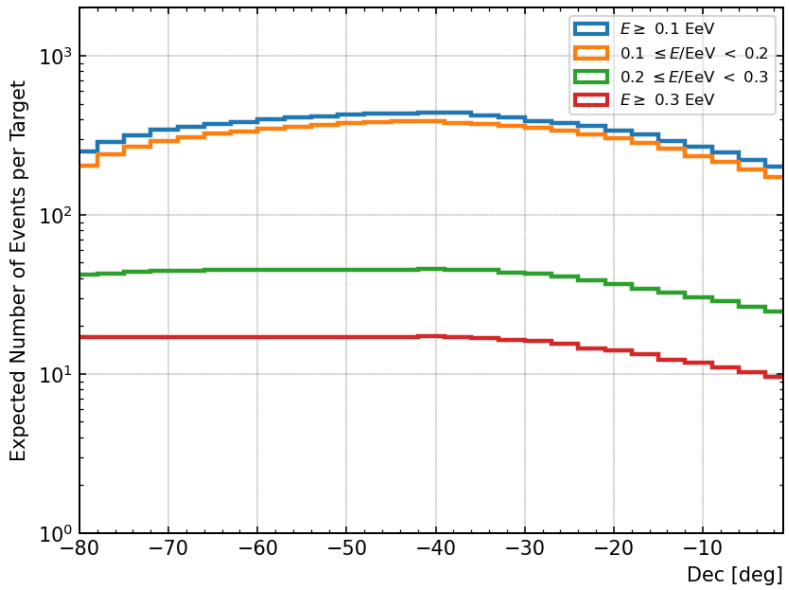

Figure 7.17: Expected number of events in each target region as a function of the declination for the infill data set. The mean is obtained by taking 3-degree intervals in declination.

We present the results for the upper limit on the neutron flux for the infill data set in Figures 7.18 and 7.19. The former are sky maps in Galactic coordinates for the upper limit flux, and the latter are the curves with the mean values obtained by using 3-degree intervals in declination.

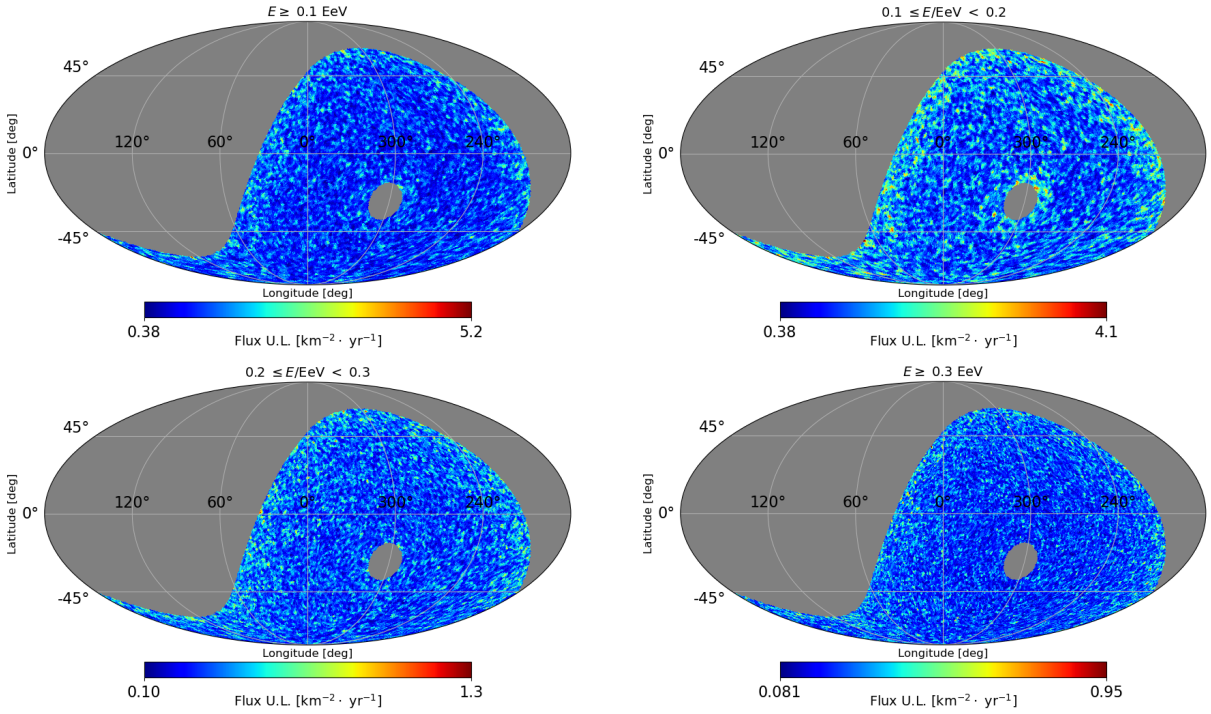

Figure 7.18: Upper limit on the flux of neutrons for each energy range for the infill data set in Galactic coordinates.

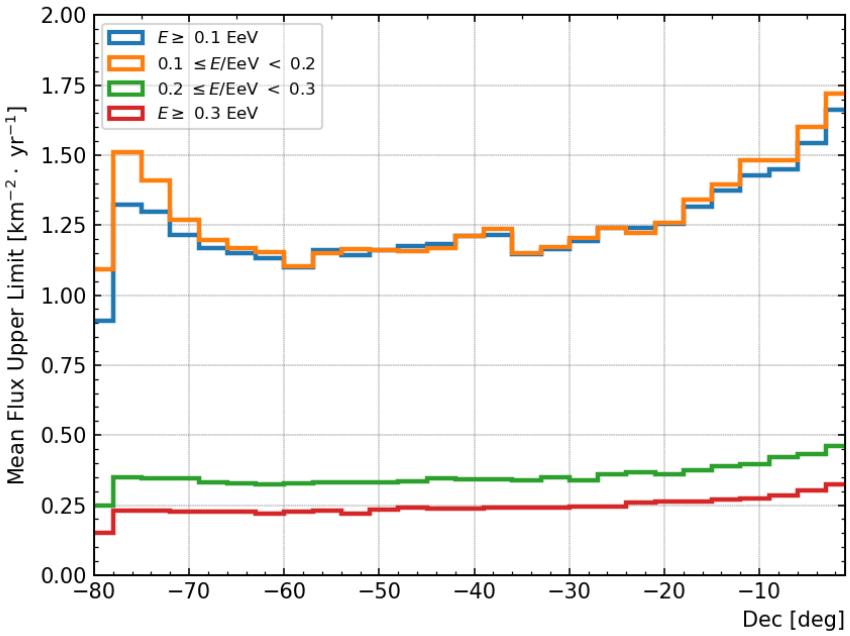

Figure 7.19: Mean flux upper limit as a function of the declination for the infill data set. The mean is obtained by taking 3-degree intervals in declination.

Considering all the tested data sets (the vertical, the inclined, and the infill), we do not identify clear evidence of excesses of events that could indicate a neutron flux. An interesting result we can obtain is the upper limit on the neutron flux. In Figures 7.8, 7.13, and 7.18, we present sky maps with the flux upper limits in Galactic coordinates. We also present the mean upper limit on the neutron flux as a function of the declination in Figures 7.9, 7.14, and 7.19.

After investigating neutron fluxes in the whole sky, respecting the field of view allowed for each data set, using the blind search, we can narrow down our analysis to specific directions of the sky where we have candidate sources. For this kind of search, referred to as targeted search, we present two methods in the next chapters.

8 TARGETED SEARCH FOR POINT SOURCES OF NEUTRONS IN WELL-DEFINED REGIONS

In this chapter, we discuss a method to investigate possible sources of cosmic rays in the energy range above 1 EeV for the full array, and above 0.1 EeV for the infilled array. The idea is to define a region in the sky around the candidate sources using a top-hat function, as in Chapter 6, and search for an excess of events that could indicate a neutron flux. Nonetheless, instead of looking at the whole sky, we will focus on specific directions where candidate sources of EeV particles lie. We will describe the candidate sources in the next section.

The method described in this chapter was published by the Pierre Auger Collaboration in 2014 [2]. In this thesis, we updated the catalogs and included new data sets with respect to the 2014 work. We present more details about the data sets and the candidate sources in Chapter 4. We present the updated results for the targeted search in Chapter 9.

8.1 The target sets

A first attempt to identify sources of ultra-high-energy particles is to search the whole sky and try to find significant event excesses. We discussed this method in Chapter 6. Another way to study possible sources is by selecting candidate sources of particles in the energy range of interest, narrowing the search. We consider astrophysical objects that can produce and accelerate particles at such high energies as candidate sources.

Supernovae are the result of the explosion of a star in which the inner layers form the supernova remnant. The supernova remnants are the most likely sources of ultra-high-energy cosmic rays. Neutron stars are a type of supernova remnant. Their intern balance is due to the *neutron degeneracy pressure*, so they are considered dead stars. The neutron degeneracy pressure is caused because neutrons are fermions. Therefore, they are subjected to the Pauli exclusion principle, which says that two or more fermions cannot occupy the same quantum state. Neutron stars are highly dense objects. In a neutron star, the density increases, resulting in a relativistic electron gas. When the total energy of the electron exceeds the mass difference between a neutron and a proton, the inverse β-decay occurs, $p + e^- \rightarrow n + \nu_e$. The number of neutrons starts to increase, forming a degenerate neutron gas. The degeneracy pressure of the neutron gas is what prevents the star from collapsing. The density of a neutron star can go from about $10^9\,\mathrm{kg\,m^{-3}}$ in the surface layers up to (possibly) $3 \times 10^{18}\,\mathrm{kg\,m^{-3}}$ in the core [74]. Pulsars are highly magnetized rotating neutron stars. The first identified pulsar was the source PSR B1919+21.

The High Energy Stereoscopic System (H.E.S.S.) experiment [136–138] is an array of telescopes, located in Namibia, designed to study γ-ray sources. The acronym refers to the physicist Victor Hess, the discoverer of cosmic rays. It is a collaboration of over 260 scientists from 13 countries. This observatory allows the study of cosmic γ-rays from dozens of GeV to dozens of TeV. In this energy range, particles can produce Cherenkov radiation in the atmosphere. Several of the γ-ray sources presented in this work were detected and identified by the H.E.S.S. experiment. The following section brings a short description of each one of them.

Millisecond pulsars: Pulsars are highly magnetized neutron stars [139] discovered in 1967 by Jocelyn Bell-Burnell and Antony Hewish [140] through signals recorded at the Mullard Radio Astronomy Observatory. Millisecond pulsars are rotating neutron stars with a short period, in the range of 1–10 ms. The first identified millisecond pulsar was the B1937+21 by Shrinivas Kulkarni, Donald Backer, and collaborators [141]. Since their discovery, over one hundred millisecond pulsars have been detected. The information from the millisecond pulsars used in this analysis was extracted from the Australia Telescope National Facility (ATNF) catalog [142]. A full description of the catalog was published by Manchester *et al* [143].

γ-ray pulsars: γ-ray pulsars have a strong confirmed emission of high-energy photons. The first observations of pulses in γ-ray emitted by neutron stars were made in the early 1970s [144]. The selected γ-ray pulsars used in this work were detected by the Fermi Gamma-ray Space Telescope in its first eight years of operation [145].

Low-mass X-ray binaries: Neutron stars can be part of binary systems. X-ray binaries were discovered using the UHURU satellite in the early 1970s [146]. In low-mass X-ray binaries, the companion of the neutron star is a low-mass star from the main sequence. This primary star is similar to the Sun, having mass, temperature, and luminosity compatible with the main star of our planetary system [74]. Information of the catalog used in this thesis was extracted from [147], and a description can be found at [148].

High-mass X-ray binaries: The primary star in high-mass X-ray binaries is a massive late 0 or early B type star [74]. The primary star is responsible for the optical light emission, and the compact object is responsible for the X-ray emission. The compact object can be a neutron star or a black hole. The catalog used in this work was extracted from the Catalog of High-Mass X-Ray Binaries in the Galaxy (HMXBCAT) [149] and a full description can be found at [150].

H.E.S.S. Pulsar Wind Nebulae: Nebulae are clouds composed of dust and gas that can be a region for star formation. In the case of Pulsar Wind Nebulae (PWNe), they are a type of nebula that resulted from the explosion of a massive star. PWNe are agglomerations

of ultra-relativistic particles with a central pulsar powering their winds. The PWNe catalog used in this work was detected and classified by the H.E.S.S. Collaboration.

Other H.E.S.S. identified sources: These sources were detected by the H.E.S.S. experiment, and they were classified into different types, such as supernova remnants and binary systems. However, there were too few of them to be considered individual classes, thus, in this work, we denominate them as the other H.E.S.S. identified sources.

H.E.S.S unidentified sources These are TeV emitters detected by the H.E.S.S. experiment that had not been identified as any known object, so their type is unidentified.

Microquasars: Quasars are AGN (Active Galactic Nuclei) with strong radio emissions. Their name is short for *quasi-stellar object* because they have a spectrum similar to a star emitting radio. Even though all galaxies present radio emission, the luminosity in quasars is much larger than in an ordinary galaxy, exceeding it by a factor of 100 or more. Microquasars are named after quasars since they have similar properties on different scales. These similarities were pointed out by Mirabel and Rodríguez in 1998 [151]. This class that mimics the phenomena observed in distant quasars are spinning black holes or neutron stars. The catalog used here can be found at [152].

Magnetars: Magnetars are a class of extreme pulsars comprehending the pulsars known as soft γ-ray repeaters and anomalous X-ray pulsars. The concept was proposed in 1992 when Duncan and Thompson suggested the existence of neutron stars with strong magnetic fields of the order of 10^{14} to 10^{15} G [153]. In magnetars, the main source of energy is provided by the strong magnetic field [154].

Galactic Center: The Galactic Center is an interesting region to look at due to the high activity caused by its central black hole. The central black hole is called Sagittarius A* and it has around 4×10^6 $M_\odot$. The Galactic Center is around 8.3 kpc from Earth [155].

In Figure 8.1, we show the angular distribution of the candidate sources in equatorial coordinates. The region where we can see an accumulation of sources is a part of the Galactic plane. As a comparison, the 2014 work [2] tested 358 targets. In this thesis, we increased this number to 670[1].

8.2 Estimating the significance of a target

We define the target size following the same procedure described in Section 6.1. The target size is given by Equation 6.8, $\chi = 1.05\psi$, with ψ representing the angular resolution. Therefore, the target size depends on the energy and the declination. The observed number of

[1] Since each data set allows a different field of view, the total number of targets used depends on the chosen data set.

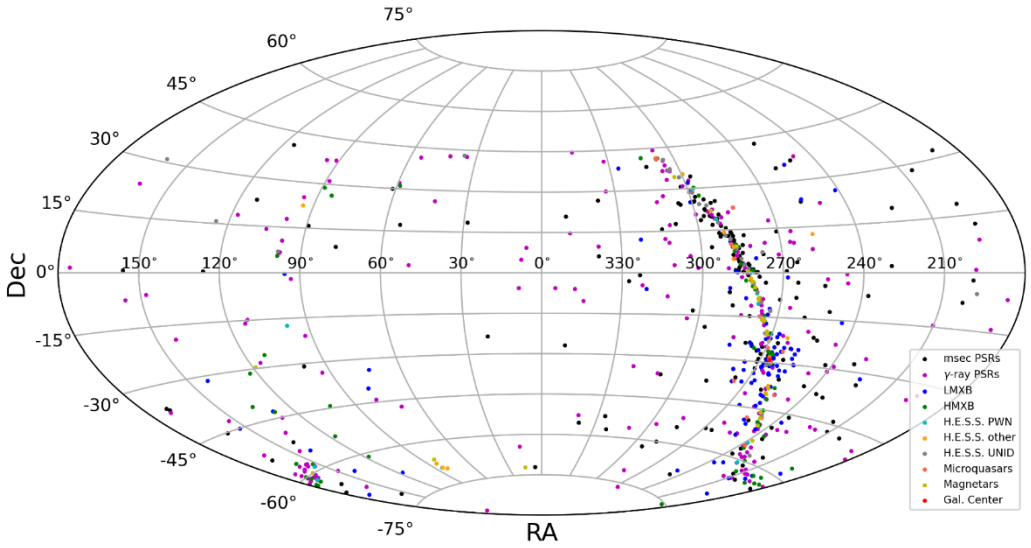

Figure 8.1: Sky map with the angular distribution of the candidate sources used in this analysis in equatorial coordinates. The candidate sources are split into classes.

events from a given target, n, is the count of arrival directions inside the solid angle with an opening angle χ. The expected number of events, b, is obtained by averaging the results obtained using 10,000 simulated data sets in the same angular region. Each simulated data set is produced with the method described in Section 6.3, using the scrambling technique.

We can estimate the significance of each candidate source based on the observed and expected number of events, n, and b, respectively. We defined the p-value as

$$p = \frac{1}{2}[\text{Poisson}(n, b) + \text{Poisson}(n+1, b)], \tag{8.1}$$

where Poisson(n, b) represents the probability of getting n or more events in the presence of a background following a Poisson distribution with mean b. We take the average between the probability using n and $n+1$ to avoid the bias caused by background fluctuations. Considering M candidate sources in a target set, the penalized p-value represents the probability of getting a p-value less or equal to p, if all the M p-values were sampled from a uniform distribution between 0 and 1. The penalized p-value takes into account that, for each target set, we are testing various targets. The penalized p-value is given by

$$p^* = 1 - (1-p)^M. \tag{8.2}$$

We identify a significant target considering the post-trial p-value (the penalized p-value). A penalized p-value with a $3\,\sigma$ significance level should be equal to or less than 1.4×10^{-3}. Typically, a p-value with a $3\,\sigma$ significance is $p = 2.7 \times 10^{-3}$. However, in our scenario, negative p-values are not possible. Therefore, to account for this constraint that we can only obtain positive values, we divide the p-value threshold by a factor of 2.

8.3 The special case of the Galactic plane

In the special case of the Galactic plane (Galactic latitude of 0°), we can consider it as a target set with a single target. We present the details related to the Galactic coordinate system in Appendix A. Assuming that the sources present in the Galactic plane are emitting a density signal proportional to a Gaussian distribution, we can estimate the total signal, coming from the Galactic plane in a slice of thickness 2β, through the following relation:

$$S \propto \int_{-\beta}^{+\beta} d\overline{\beta} \exp\left(-\frac{\overline{\beta}^2}{2\sigma^2}\right) = \sqrt{2\pi}\sigma \,\mathrm{erf}\left(\frac{\beta}{\sqrt{2}\sigma}\right), \tag{8.3}$$

where β is the Galactic latitude[2]. We use $\overline{\beta}$ to distinguish between the variable of integration and the limits of integration. Our goal is to find the β value that maximizes the signal-to-noise ratio. In a region defined by the half thickness β, the number of events collected is proportional to β. So, the noise is roughly proportional to $\sqrt{\beta}$. Maximizing the signal-to-noise ratio, we obtain:

$$\frac{d}{d\beta}\left[\sqrt{\frac{2\pi}{\beta}}\sigma \,\mathrm{erf}\left(\frac{\beta}{\sqrt{2}\sigma}\right)\right] = 0 \implies \frac{\beta}{\sigma}\exp\left(-\frac{\beta^2}{2\sigma^2}\right) = \sqrt{\frac{\pi}{8}}\,\mathrm{erf}\left(\frac{\beta}{\sqrt{2}\sigma}\right). \tag{8.4}$$

We can solve Equation 8.4 numerically to obtain the relation $\beta = 1.40\sigma$. Using the relation between σ and the angular resolution (Equation 6.8), we define the half thickness as $\beta = 0.93\Psi$, where Ψ is the mean angular resolution in the portion of the Galactic plane exposed to the Observatory. Thus, for this specific target region, the observed number of events is the number of events with a Galactic latitude less than 0.93Ψ. The expected number of events is obtained using the same criterion for the 10,000 simulated data sets using the scrambling method.

8.4 Upper limit on the neutron flux and the energy flux

The upper limit on the number of neutrons can be estimated from the observed number of events n and the background expectation b, using the same procedure described in Section 6.5. Then the upper limit on the flux is obtained by scaling the upper limit on the number of neutrons by the factor 1.39 and dividing by the directional exposure. For the special case of the Galactic plane, the solid angle of this target region is $2\pi \times 2\beta$ sr, with β measured in radians.

After estimating the upper limit on the neutron flux, it is interesting to estimate an upper limit on the energy flux. We assume an E^{-2} differential energy spectrum. In this

[2]Usually, the Galactic latitude is denoted by the letter b. However, to avoid confusion with the expected number of events in a target region, we denote the Galactic latitude by the Greek letter β.

scenario, the integral flux is proportional to E^{-1}. Integrating this in a decade of energy, we obtain an energy flux proportional to $\ln 10$. Therefore, the upper limit on the energy flux is the upper limit on the neutron flux scaled by a factor of $\ln 10$.

8.5 Analysis combining targets

In addition to investigating the individual targets, we can consider each target set as a candidate neutron emitter. If a specific class of astrophysical objects is responsible for emitting neutrons, this class would be more significant as a set than its individual sources.

Let us consider a target set with M candidate sources and the product of the p-values associated with each target,

$$\Pi_0 = \prod_{i=1}^{M} p_i. \tag{8.5}$$

The probability that a set of M p-values randomly sampled from a uniform distribution between 0 and 1 gives a product less or equal to Π_0 is given by:

$$P(\Pi \leq \Pi_0) = \Pi_0 \sum_{j=0}^{M-1} \frac{(-\ln \Pi_0)^j}{j!} = 1 - \text{Poisson}(M, -\ln \Pi_0). \tag{8.6}$$

We present the details of the mathematical deduction of Equation 8.6 in the Appendix B.2.

We can add statistical weights when combining the p-values to take into account the attenuation factor due to neutron decay (considering the traveled distance by the neutron), the exposure of the target to the Observatory, and the electromagnetic flux at the candidate source (recorded in the catalog). The statistical weights are proportional to these three factors[3], and normalized in a way that the sum of all the weights in a target set is equal to 1. The weighted product Π_0^w is obtained by raising each p-value by its correspondent statistical weight:

$$\Pi_0^w = \prod_{i=1}^{M} p_i^{w_i}. \tag{8.7}$$

The weighted combined P-value is given by the Good's formula [156]. Due to the computational difficulties of using this formula, we obtain the weighted combined P-value using simulated sets of p-values. If a target set has M targets, we sample sets of M uniformly distributed values between 0 and 1. We raise each one of these values by the correspondent statistical weight and obtain the weighted product Π^w. Then, the weighted combined P-value is the number of simulated sets of p-values resulting in a product Π^w less than Π_0^w.

As in the blind search, presented in Chapter 6, we perform the targeted search in

[3]For some targets, we do not have information about the distance or the electromagnetic flux. For these cases, we evaluate the statistical weight with the available pieces of information.

three data sets: the vertical, the inclined, and the infill ones. In the next chapter, we present the results of the targeted search in well-defined regions.

9 RESULTS FOR THE TARGETED SEARCH: WELL-DEFINED TARGET REGIONS

In this chapter, we present the results for the targeted search for point sources of neutrons using the method explained in Chapter 8. In this method, we define a target region where we search for event excesses, comparing the observed number of events within the region with the expected number. The target size is 1.05 times the angular resolution at the position of the target. The fit parameters for the angular resolution are presented in 7.3. The expected number is obtained using a scrambling technique to erase local excesses, providing an estimation of the background signal when enough simulated data sets are used. We simulated 10,000 data sets to estimate the expected number of events in each target region. For this method, we restrict the tested directions, narrowing down to specific directions where candidate sources lie. We described the candidate sources considered for the results presented below in Section 8.1.

We investigate neutron fluxes using three different data sets: the vertical (events with a zenith angle less than 60°), the inclined (events with a zenith angle between 60° and 80°), and the infill (events recorded by the infilled portion of the array). The results for these three data sets are presented below.

9.1 Vertical data set

In Table 9.1, we present the results for the most significant target in each target set for the vertical data set using the cumulative data set ($E \geq 1$ EeV). The most significant target is the one with the smallest individual p-value. The tables show the position of the candidate source, the observed and expected number of events inside the target region, and the upper limit on the flux of neutrons and on the energy flux, in addition to the p-value and the penalized p-value. The penalized p-value takes into account that in each target set, we are testing multiple targets. It represents the chance probability of getting a p-value equal to or less than p if all the p-values in a target set were sampled from a uniform distribution between 0 and 1.

The smallest individual penalized p-value for the cumulative data set using vertical events is associated with a low-mass X-ray binary (LMXB) system located at the position $(117.14°, -67.75°)$. For this data set, we tested 95 LMXB targets. The penalized p-value for this target was 0.33, associated with a p-value $p = 0.0042$. Therefore, we have a 33% chance of getting a p-value equal to or less than 0.0042 when sampling 95 p-values from a uniform distribution between 0 and 1. For this target, the upper limit on the neutron flux is $0.012\,\mathrm{km^{-2}\,yr^{-1}}$, resulting in an energy flux of $0.087\,\mathrm{eV\,cm^{-2}\,s^{-1}}$, assuming an E^{-2} spec-

trum. Considering the penalized p-values presented in Table 9.1, we do not find any clear evidence of a neutron flux coming from the direction of any of the tested targets. Investigating the other energy ranges used in this work, we also do not identify evidence of neutron flux. Since the tested targets are not significant, we present the results for the cumulative data set in Table 9.1, and for the other energy ranges, in Appendix C, in Tables C.1, C.2, and C.3.

The vertical data set was studied before, with data detected at the Observatory from 2004 to 2013. These results were published in [2]. The new data set brings an update of almost ten years since it was detected from 2004 to 2022. Using almost three times more exposure, the results presented in Table 9.1 can be compared with the ones published in 2014. In [2], the smallest individual penalized p-value was 0.10. This target also belongs to the LMXB class, however, in a different position than the one found in our work and presented in Table 9.1. This target with the smallest individual p-value in [2] is located at $(264.57°, -26.99°)$ with a individual p-value of 0.0012. In the work published in 2014, 87 targets in the LMXB target set were tested. In that paper, as in this thesis, no clear evidence of an excess of events that could indicate a neutron flux was found. For the Galactic center, the 2014 work obtained a p-value $p = 0.24$ for the data set with events above 1 EeV. In our case, we obtained for this target a p-value equal to 0.96

We also investigate the possibility of a neutron flux coming from the Galactic plane. In this case, we compare the observed number of events in a slice around the Galactic plane with the expected value obtained from simulations. The size of this slice depends on a parameter called the half thickness, measured from the Galactic plane. The total size of the target region is twice the half thickness. In Table 9.2, we present the half thickness, the observed and expected number of events in the target region, the upper limit on the neutron flux and on the neutron energy flux, and the p-value for each one of the energy ranges in which we split the vertical events. The smallest p-value was 0.20 for events with an energy between 2 EeV and 3 EeV. Therefore, none of the tested energy ranges is significant, and we do not identify evidence of a neutron flux coming from the Galactic plane. In [2], the half thickness using the cumulative data set was 1.17°, resulting in 16,965 observed events and 17,197 expected events, leading to a p-value of 0.96. For the same energy range, in this work, we obtained a half thickness of 1.11°, resulting in 49,176 observed events and 49,164 expected events, leading to a p-value of 0.48.

Table 9.1: Results for the most significant target in each target set for the vertical data set and events with energy above 1 EeV.

Results for the targeted search - vertical data set - $E \geq 1$ EeV								
Class	**RA [deg]**	**Dec [deg]**	**Observed**	**Expected**	**Flux U.L.** $[\mathrm{km^{-2}\ yr^{-1}}]$	**E-flux U.L.** $[\mathrm{eV\ cm^{-2}\ s^{-1}}]$	p**-value**	p**-value (penalized)**
msec PSRs	218.83	−61.02	705	646	0.012	0.085	0.011	0.79
γ-ray PSRs	271.43	6.26	238	203	0.016	0.12	0.0082	0.75
LMXB	117.14	−67.75	634	570	0.012	0.087	0.0042	0.33
HMXB	195.32	−61.60	700	640	0.012	0.086	0.0096	0.39
H.E.S.S. PWN	154.50	−58.92	696	667	0.0084	0.062	0.13	0.79
H.E.S.S. other	282.12	−1.79	356	324	0.013	0.094	0.039	0.45
H.E.S.S. UNID	284.40	2.97	268	251	0.011	0.077	0.14	0.99
Microquasars	287.96	4.98	248	222	0.013	0.096	0.042	0.43
Magnetars	15.18	−72.19	556	515	0.0091	0.066	0.037	0.61
Gal. Center	266.42	−29.01	642	688	0.0040	0.029	0.96	0.96

Table 9.2: Results for the Galactic plane for the vertical data set.

Results for the Galactic plane - Vertical data set						
Energy range	**Half thick. [deg]**	**Observed**	**Expected**	**Flux U.L. [km^{-2} yr^{-1}]**	**E-flux U.L. [eV cm^{-2} s^{-1}]**	**p-value**
$E \geq 1$ EeV	1.11	49176	49164	0.087	0.64	0.48
$1 \leq E/\text{EeV} \leq 2$	1.23	41616	41767	0.063	0.46	0.77
$2 \leq E/\text{EeV} \leq 3$	0.87	5304	5243	0.034	0.24	0.20
$E \geq 3$ EeV	0.59	2343	2420	0.011	0.083	0.94

We can also test the possibility that one of the classes of candidate sources is emitting neutrons. If one of the classes is responsible for emitting neutrons, the combined P-value will be more significant than the individual p-values. We can calculate the combined P-value without including statistical weights with Equation 8.6 and including statistical weights. The statistical weight takes into account the electromagnetic flux at the candidate source, the exposure of the Observatory at the location of the target, and the attenuation factor caused by the neutron decay. We can only obtain this attenuation factor for candidate sources with a known distance. For those targets with an unknown distance, we evaluate the weight using the other two pieces of information. The weighted combined P-value is obtained using simulations, as explained in Section 8.5.

In Table 9.3, we present the results for the combined P-values both without (unweighted) and including (weighted) statistical weights for the cumulative data set. The smallest unweighted combined P-value is 0.24 and is associated with the LMXB target set. For this class, the weighted P-value is 0.20. Therefore, both the unweighted and the weighted P-values for this target set are not significant. The smallest weighted P-value is associated with the class of the γ-ray pulsars ($P_w = 0.053$), which is also not significant. The results for unweighted and weighted P-values in the other energy ranges are presented in the Appendix C in Tables C.4, C.5, and C.6. We did not find evidence that any of the tested classes are significant, reinforcing the results published by the Auger Collaboration in [2].

Table 9.3: Results for the combined analysis for the vertical data set with events above 1 EeV.

Results for combined analysis - Vertical data set - $E \geq 1$ EeV			
Class	**Number of targets**	**P-value (unweighted)**	**P-value (weighted)**
msec PSRs	142	0.67	0.67
γ-ray PSRs	168	0.87	0.053
LMXB	95	0.24	0.20
HMXB	52	0.82	0.82
H.E.S.S. PWN	11	0.89	0.70
H.E.S.S. other	15	0.47	0.72
H.E.S.S. UNID	28	0.99	0.99
Microquasars	13	0.34	0.51
Magnetars	25	0.88	0.98
Gal. Center	1	0.96	0.96

9.2 Inclined data set

We perform the same analysis described above, in which we use the vertical data set, for the inclined data set. This data set contains events with a zenith angle between 60° and 80°. In Table 9.4, we present the results for the analysis using the cumulative inclined data set ($E \geq 1$ EeV). In this table, we show the target with the smallest individual p-value in each target set, reporting its angular position, the observed and expected number of events in the target region, the flux and energy flux upper limit, the p-value and the penalized p-value. The smallest individual p-value is 0.00031 and it is associated with a γ-pulsar located at $(212.60°, -61.54°)$. For this target, the penalized p-value is 0.056, indicating a 5.6% chance of sampling a p-value equal to or less than 0.00031 when sampling 188[1] p-values uniformly distributed between 0 and 1. The smallest individual penalized p-value is 0.020, associated with a high-mass X-ray binary system located at $(195.49°, -63.97°)$, which is also not significant. We do not find any clear evidence of an excess coming from the direction of any of the tested targets in any of the energy ranges. We report the results for the other energy ranges in Appendix C in Tables C.7, C.8, and C.9.

For the special case of the Galactic plane, we present the results obtained using the procedure described in Section 8.3. Using the inclined data set, we report for each energy range the observed number of events in the region defined by the half thickness in Table 9.5. The half thickness is measured from the Galactic plane and depends on the average angular

[1]Total number of targets in this target set. The number of targets in each target set is presented in Table 9.6.

Table 9.4: Results for the most significant target in each target set for the inclined data set and events with energy above 1 EeV.

Results for the targeted search - inclined data set - $E \geq 1$ EeV								
Class	**RA [deg]**	**Dec [deg]**	**Observed**	**Expected**	**Flux U.L.** $[\mathrm{km^{-2}\ yr^{-1}}]$	**E-flux U.L.** $[\mathrm{eV\ cm^{-2}\ s^{-1}}]$	p**-value**	p**-value (penalized)**
msec PSRs	155.95	0.64	16	6	0.045	0.33	0.00034	0.058
γ-ray PSRs	212.60	−61.54	30	15	0.025	0.18	0.00031	0.056
LMXB	201.11	−63.22	25	16	0.017	0.12	0.018	0.83
HMXB	195.49	−63.97	34	18	0.022	0.16	0.00037	0.020
H.E.S.S. PWN	279.41	−6.95	9	7	0.021	0.15	0.22	0.96
H.E.S.S. other	287.78	9.09	10	7	0.022	0.16	0.13	0.90
H.E.S.S. UNID	290.30	13.13	13	7	0.028	0.20	0.020	0.48
Microquasars	262.75	−26.00	11	6	0.030	0.22	0.031	0.36
Magnetars	283.19	0.55	10	6	0.028	0.21	0.063	0.82
Gal. Center	266.42	−29.01	7	7	0.016	0.11	0.48	0.48

resolution along this plane. Using the fit presented in Figure 7.3, we obtain the average angular resolution. Then, the half thickness is this mean value times 0.93[2]. As we can observe in Table 9.5, the p-values for the Galactic plane vary between 0.65 and 0.79, indicating that we do not have evidence of a neutron flux coming from the Galactic plane with inclined events in any of the tested energy ranges. Even though the Galactic plane region is not significant, we can obtain an upper limit on the neutron flux and on the energy flux. These results are also reported in Table 9.5.

Table 9.5: Results for the Galactic plane for the inclined data set.

Results for the Galactic plane - Inclined data set						
Energy range	**Half thick. [deg]**	**Observed**	**Expected**	**Flux U.L.** $[\mathrm{km^{-2}\ yr^{-1}}]$	**E-flux U.L.** $[\mathrm{eV\ cm^{-2}\ s^{-1}}]$	p**-value**
$E \geq 1$ EeV	0.46	2665	2707	0.14	1.0	0.79
$1 \leq E/\mathrm{EeV} \leq 2$	0.54	1587	1616	0.17	1.2	0.76
$2 \leq E/\mathrm{EeV} \leq 3$	0.44	637	657	0.033	0.24	0.78
$E \geq 3$ EeV	0.33	429	437	0.026	0.19	0.65

We also investigate the possibility of one specific class emitting neutrons by combining the p-values. In Table 9.6, we present the results for the combined analysis using the cumulative inclined data set. In this table, we report the total number of tested targets in each class, the unweighted combined P-value, and the weighted combined P-value. The procedure of how we can combine the individual p-values is presented in Section 8.5. The weighted combined P-value considers the electromagnetic flux at the target, its exposure to the Observatory, and the expected attenuation factor due to the neutron decay considering the traveled distance. The smallest combined P-value, both for the unweighted and the weighted cases, is associated with the target set of the unidentified sources detected by the H.E.S.S. experiment (H.E.S.S. UNID). For this class, the unweighted combined P-value is 0.021 and we get a combined P-value of 0.034 after including the statistical weights. Therefore, this class, as all the other tested ones, is not significant, indicating that we do not have any indication that any of the tested target sets is responsible for emitting a neutron flux. The conclusion is the same for all the energy ranges used in this analysis. We report the results for the other energy ranges in Tables C.10, C.11, and C.12.

[2]We describe in Section 8.3 the details of how this factor is obtained.

Table 9.6: Results for the combined analysis for the inclined data set with events above 1 EeV.

Results for combined analysis - Inclined data set - $E \geq 1$ EeV			
Class	**Number of targets**	**P-value (unweighted)**	**P-value (weighted)**
msec PSRs	175	0.33	0.85
γ-ray PSRs	188	0.57	0.49
LMXB	99	0.85	0.89
HMXB	55	0.57	0.20
H.E.S.S. PWN	13	0.98	0.45
H.E.S.S. other	16	0.95	0.71
H.E.S.S. UNID	33	0.021	0.034
Microquasars	14	0.48	0.75
Magnetars	26	0.90	0.82
Gal. Center	1	0.48	0.48

9.3 Infill data set

Regarding the method described in Chapter 8, we also investigate hints of neutron fluxes using events recorded by the infilled portion of the Observatory. This data set is described in Chapter 4. As in the other data sets, we split the events into four energy ranges. In Table 9.7, we present the results for the cumulative data set ($E \geq 0.1$ EeV). The penalized p-values indicate that none of the tested targets is significant. For this data set, considering the energy range above 0.1 EeV, the smallest individual p-value is 0.0033 associated with a γ-ray pulsar located at $(274.29°, -17.70°)$. For the γ-ray pulsar class, we tested 136 targets, resulting in a penalized p-value of 0.36 for this target. The smallest individual penalized p-value is 0.096, associated with one of the 16 unidentified H.E.S.S. sources. This candidate source is located at $(273.34°, -12.69°)$, and its p-value before the penalization was 0.0063.

For this data set, the events have a lower energy, implying in a shorter expected traveled distance due to neutron decay. Therefore, we would expect that, if we had detected a neutron flux, this flux would come from the closest candidate sources, given that neutrons would probably decay before reaching Earth if they were produced by the farthest sources. However, we do not identify a neutron flux from any of the tested targets. The same is true for the other energy ranges, reported in Tables C.13, C.14, and C.15.

For the Galactic plane, we present the results for all the energy ranges in Table 9.8. For the cumulative data set, the half thickness is 0.93°, resulting in 37,919 observed events. The expected number of events within this region, considering this energy range, is 37,796. We obtain the expected number the events using simulated data sets, as explained

Table 9.7: Results for the most significant target in each target set for the infill data set and events with energy above 0.1 EeV.

Results for the targeted search - infill data set - $E \geq 0.1$ EeV								
Class	**RA [deg]**	**Dec [deg]**	**Observed**	**Expected**	**Flux U.L.** $[\mathrm{km^{-2}\ yr^{-1}}]$	**E-flux U.L.** $[\mathrm{eV\ cm^{-2}\ s^{-1}}]$	p**-value**	p**-value (penalized)**
msec PSRs	232.31	−38.48	475	435	2.0	15.0	0.029	0.93
γ-ray PSRs	274.29	−17.70	375	325	2.7	20.0	0.0033	0.36
LMXB	274.43	−33.02	465	421	2.2	16.0	0.017	0.79
HMXB	116.85	−53.33	448	416	1.8	13.0	0.060	0.94
H.E.S.S. PWN	169.75	−61.40	416	386	1.8	13.0	0.065	0.52
H.E.S.S. other	282.12	−1.79	217	200	2.3	17.0	0.12	0.74
H.E.S.S. UNID	273.34	−12.69	328	285	2.7	20.0	0.0063	0.096
Microquasars	275.50	−37.02	468	432	1.9	14.0	0.043	0.38
Magnetars	275.57	−16.07	334	312	1.9	14.0	0.11	0.93
Gal. Center	266.42	−29.01	415	402	1.5	11.0	0.26	0.26

in Chapter 8. The p-values are between 0.26 ($E \geq 0.1$ EeV) and 0.81 (0.2 EeV $\leq E <$ 0.3 EeV), indicating that we do not have an indication of a neutron flux coming from the Galactic plane region.

Table 9.8: Results for the Galactic plane for the infill data set.

Results for the Galactic plane - Infill data set						
Energy range	**Half thick. [deg]**	**Observed**	**Expected**	**Flux U.L. [km^{-2} yr^{-1}]**	**E-flux U.L. [eV cm^{-2} s^{-1}]**	**p-value**
$E \geq 0.1$ EeV	0.93	37919	37796	22	160	0.26
0.1 – 0.2 EeV	1.04	30948	30949	18	130	0.50
0.2 – 0.3 EeV	0.79	5091	5153	3.9	28	0.81
$E \geq 0.3$ EeV	0.60	2489	2524	2.9	21	0.76

We also combined all the targets to obtain the probability of one of the tested target sets emitting neutrons using the method described in Section 8.5. The results for the cumulative data set are presented in Table 9.9. The smallest unweighted combined P-value is 0.12, associated with the microquasars. This class is also the one with the smallest weighted combined P-value (0.074). As in the vertical and the inclined data sets, we do not find any compelling evidence that one of the target sets is producing neutrons. We get the same conclusion for the other energy ranges. The results for the other three energy ranges are presented in Tables C.16, C.17, and C.18.

Table 9.9: Results for the combined analysis for the infill data set with events above 0.1 EeV.

Results for combined analysis - Infill data set - $E \geq 0.1$ EeV			
Class	**Number of targets**	**P-value (unweighted)**	**P-value (weighted)**
msec PSRs	90	0.20	0.78
γ-ray PSRs	136	0.89	0.92
LMXB	89	0.87	0.68
HMXB	45	0.29	0.94
H.E.S.S. PWN	11	0.26	0.12
H.E.S.S. other	11	0.50	0.86
H.E.S.S. UNID	16	0.23	0.38
Microquasars	11	0.12	0.074
Magnetars	23	0.85	0.55
Gal. Center	1	0.26	0.26

Considering all the investigated data sets (vertical, inclined, and infill) and all the used energy ranges (four for each data set), we do not find any evidence of a neutron flux coming from any of the tested targets. We would identify a significant target by the individual penalized p-value. A penalized p-value with a $3\,\sigma$ significance would be equal to (or less than) 1.4×10^{-3}. We also investigate if one of the classes of astrophysical objects would be more significant as a set than its individual targets. We conclude, after estimating the combined P-values, that none of the tested target sets are significant.

The negative detection of a neutron flux reinforces the results obtained by the Auger Collaboration in a targeted neutron search published in 2014 [2]. In this thesis, we updated the results of this paper including more than nine extra years of observation. We also studied two new data sets: the one with inclined events ($60° < \theta < 80°$) and the one with events recorded by the infilled portion of the SD array.

10 SEARCH FOR POINT SOURCES OF NEUTRONS: PROBABILITY DENSITY METHOD

The methods described in Chapters 6 and 8 use a top-hat function to determine the number of events in a specific region of the sky. Even though this is a good approach, by making a hard cut in the definition of the region, we may not consider some events coming from the direction of the target due to their uncertainties on the measured arrival directions. An alternative method is assigning a weight to each event representing the probability density that this event came from the position of the target. As in the method described in Chapter 8, the method discussed in this chapter is a targeted search. We use the same target sets presented in Section 8.1.

We can estimate the air shower density at the position of a candidate source through the probability density of each event in the data set coming from its direction. We define a weight that represents this probability density. Then we calculate the air shower density by summing the weights associated with each event in the data set. Since we cannot distinguish between air showers initiated by protons and neutrons, we search for evidence of neutron fluxes by comparing the observed density with the one expected from the background. Since it is interesting to estimate the upper limit on the neutron flux based on the observed and expected air shower densities, we present an alternative method to estimate this upper limit to the one presented in Section 6.5. The first step of this analysis is to define the weight. We describe the details about how to calculate the weights in the next section.

10.1 Definition of the probability density

The probability density of an event being associated with a target depends on the angular distance between them, as well as the uncertainty in the measured arrival direction. Using data detected at the Observatory, it is possible to estimate the angular direction of the events in local coordinates. Therefore, we have uncertainties on the measured local angles, $\Delta\theta$ and $\Delta\varphi$[1], associated with the zenith and the azimuth angles, respectively. From these uncertainties, we can estimate a combined angular uncertainty,

$$\sigma = \sqrt{(\Delta\theta)^2 + (\sin\theta\Delta\varphi)^2}. \tag{10.1}$$

Then, we can assign to each event a weight that represents a probability that this event is

[1]The local coordinate system is presented in Appendix A.

coming from the direction of the candidate source as

$$w_i = \frac{1}{2\pi\sigma_i^2} \exp\left(-\frac{\xi_i^2}{2\sigma_i^2}\right), \tag{10.2}$$

where ξ_i is the angular distance between the i-th event and the target (the larger the angular distance, the smaller the weight). This weight is a symmetrical two-dimensional Gaussian distribution.

10.2 Evaluation of the significance of a target

When summing the weights over all the N events in a data set, we obtain the observed density of air showers for each target. Consequently, the air shower density, denoted as ρ_{obs}, can be expressed as

$$\rho_{\text{obs}} = \sum_i^N w_i. \tag{10.3}$$

To detect an excess of events coming from the direction of the target, we can calculate a p-value associated with this target. For this, we need to estimate the background signal. We use a procedure similar to the one described in Section 6.3 to erase local anisotropies. For the method discussed in this chapter, we still sample two events from the observed data set to simulate an angular direction using the scrambling technique [133]. From one of them, we extract information about the detection time, and from the other, we extract information about the zenith angle and the uncertainties in local coordinates. We also sample an azimuth angle from a uniform distribution between 0 and 2π. When extracting the information about the local angular uncertainties from the same event from which we acquired the zenith angle information, we ensure that we are sampling a σ value (Equation 10.1) from the observed distribution.

Each simulated data set contains the same number of events as the observed. From each scrambled data set, we obtain a simulated density of events at the position of the target, ρ_{scr}, given by

$$\rho_{\text{scr}} = \sum_i^N w_i^{\text{scr}}, \tag{10.4}$$

where w_i^{scr} indicates the weight of the i-th simulated event in the scrambled data set. Then, we estimate the p-value by evaluating the fraction of simulations in which the scrambled data set produces a ρ_{scr} larger than the observed value ρ_{obs}. To estimate this fraction, we generate 10,000 simulated data sets.

10.3 The special case of the Galactic plane

In the method described in Chapter 8, we investigate the Galactic plane as a single-element target set. We can do the same with the probability density method. However, we need to modify the definition of the weight. The other targets are point directions, while the Galactic plane is a region. So, instead of using a two-dimensional Gaussian distribution, we should use a one-dimensional Gaussian distribution. Thus, we define the weight as

$$w_i = \frac{1}{\sqrt{2\pi}\sigma_i} \exp\left(-\frac{\Delta\beta_i}{2\sigma_i^2}\right), \tag{10.5}$$

where $\Delta\beta_i$ is the angular difference between the Galactic latitude of the i-th event and the Galactic plane ($\beta = 0°$). The rest of the procedure is the same. We estimate the air shower density along the Galactic plane by summing all the weights in a data set. The observed density is then compared with the density obtained with scrambled data sets to search for an excess of events. The upper limit on the neutron flux is calculated with the observed and expected air shower densities.

10.4 Upper limits on the neutron flux

To determine the upper limit using the method described in Chapter 8, we use Zech's procedure [135] based on the observed and expected number of events. In Equation 6.12, we used the observed and the expected number of arrival directions. Since they are a count, both are integer numbers, and we can use a discrete distribution like a Poisson distribution. With the method described in this chapter, instead of counting the number of events in a target region, we estimate the air shower density in the direction of the target, making it impossible to use a discrete distribution.

An alternative way to estimate the upper limit on the number of events is to determine how many events are necessary to achieve a certain significance. We can start with Equation 6.11 and modify it as

$$P(\leq \rho_{\text{obs}}|\rho_{\text{exp}} + \rho_{\text{UL}}) = (1 - CL)P(\leq \rho_{\text{obs}}|\rho_{\text{exp}}), \tag{10.6}$$

and from the background expectation with mean ρ_{exp}, we can numerically find ρ_{UL}. Here, $P(\leq \rho_{\text{obs}}|\rho_{\text{exp}})$ represents the probability of getting an air shower density less or equal to ρ_{obs} when the background contribution has as mean ρ_{exp}. The background contribution is obtained with simulated data sets using the scrambling technique as explained in Section 10.2. We can simulate events to estimate an expected value of the probability density close to the target. We explain the procedure to simulate events below, in Section 10.4.1. Using the

expected weight, $\overline{w}$, we can estimate how many events are necessary to get $\rho_{\rm UL}$:

$$n_{\rm UL} = \frac{\rho_{\rm UL}}{\overline{w}}. \tag{10.7}$$

The upper limit on the neutron flux is then the upper limit on the number of neutrons, $n_{\rm UL}$, divided by the directional exposure. We can estimate the directional exposure by dividing the expected density obtained for each target by the cosmic ray intensity I:

$$\omega_{\rm dir} = \frac{\rho_{\rm exp}}{I}, \tag{10.8}$$

We present the procedure to estimate the cosmic ray intensity in Section 7.2.

10.4.1 Generating an excess

To generate an excess, we consider events close in declination to the target. We make this cut in the data set to preserve the distribution of the measured angle uncertainties since it has a slight dependence on declination. We chose 5,000 events in a declination band centered on the target's declination.

To simulate an event, we randomly sampled one event and extracted the zenith angle, θ, and the uncertainties in the zenithal and azimuthal angles, $\Delta\theta$ and $\Delta\varphi$, respectively. Using this information, we evaluate the associated standard deviation, σ, using Equation 10.1. Then, we simulated an angular distance, $\xi_{\rm sim}$, between the target and the event using the relation

$$\xi_{\rm sim} = \sigma\sqrt{-2\ln u}, \tag{10.9}$$

where u is a random number sampled from a uniform distribution between 0 and 1.

10.5 Analysis combining targets

Once we have estimated the individual p-values for each candidate source in each target set, we can apply the "stacked" analysis using the same procedure described in section 8.5 for each target set. We can estimate the unweighted and the weighted combined P-value for each target set. The weighted combined P-value takes into account the attenuation factor caused by the neutron decay, the exposure of each target to the Observatory, and the electromagnetic flux at the candidate source.

We apply the method described in this chapter in the same data sets used in the other two methods, described in Chapters 6 and 8. The results for the probability density method are presented in the next chapter.

11 RESULTS FOR THE TARGETED SEARCH: PROBABILITY DENSITY METHOD

The method described in Chapter 10 differs from the ones explained in Chapters 6 and 8. Instead of defining a target region and counting the number of events comprised within a solid angle, we estimate the probability density of an event coming from a given direction of the sky to estimate the air shower density at this point. Then, we compare the observed density with the density obtained using simulated isotropic data sets to identify an excess of events at the position of the target. This method uses the combined angular uncertainties to smear the arrival direction of the event. The combined angular uncertainty σ is given by Equation 10.1 and it depends on the angular uncertainties associated with the local coordinates, the zenith angle θ and azimuth angle φ. Ideally, we would use the angular uncertainty event-by-event. Nevertheless, upon investigating the distribution of angular uncertainties, we identified outliers exhibiting unrealistic low values of σ, measuring less than 0.2°. To bypass this issue, we decided to parameterize the angular uncertainty using the multiplicity (the number of triggered stations in an air shower event), the zenith angle, and the energy. We present the curves resulting from this parameterization in Figures 11.1, 11.2, and 11.3 for the vertical, inclined, and infill data sets, respectively. We chose 1-degree intervals in zenith angle to parameterize the selected multiplicities indicated in the figures and we sampled the events in these subsets. Then, we evaluate the median value for the σ parameter of the events in each bin. We used Equation 10.1 to estimate the σ parameter event-by-event before calculating the median values in the bins. In this way, we use the parameterized curves instead of the value obtained event-by-event. As we can observe in Figures 11.1, 11.2, and 11.3, this procedure ensures that all values used for the σ parameter are well-behaved, and we are not using any outliers.

As we can observe in Figure 11.1, for the cumulative data set ($E \geq 1$ EeV), the smallest value for multiplicity is three triggered stations. This is the minimum number of stations needed to reconstruct an event. We have events that triggered more than eight stations, but to avoid statistical fluctuations caused by the low number of events satisfying this condition, we include them in the multiplicity-eight set. The angular uncertainty decreases with the increase in multiplicity because using more stations, it is possible to reconstruct the arrival direction of the events more accurately. For the vertical events, all the σ values are smaller than 1.7°. For the energy range below 3 EeV, we use a multiplicity between three and five because events with this energy have a smaller size when compared to more energetic ones, triggering fewer stations.

Figure 11.2 shows the σ-parameterization for the inclined data set. For the cu-

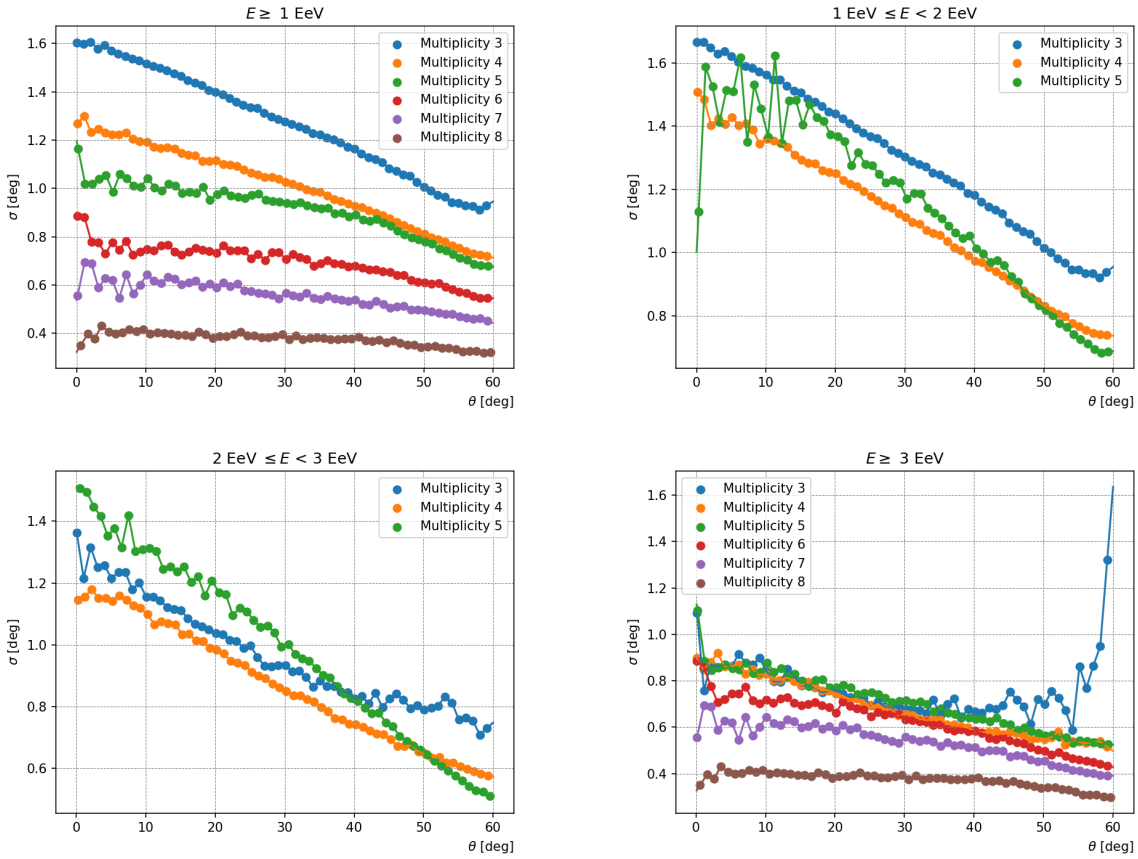

Figure 11.1: The σ parameter as a function of the zenith angle for the vertical data set. The continuous lines are a linear interpolation.

mulative data set ($E \geq 1$ EeV), as we can see, the multiplicity value varies from six to ten. Events that trigger more than ten stations are included in the multiplicity-ten set. Usually, inclined events (zenith angle larger than 60°) trigger more stations than vertical events for geometrical reasons[1]. Due to the larger number of triggered stations, inclined events have, in general, a more accurate arrival direction reconstruction when compared to vertical ones. Then, we have a better precision in the angular direction, reflecting in smaller value for the combined angular uncertainty. For the inclined events, the combined uncertainty is smaller than 1°. Even though the inclined data set has fewer events than the vertical one (353,227 inclined events versus 2,535,932 vertical events above 1 EeV), we have a shorter zenith range for inclined events ($60° < \theta \leq 80°$) than for vertical events ($0° \leq \theta \leq 60°$). Due to this shorter range, we keep the 1-degree interval in the zenith angle in the σ-parameterization.

We present the results for the σ-parameterization using the infill data set in Figure 11.3. For the cumulative data set ($E \geq 0.1$ EeV), we use multiplicities between three and ten. Events that triggered more than ten stations are included in the multiplicity-ten set. Events recorded by the infilled array have a zenith angle smaller than 55°. For this data set, we also use a 1-degree interval in zenith angle. In the infilled portion of the Observatory, the

[1]The number of triggered stations also depends on the energy of the event. The more energetic is an event, the larger is the shower size, leading to a larger number of triggered stations.

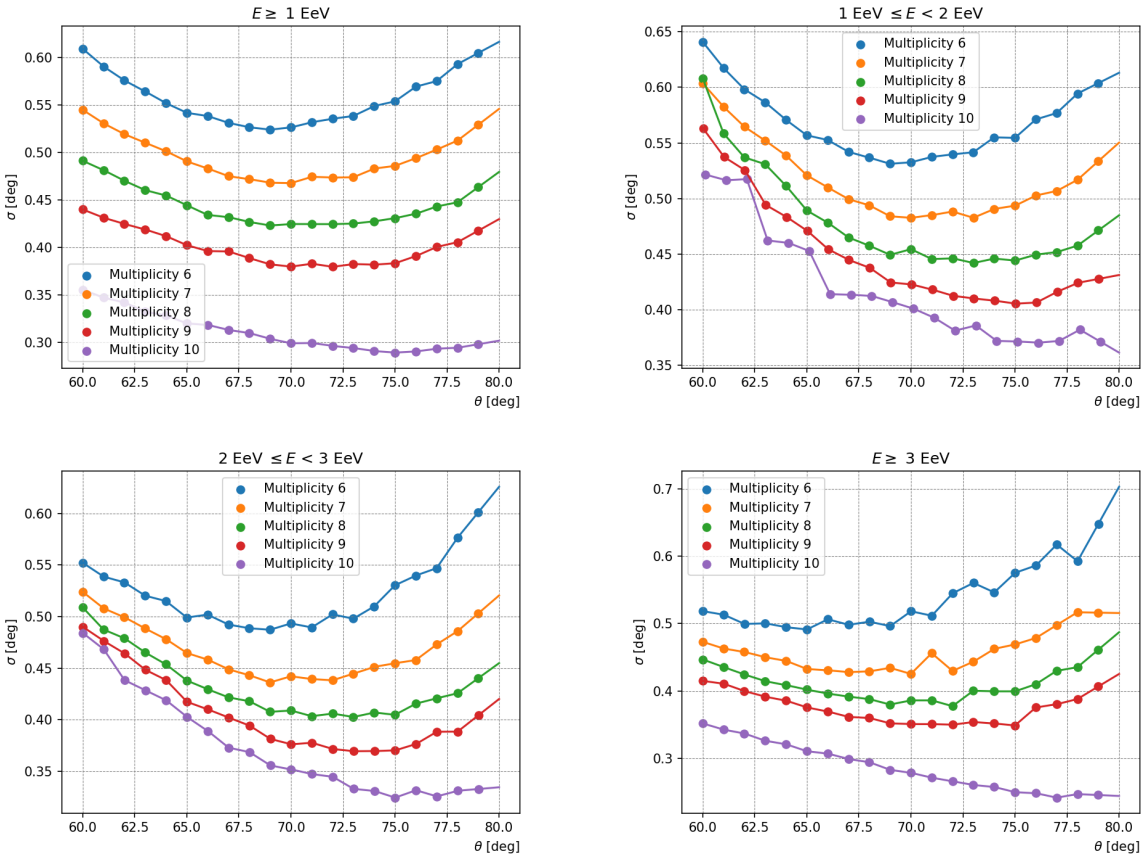

Figure 11.2: The σ parameter as a function of the zenith angle for the inclined data set. The continuous lines are a linear interpolation.

stations have a spacing of 750 m, covering an area of approximately 24 km^2. The full array covers approximately 3,000 km^2 and the stations are spaced 1,500 m from each other. We use multiplicities up to ten for the infill data set and up to eight for the vertical data set because the stations are closer to each other in the first case. Even though events have less energy in the infill data set ($E < 1$ EeV), the number of triggered stations can be larger due to the arrangement of this part of the Observatory.

We use the linear interpolation of the σ-parameterization presented in Figures 11.1, 11.2, and 11.3 to determine the σ value associated to each event. Then, we evaluate the angular distance between each event and the target that we are testing. Using the σ value and the angular distance, we calculate the weight associated with each event with Equation 10.2. Once we have the weights for all events in the data set, we estimate the air shower density at the position of the tested target using Equation 10.3. We compare the observed density with the densities obtained using scrambled data sets as explained in Section 10.2 to investigate excesses of events that could indicate a neutron flux. In the next sections, we present the results obtained using this method for the vertical, inclined, and infill data sets.

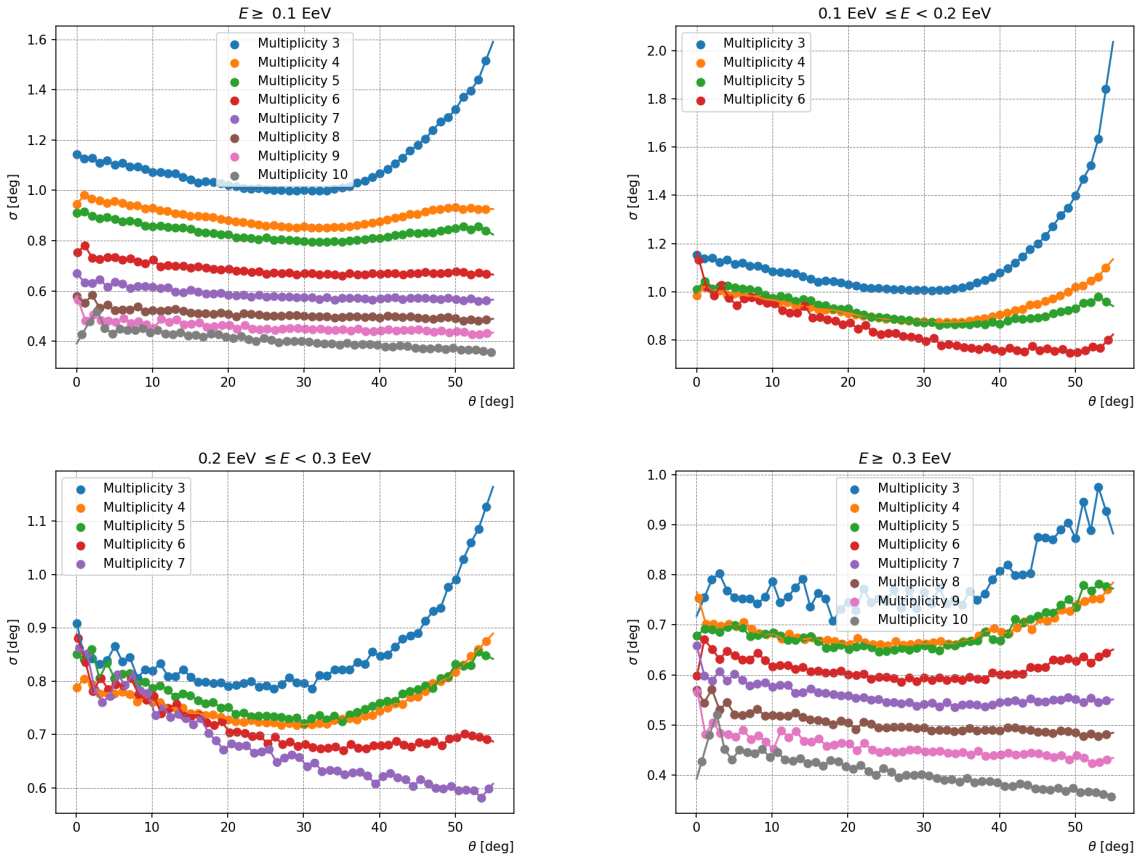

Figure 11.3: The σ parameter as a function of the zenith angle for the infill data set. The continuous lines are a linear interpolation.

11.1 Vertical data set

As in the other two methods that we present in this thesis for the neutron search, we split each data set into four energy ranges. In this section, we present the results for the vertical data set. We use the observed and the simulated density (using the scrambling technique) to estimate the p-value associated with each target. A p-value close to 1 indicates that we do not have an excess of events since $p = 1$ means that 100% of the simulated data sets have an air shower density larger than the observed. The smaller the p-value, the more significant the candidate source.

In Table 11.1, we present the results for the cumulative vertical data set. We report the results for the most significant target in each target set. The most significant candidate source is the one with the smallest individual p-value. For the most significant target in each target set, we report its direction, the observed and expected air shower density in its direction, as well as the upper limit for the neutron flux and the energy flux, the p-value, and the penalized p-value. The penalized p-value, given by $p^* = 1 - (1 - p)^M$, takes into account the fact that we are testing M targets in each target set.

The smallest individual p-value is 0.0018 associated with a γ-ray pulsar located at $(296.64°, -54.06°)$. The penalized p-value for this target, considering that we are testing 167

Table 11.1: Results for the most significant target in each target set for the vertical data set and events with energy above 1 EeV.

Results for the targeted search - vertical data set - $E \geq 1$ EeV								
Class	**RA [deg]**	**Dec [deg]**	**Observed ρ** [deg^{-2}]	**Expected ρ** [deg^{-2}]	**Flux U.L.** [km^{-2} yr^{-1}]	**E-flux U.L.** [eV cm^{-2} s^{-1}]	p**-value**	p**-value (penalized)**
msec PSRs	218.83	−61.02	135.45	126.47	0.012	0.089	0.0064	0.60
γ-ray PSRs	296.64	−54.06	135.59	125.66	0.014	0.10	0.0018	0.26
LMXB	117.14	−67.75	134.95	126.75	0.011	0.078	0.013	0.73
HMXB	286.20	9.04	53.99	48.28	0.015	0.11	0.015	0.53
H.E.S.S. PWN	154.50	−58.92	129.67	126.05	0.0082	0.060	0.15	0.82
H.E.S.S. other	282.12	−1.79	76.71	71.77	0.012	0.091	0.038	0.44
H.E.S.S. UNID	284.40	2.97	66.47	61.98	0.013	0.092	0.052	0.78
Microquasars	275.50	−37.02	118.51	115.51	0.0091	0.066	0.16	0.90
Magnetars	286.81	9.32	52.71	47.64	0.014	0.10	0.026	0.48
Gal. Center	266.42	−29.01	103.42	108.71	0.0035	0.025	0.97	0.97

γ-ray pulsars, is 0.26. This means that we have a 26% chance of getting a p-value equal to or less than 0.0018 if all the 167 p-values were randomly sampled from a uniform distribution between 0 and 1. As we can observe in Table 11.1, considering the penalized p-values, we do not have any clear evidence of a neutron flux coming from any of the tested directions, supporting the results presented in Chapter 9 obtained with the method described in Chapter 8. We tested the other three energy ranges, and we did not find any significant target either. The results for the other energy ranges are presented in Appendix D in Tables D.1, D.2, and D.3.

For the special case of the Galactic plane, the results for the vertical data set in all energy ranges are presented in Table 11.2. For this specific target, we also assign a σ value for each event using the parameterization presented in Figure 11.1. Then, we use the angular difference between the Galactic latitude of the event and plane (Galactic latitude of 0°) to calculate the weight associated to this event using Equation 10.5. We sum all the weights in the data set to estimate the observed density. Then we compare with the values obtained using 10,000 isotropic simulated data sets to obtain the p-value. We investigate a neutron flux from the Galactic plane in all four energy ranges. As we can observe in Table 11.2, the p-values are between 0.18 and 0.64. These p-values indicate that we do not have a significant excess of events coming from the Galactic plane. Both with the method described in Chapter 8, in which we used a top-hat function to define a limited region of the sky and determine the number of events inside this region, and with this method we are discussing in this section (described in Chapter 10), we do not identify any significant excess that could indicate a neutron flux coming from the Galactic plane region.

As in the method described in Chapter 8, in which we have a well-defined target region in which we search for an excess of events, we can combine the p-values obtained with the method of assigning a weight for each event to estimate the air shower density to investigate if one of the classes of astrophysical objects is emitting neutrons. If a target set is, in fact, producing neutrons, the combined P-value would be more significant than its individual p-values. We combined the individual p-values as explained in Section 8.5. We combined the p-values using Equation 8.6 (unweighted combined P-value). We also include statistical weights proportional to the electromagnetic flux at the candidate source, to the exposure of the Observatory in the direction of the target, and to the expected attenuation factor caused by the decay during the neutron propagation from the candidate source to the Earth. We present the results for the combined analysis for the cumulative vertical data set in Table 11.3. The smallest unweighted combined P-value is 0.66 associated to the other sources identified by the H.E.S.S. experiment (H.E.S.S. other). This target set contains 15 candidate sources. The weighted P-value for this class is 0.90. The smallest weighted combined P-value is 0.024 associated with the 167 γ-ray pulsars. The unweighted combined P-value for this class is 0.82. Therefore, we do not find any significant target set neither in this energy range nor in the other ones. The results for the other energy ranges are presented

in Tables D.4, D.5, and D.6. These negative results for excesses support the results obtained with the method described in Chapter 8 and presented in Tables 9.3, C.4, C.5, and C.6.

Table 11.2: Results for the Galactic plane for the vertical data set.

Results for the Galactic plane - Vertical data set					
Energy range	**Observed ρ** $[\mathrm{deg}^{-1}]$	**Expected ρ** $[\mathrm{deg}^{-1}]$	**Flux U.L.** $[\mathrm{km}^{-2}\,\mathrm{yr}^{-1}]$	**E-flux U.L.** $[\mathrm{eV\,cm}^{-2}\,\mathrm{s}^{-1}]$	**p-value**
$E \geq 1$ EeV	22079.44	22043.16	0.016	0.12	0.32
$1 \leq E/\mathrm{EeV} \leq 2$	16997.93	16976.67	0.015	0.11	0.37
$2 \leq E/\mathrm{EeV} \leq 3$	3042.04	3012.58	0.0055	0.040	0.18
$E \geq 3$ EeV	2042.23	2054.07	0.0027	0.020	0.64

Table 11.3: Results for the combined analysis for the vertical data set with events above 1 EeV.

Results for combined analysis - Vertical data set - $E \geq 1$ EeV			
Class	**Number of targets**	**P-value (unweighted)**	**P-value (weighted)**
msec PSRs	142	0.85	0.59
γ-ray PSRs	167	0.82	0.024
LMXB	95	0.87	0.26
HMXB	52	0.90	0.52
H.E.S.S. PWN	11	0.93	0.79
H.E.S.S. other	15	0.66	0.90
H.E.S.S. UNID	28	0.96	0.98
Microquasars	13	0.74	0.65
Magnetars	25	1.0	1.0
Gal. Center	1	0.97	0.97

11.2 Inclined data set

The results using the cumulative inclined data set ($E \geq 1$ EeV) and applying the method described in Chapter 10 defining the probability density for each event and then estimating the air shower density at the direction of the target are presented in Table 11.6. These results correspond to the most significant target in each target set (the target with the smallest individual p-value), including the direction of the target, the observed and expected air shower density from its direction, the upper limit on the flux and the energy flux, the p-value, and the penalized p-value. The smallest individual p-value (penalized p-value) is 0.0013 (0.069) corresponding to a high-mass binary system located at $(195.49°, -63.97°)$. Therefore, we do not have any clear indication of an excess of events indicating a neutron flux in any of the tested directions. We performed this analysis for the other three energy ranges and, for those

cases, we also do not find any significant targets. These results are presented in the Appendix D, in Tables D.7, D.8, and D.9.

We also tested the Galactic plane as a single-element target set, following the procedure described in 10.3. We present the results for the inclined data set in each energy range in Table 11.4. We report the observed and expected densities, the upper limit on the neutron flux and on the energy flux, and the p-value. The smallest p-value is 0.35 for the data set with events with an energy between 2 EeV and 3 EeV. This p-value means that in 35% of the isotropic simulated data sets, we obtained an air shower density greater than the observed one. Considering the obtained p-values, we also do not find any indication of a signal of an excess in the flux of events coming from the Galactic plane using the inclined data set.

Table 11.4: Results for the Galactic plane for the inclined data set.

Results for the Galactic plane - Inclined data set					
Energy range	**Observed ρ** [deg^{-1}]	**Expected ρ** [deg^{-1}]	**Flux U.L.** [km^{-2} yr^{-1}]	**E-flux U.L.** [eV cm^{-2} s^{-1}]	p-**value**
$E \geq 1$ EeV	2913.93	2925.72	0.027	0.20	0.61
$1 \leq E/\text{EeV} \leq 2$	1488.10	1510.05	0.027	0.20	0.78
$2 \leq E/\text{EeV} \leq 3$	761.42	752.83	0.0082	0.060	0.35
$E \geq 3$ EeV	659.08	662.75	0.0047	0.034	0.56

For the combined analysis, we present the results for the cumulative data set in Table 11.5. We combine the individual p-values to obtain the probability of a class being responsible for emitting neutrons. We report the results without and including statistical weights. The smallest combined P-value is associated with the 33 unidentified sources detected by the H.E.S.S. experiment (both unweighted and weighted). The (weighted) unweighted combined P-value is (0.040) 0.0058. As we can observe in Table 11.5, we do not have any significant classes. The same is valid for the other energy ranges used in this analysis. The results for the other energy ranges are presented in Tables D.10, D.11, and D.12. This conclusion is the same one obtained with the method described in Chapter 8 (the results are presented in Tables 9.6, C.10, C.11, and C.12). For both methods, we do not find any clear indication that one of the classes studied in this work is responsible for emitting neutrons with the inclined data set.

Table 11.6: Results for the most significant target in each target set for the inclined data set and events with energy above 1 EeV.

Results for the targeted search - Inclined data set - $E \geq 1$ EeV								
Class	**RA [deg]**	**Dec [deg]**	**Observed ρ** $[\mathrm{deg}^{-2}]$	**Expected ρ** $[\mathrm{deg}^{-2}]$	**Flux U.L.** $[\mathrm{km}^{-2}\ \mathrm{yr}^{-1}]$	**E-flux U.L.** $[\mathrm{eV\ cm}^{-2}\ \mathrm{s}^{-1}]$	p**-value**	p**-value (penalized)**
msec PSRs	302.69	−13.40	12.52	7.15	0.030	0.22	0.0031	0.42
γ-ray PSRs	212.60	−61.54	25.80	16.80	0.020	0.15	0.0014	0.23
LMXB	259.70	−32.18	12.94	7.98	0.026	0.19	0.0096	0.62
HMXB	195.49	−63.97	31.32	20.62	0.019	0.14	0.0013	0.069
H.E.S.S. PWN	279.41	−6.95	10.39	7.21	0.022	0.16	0.046	0.46
H.E.S.S. other	259.49	−37.44	9.94	8.51	0.014	0.10	0.22	0.98
H.E.S.S. UNID	280.95	−3.55	12.16	7.32	0.028	0.21	0.0091	0.26
Microquasars	248.50	−47.43	12.77	10.08	0.016	0.12	0.11	0.80
Magnetars	162.53	−59.89	20.73	15.36	0.016	0.12	0.028	0.52
Gal. Center	266.42	−29.01	8.57	7.75	0.014	0.10	0.31	0.31

Table 11.5: Results for the combined analysis for the inclined data set with events above 1 EeV.

Results for combined analysis - Inclined data set - $E \geq 1$ EeV			
Class	**Number of targets**	**P-value (unweighted)**	**P-value (weighted)**
msec PSRs	175	0.039	0.48
γ-ray PSRs	187	0.12	0.28
LMXB	99	0.68	0.56
HMXB	55	0.61	0.28
H.E.S.S. PWN	13	0.88	0.12
H.E.S.S. other	16	0.95	0.60
H.E.S.S. UNID	33	0.0058	0.040
Microquasars	14	0.72	0.78
Magnetars	26	0.42	0.76
Gal. Center	1	0.31	0.31

11.3 Infill data set

We also applied the method described in Chapter 10 in the infill data set. The events recorded with the infilled array have energy starting at 0.1 EeV and zenith angle less than 55°. The smallest individual p-value is 0.0035 associated with a γ-ray pulsar (located at a right ascension of 274.29° and a declination of −17.70°). We tested 136 γ-ray pulsars, resulting in a penalized p-value of 0.38. The smallest penalized p-value is 0.088, associated with a microquasar located at (274.88°, −16.42°). The p-value before the penalization is 0.0083. For this data set, we tested 11 microquasars. The upper limit on the neutron flux is larger than for the vertical and inclined data sets. We can compare these upper limits by looking at Tables 11.1 and 11.6. The upper limit on the flux is larger for the events detected by the infilled portion of the array because the flux of events is larger. The flux decreases with energy, as discussed in Chapter 2, and the infill data set has events with energy starting in 0.1 EeV (an order of magnitude less than the other two data sets).

For the infill data set, as in the other ones considered in this analysis, we do not find any indication of a neutron flux when analyzing this data set neither for the cumulative data set nor for the other energy ranges. The results for the other energy ranges are presented in Tables D.13, D.14, and D.15.

Using the infill data set, we perform a search for neutron flux as described in Section 10.3. We assign a combined angular uncertainty of each event using the parameterization shown in Figure 11.3. Then we estimate the weights for each event in the data set using Equation 10.5 to determine the air shower density, used to calculate the p-value. In Ta-

Table 11.7: Results for the most significant target in each target set for the infill data set and events with energy above 0.1 EeV.

Results for the targeted search - Infill data set - $E \geq 0.1$ EeV								
Class	**RA [deg]**	**Dec [deg]**	**Observed ρ** [deg^{-2}]	**Expected ρ** [deg^{-2}]	**Flux U.L.** [km^{-2} yr^{-1}]	**E-flux U.L.** [eV cm^{-2} s^{-1}]	**p-value**	**p-value (penalized)**
msec PSRs	232.31	−38.48	125.26	118.39	2.2	16.0	0.027	0.92
γ-ray PSRs	274.29	−17.70	103.33	94.17	3.0	22.0	0.0035	0.38
LMXB	273.63	−17.16	101.91	93.21	3.0	22.0	0.0041	0.31
HMXB	116.85	−53.33	129.37	120.36	2.5	18.0	0.0082	0.31
H.E.S.S. PWN	169.75	−61.40	118.82	114.36	1.8	13.0	0.11	0.71
H.E.S.S. other	84.00	−67.59	108.69	104.96	1.7	13.0	0.15	0.83
H.E.S.S. UNID	273.34	−12.69	92.23	84.91	2.8	21.0	0.0093	0.14
Microquasars	274.88	−16.42	100.03	91.90	2.9	21.0	0.0083	0.088
Magnetars	274.52	−16.13	98.60	91.36	2.7	20.0	0.014	0.28
Gal. Center	266.42	−29.01	113.49	110.24	1.8	13.0	0.17	0.17

ble 11.8, we report the observed and expected densities, the upper limit on the flux and the energy flux, and the p-value for all the four energy ranges considered in this analysis. The p-values vary from 0.25 to 0.84. Therefore, we do not observe a clear indication of a neutron flux coming from the Galactic plane using the infill data set.

Table 11.8: Results for the Galactic plane for the infill data set.

Results for the Galactic plane - Infill data set					
Energy range	**Observed ρ** [deg^{-1}]	**Expected ρ** [deg^{-1}]	**Flux U.L.** [km^{-2} yr^{-1}]	**E-flux U.L.** [eV cm^{-2} s^{-1}]	**p-value**
$E \geq 0.1$ EeV	20249.80	20255.59	2.9	21.0	0.53
0.1 – 0.2 EeV	14926.54	14883.27	3.7	27.0	0.25
0.2 – 0.3 EeV	3252.68	3277.69	0.70	5.1	0.76
$E \geq 0.3$ EeV	2062.87	2095.10	0.43	3.1	0.84

We present the results for the combined analysis for the cumulative infill data set in Table 11.9. We combine the individual candidate sources to try to identify a stronger significance in a specific class. This would indicate that the objects of this specific class were emitting neutrons. We combine the individual p-values to obtain an unweighted combined P-value, and then we include statistical weights to obtain the weighted combined P-value. In this table, we report the total number of targets, besides the unweighted and weighted combined P-value for each target set. The smallest unweighted combined P-value is 0.093 and it is associated with the 11 microquasars. This target set has also the smallest weighted combined P-value (0.016). Considering the combined P-values, we do not identify a stronger significance in a specific class for the cumulative data set. We combined the p-values for the other energy ranges, obtaining the same conclusion. The results for the other energy ranges are presented in Tables D.16, D.17, and D.18.

After investigating three different data sets, each one split into four energy ranges[2], using the probability density method, we did not identify a significant neutron flux. Even though we did not find a neutron source in the EeV range, we reported the results for the most significant target in each set, establishing upper limits on the neutron flux and on the energy flux for these directions. We also presented the results for the combined analysis.

11.4 Final considerations

In conclusion, we performed the neutron search using three different methods, described in Chapter 6, 8, and 10. The first one is a blind search, investigating targets covering the full field of the view accessed by each data set. The other two are targeted methods, in which we narrowed down the search to specific directions from which we have known candidate

[2]One of these four energy ranges is the cumulative data set of the other three.

Table 11.9: Results for the combined analysis for the infill data set with events above 0.1 EeV.

Results for combined analysis - Infill data set - $E \geq$ 0.1 EeV			
Class	**Number of targets**	**P-value (unweighted)**	**P-value (weighted)**
msec PSRs	90	0.39	0.76
γ-ray PSRs	136	0.96	0.89
LMXB	89	0.71	0.59
HMXB	45	0.54	0.97
H.E.S.S. PWN	11	0.29	0.12
H.E.S.S. other	11	0.47	0.64
H.E.S.S. UNID	16	0.14	0.27
Microquasars	11	0.093	0.016
Magnetars	23	0.60	0.77
Gal. Center	1	0.17	0.17

sources. The method described in Chapter 6 and the one described in Chapter 8 were published by the Auger Collaboration in 2012 [1] and in 2014 [2], respectively. In this thesis, we updated these results including more data, using events recorded up to 2022. The method described in Chapter 10 is a new method for neutron searches, offering a more realistic way to associate events with targets since we consider all the events in the data set to estimate the air shower density. We reported upper limits on the neutron flux for the three methods. These upper limits can be used to restrict astrophysical models of cosmic ray production. We discuss the implications of these negative results for the neutron search in the next chapter.

12 CONCLUSIONS

Identifying the sources of ultra-high-energy cosmic rays (UHECRs) is one of the biggest challenges in astroparticle physics. The study of the arrival direction distribution of cosmic rays is one of the main tools to investigate these sources and understand the mechanisms behind the acceleration of ultra-high-energy (UHE) particles in astrophysical environments.

One of the main challenges, when we are trying to identify the sources of such high-energy particles, is that most of the cosmic rays are charged particles, and thus, magnetic fields present in the interstellar medium deflect them. A way to bypass this problem is to study neutral particles since they will point directly to their sources. We expect neutron production in the vicinity of the sources of UHE protons. Therefore, the goal of this thesis is to try to identify a neutron flux by analyzing data collected at the Pierre Auger Observatory to identify the sources of UHECRs.

In this work, we presented three methods to search for point sources of neutrons. Since air showers initiated by neutrons are indistinguishable from those created by protons, we try to identify an excess of events in a small region of the sky around the targets. Since neutrons are undeflected by magnetic fields, on a small scale, we would observe an event excess caused by the undeflected neutral particles.

The method presented in Chapter 6 is a blind search. In this method, we searched the whole sky, considering the Observatory's field of view, to identify small-scale anisotropies that could indicate neutron fluxes. We defined a target region using a top-hat function and compared the observed number of events with the expected number from the background signal. We estimated the background signal using simulated data sets built from the scrambling of the observed data set. This technique allowed us to preserve the actual exposure of the Observatory, erasing any local excess of events. We also estimated the upper limit on the neutron flux.

In Chapter 8, we described a method similar to the blind search, in which we used a top-hat function to determine a target region and try to identify an excess of events. However, instead of looking for the whole sky within the field of view of the Observatory, we selected specific directions where potential sources are located. We studied the number of events around these directions compared with the background signal.

Finally, we presented a method that, instead of limiting a region of the sky around a target, defines a probability density, estimating the chance of each event coming from its direction. We smeared the arrival direction of the events, considering the angular uncertainties measured at the Observatory, and used the probability density to estimate the air shower

density in the position of the target. This method offers the advantage of including all events in the data set for each target tested.

We presented the results for the three methods in Chapters 7, 9, and 11. The Auger Collaboration has published the results for the methods described in Chapters 6 and 8 in 2012 [1] and 2014 [2], respectively. In these two works, the Collaboration studied vertical events, i.e., events with a zenith angle between 0° and 60°. With total exposure of 24,880 km^2 sr yr in the 2012 work[1] and 35,967 km^2 sr yr in 2014 [2], we have 429,138 and 854,270 events with energy above 1 EeV, respectively. In this thesis, we studied an updated version of the vertical data set with a total exposure of 79,865 km^2 sr yr yielding 2,535,932 events above 1 EeV. In this thesis, we also studied two new data sets: the inclined data sets, with a zenith angle between 60° and 80°, and the infill data set including events in a lower energy range starting at 0.1 EeV. A full description of the data sets used in this work can be found in Chapter 4.

In the previous studies, using data from cosmic rays detected at the Pierre Auger Observatory, the main result was the absence of any significant excess of events that could indicate the presence of a neutron flux. By studying new data sets and updating both the vertical data set and the studied catalogs of candidate sources, we come to the same conclusion.

The fact that we did not identify a neutron source opens some possibilities. A positive detection is more straightforward since the detection of a neutron flux indicates the presence of a cosmic ray source in the EeV range. The negative result can be explained by different scenarios. For example, if neutrons are propagating in a more diffusive way than we assumed, we would not be able to identify them. An alternative option is that neutrons are produced only in transient events, such as in γ-ray bursts. Another possibility is that neutrons are produced outside our Galaxy. In this scenario, they would decay before reaching the Earth. In the coming years, upcoming data may enable the detection of a UHE neutron flux, thereby allowing the identification of UHECR sources.

[1] The data set used in this work contains events recorded from January 2004 to September 2011.
[2] The data set used in this work contains events recorded from January 2004 to October 2013.

BIBLIOGRAPHY

[1] Abreu, P. *et al.* A search for point sources of EeV neutrons. *The Astrophysical Journal* **760**, 148 (2012).

[2] Aab, A. *et al.* A targeted search for point sources of EeV neutrons. *The Astrophysical Journal Letters* **789**, L34 (2014).

[3] Röntgen, W. C. On a new kind of rays. *Science* **3**, 227–231 (1896).

[4] Becquerel, A. H. On radioactivity, a new property of matter. *Les prix Nobel* (1903).

[5] Rutherford, E. Uranium radiation and the electrical conduction produced by it. *Philosophical Magazine Series* **47**, 109–163 (1899).

[6] Villard, P. Sur la réflexion et la réfraction de rayons cathodiques et des rayons déviables du radium. *Comptes rendus* **130**, 1010–1011 (1900).

[7] Wilson, C. T. R. On the ionisation of atmospheric air. *Proceedings of the Royal Society of London* **68**, 151–161 (1901).

[8] Wulf, T. Beobachtungen über Strahlung hoher Durchdringungsfähigkeit auf dem Eiffelturm. *Physikalische Zeitschrift* **11**, 811–813 (1910).

[9] Hess, V. F. Über Beobachtungen der durchdringenden Strahlung bei sieben Freiballonfahrten. *Physikalische Zeitschrift* **13**, 1084–1091 (1912).

[10] Kolhörster, W. Messungen der durchdringenden Strahlung im Freiballon in größeren Höhen. *Physikalische Zeitschrift* **14**, 1153–1156 (1913).

[11] Bothe, W. & Kolhörster, W. Das Wesen der Höhenstrahlung. *Zeitschrift fur Physik* **56**, 751–777 (1929).

[12] Geiger, H. & Müller, W. Elektronenzählrohr zur Messung schwächster Aktivitäten. *Naturwissenschaften* **16**, 617–618 (1928).

[13] Millikan, R. A. & Cameron, G. H. The origin of the cosmic rays. *Physical Review* **32**, 533–557 (1928).

[14] Rossi, B. Über die Eigenschaften der durchdringenden Korpuskularstrahlung im Meeresniveau. *Zeitschrift für Physik* **82**, 151–178 (1933).

[15] Rossi, B. Misure sulla distribuzione angolare di intensità della radiazione penetrante all'Asmara. *Supplemento a la Ricerca Scientifica* **1**, 579 (1934).

[16] Schmeiser, K. & Bothe, W. Die harten Ultrastrahlschauer. *Annalen der Physik* **424**, 161–177 (1938).

[17] Auger, P., Ehrenfest, P., Maze, R., Daudin, J. & Fréon, R. A. Extensive Cosmic-Ray Showers. *Reviews of Modern Physics* **11**, 288–291 (1939).

[18] Pfotzer, G. Dreifachkoinzidenzen der Ultrastrahlung aus vertikaler Richtung in der Stratosphäre. *Zeitschrift für Physik* **102**, 41–58 (1936).

[19] Schein, M., Jesse, W. P. & Wollan, E. O. The nature of the primary cosmic radiation and the origin of the mesotron. *Physical Review* **59**, 615–615 (1941).

[20] Anderson, C. D. The positive electron. *Physical Review* **43**, 491–494 (1933).

[21] Neddermeyer, S. H. & Anderson, C. D. Note on the nature of cosmic-ray particles. *Physical Review* **51**, 884–886 (1937).

[22] Lattes, C. M., Muirhead, H., Occhialini, G. P. & Powell, C. F. Processes involving charged mesons. *Nature* **159**, 694–697 (1947).

[23] Rochester, G. D. & Butler, C. C. Evidence for the existence of new unstable elementary particles. *Nature* **160**, 855–857 (1947).

[24] Hopper, V. D. & Biswas, S. Evidence concerning the existence of the new unstable elementary neutral particle. *Physical Review* **80**, 1099–1100 (1950).

[25] Abreu, P. *et al.* Arrival directions of cosmic rays above 32 EeV from phase one of the Pierre Auger Observatory. *The Astrophysical Journal* **935**, 170 (2022).

[26] Antares, IceCube, Pierre Auger and TA Collaborations. Search for spatial correlations of neutrinos with ultra-high-energy cosmic rays. *The Astrophysical Journal* **934**, 164 (2022).

[27] Aab, A. *et al.* A targeted search for point sources of EeV photons with the Pierre Auger Observatory. *The Astrophysical Journal Letters* **837**, L25 (2017).

[28] Aab, A. *et al.* Search for photons with energies above 10^{18} eV using the hybrid detector of the Pierre Auger Observatory. *Journal of Cosmology and Astroparticle Physics* **2017**, 009 (2017).

[29] Abreu, P. *et al.* A search for photons with energies above 2×10^{17} eV using hybrid data from the low-energy extensions of the Pierre Auger Observatory. *The Astrophysical Journal* **933**, 125 (2022).

[30] Pierre Auger Collaboration *et al.* Observation of a large-scale anisotropy in the arrival directions of cosmic rays above 8×10^{18} eV. *Science* **357**, 1266–1270 (2017).

[31] Kampert, K.-H., Alejandro Mostafa, M., Zas, E. & Collaboration, P. A. Multi-messenger physics with the Pierre Auger Observatory. *Frontiers in Astronomy and Space Sciences* **6**, 24 (2019).

[32] Blümer, J., Engel, R. & Hörandel, J. R. Cosmic rays from the knee to the highest energies. *Progress in Particle and Nuclear Physics* **63**, 293–338 (2009).

[33] Thoudam, S. *et al.* Cosmic-ray energy spectrum and composition up to the ankle: the case for a second Galactic component. *Astronomy & Astrophysics* **595**, A33 (2016).

[34] Aab, A. *et al.* Measurement of the cosmic-ray energy spectrum above 2.5×10^{18} eV using the Pierre Auger Observatory. *Physical Review D* **102**, 062005 (2020).

[35] Gleeson, L. & Axford, W. Solar modulation of Galactic cosmic rays. *Astrophysical Journal, vol. 154, p. 1011* **154**, 1011 (1968).

[36] Kulikov, G. & Khristiansen, G. On the size spectrum of extensive air showers. *Soviet Physics — JETP* **35**, 441–444 (1959).

[37] Giacinti, G., Kachelrieß, M. & Semikoz, D. Escape model for Galactic cosmic rays and an early extragalactic transition. *Physical Review D* **91**, 083009 (2015).

[38] Linsley, J. Primary cosmic rays of energy 10^{17} to 10^{20} eV, the energy spectrum and arrival directions. In *8th International Cosmic Ray Conference*, vol. 4 of *Proceedings of the 8th International Cosmic Ray Conference*, 77 (1963).

[39] Lawrence, M., Reid, R. & Watson, A. The cosmic ray energy spectrum above 4×10^{17} eV as measured by the Haverah Park array. *Journal of Physics G: nuclear and particle physics* **17**, 733 (1991).

[40] Bird, D. J. *et al.* Evidence for correlated changes in the spectrum and composition of cosmic rays at extremely high energies. *Physical Review Letters* **71**, 3401–3404 (1993).

[41] Aloisio, R., Berezinsky, V. & Gazizov, A. Transition from Galactic to extragalactic cosmic rays. *Astroparticle Physics* **39**, 129–143 (2012).

[42] Seo, E. S. *et al.* Measurement of cosmic-ray proton and helium spectra during the 1987 solar minimum. *Astrophysical Journal* **378**, 763 (1991).

[43] Grigorov, N., Rapoport, I., Savenko, I., Nesterov, V. & Prokhin, V. Energy Spectrum of Cosmic Ray α-particles in $5 \times 10^{10} - 10^{12}$ eV/Nucleon Energy Range. In *12th International Cosmic Ray Conference (ICRC12)*, vol. 5, 1760 (1971).

[44] Afanasiev, B. N. *et al.* New project and new detection techniques for the highest energies in Yakutsk EAS array. In *ICRR International Symposium on Extremely High-energy Cosmic Rays: Astrophysics and Future Observatories* (1996).

[45] Nagano, M. *et al.* Energy spectrum of primary cosmic rays above $10^{17.0}$ eV determined from extensive air shower experiments at Akeno. *Journal of Physics G: Nuclear and Particle Physics* **18**, 423 (1992).

[46] Bird, D. J. *et al.* The Cosmic-Ray Energy Spectrum Observed by the Fly's Eye. *Astrophysical Journal* **424**, 491 (1994).

[47] Abbasi, R. U. *et al.* First Observation of the Greisen-Zatsepin-Kuzmin Suppression. *Physical Review Letters* **100**, 101101 (2008).

[48] Abraham, J. *et al.* Observation of the suppression of the flux of cosmic rays above 4×10^{19} eV. *Physical Review Letters* **101**, 061101 (2008). 0806.4302.

[49] Abbasi, R. *et al.* Measurement of the flux of ultra high energy cosmic rays by the stereo technique. *Astroparticle Physics* **32**, 53–60 (2009).

[50] Hanlon, W. Cosmic ray spectra of various experiments. URL https://web.physics.utah.edu/~whanlon/spectrum.html.

[51] Abraham, J. *et al.* Measurement of the energy spectrum of cosmic rays above 10^{18} eV using the Pierre Auger Observatory. *Physics Letters B* **685**, 239–246 (2010).

[52] Settimo, M. for the Pierre Auger Collaboration. Measurement of the cosmic ray energy spectrum using hybrid events of the Pierre Auger Observatory. *The European Physical Journal Plus* **127**, 1–15 (2012).

[53] Aab, A. *et al.* Features of the energy spectrum of cosmic rays above 2.5×10^{18} eV using the Pierre Auger Observatory. *Physical Review Letters* **125**, 121106 (2020).

[54] (The Pierre Auger Collaboration), P., Abreu *et al.* The energy spectrum of cosmic rays beyond the turn-down around 10^{17} eV as measured with the surface detector of the Pierre Auger Observatory. *The European Physical Journal C* **81**, 1–25 (2021).

[55] Seo, E. *et al.* Cosmic ray energetics and mass for the International Space Station (ISS-CREAM). *Advances in Space Research* **53**, 1451–1455 (2014).

[56] The Pierre Auger Collaboration. The Pierre Auger Cosmic Ray Observatory. *Nuclear Instruments and Methods in Physics Research Section A: Accelerators, Spectrometers, Detectors and Associated Equipment* **798**, 172–213 (2015).

[57] Heitler, W. *The quantum theory of radiation* (Courier Corporation, 1984).

[58] Workman, R. L. *et al.* (Particle Data Group). Review of Particle Physics. *Progress of theoretical and experimental physics* **2022**, 083C01 (2022).

[59] The Pierre Auger Collaboration & Yushkov, A. Mass composition of cosmic rays with energies above $10^{17.2}$ eV from the hybrid data of the Pierre Auger Observatory. In *PoS ICRC2019* (2020).

[60] Hörandel, J. R. Cosmic-ray abundances and energy spectra at high energies: Measurements with TRACER and KASCADE. *Advances in Space Research* **38**, 1549–1557 (2006).

[61] Simpson, J. Elemental and isotopic composition of the Galactic cosmic rays. *Annual Review of Nuclear and Particle Science* **33**, 323–382 (1983).

[62] Fowler, P. *et al.* High resolution study of nucleonic cosmic rays with $Z \geq 34$. *Nuclear Instruments and Methods* **147**, 195–199 (1977).

[63] Fowler, P. H. *et al.* Ariel 6 Measurements of the Fluxes of Ultra-heavy Cosmic Rays. *Astrophysical Journal* **314**, 739 (1987).

[64] Binns, W. *et al.* Abundances of ultraheavy elements in the cosmic radiation: results from HEAO 3. *Astrophysical Journal* **346**, 997–1009 (1989).

[65] Shirk, E. & Price, P. Charge and energy spectra of cosmic rays with $Z \gtrsim 60$: The SKYLAB experiment. *The Astrophysical Journal* **220**, 719–733 (1978).

[66] Lawrence, D. *et al.* Large-area scintillating-fiber time-of-flight/hodoscope detectors for particle astrophysics experiments. *Nuclear Instruments and Methods in Physics Research Section A: Accelerators, Spectrometers, Detectors and Associated Equipment* **420**, 402–415 (1999).

[67] Weaver, B. A. & Westphal, A. J. The Extended Analysis of the Trek Detector. In *27th International Cosmic Ray Conference*, vol. 5 of *Proceedings of the 27th International Cosmic Ray Conference*, 1720 (2001).

[68] Binns, W. *et al.* Cosmic-ray abundances of elements with atomic number $26 \leq Z \leq 40$ measured on HEAO-3. *Astrophysical Journal Letters* **247**, L115–L118 (1981).

[69] Donnelly, J. New results on the relative abundance of actinides in the cosmic radiation. In *26th International Cosmic Ray Conference (ICRC26)*, vol. 3, 109 (1999).

[70] Lodders, K. Solar system abundances and condensation temperatures of the elements. *The Astrophysical Journal* **591**, 1220 (2003).

[71] Greisen, K. End to the cosmic-ray spectrum? *Physical Review Letters* **16**, 748 (1966).

[72] Zatsepin, G. T. & Kuz'min, V. A. Upper Limit of the Spectrum of Cosmic Rays. *Soviet Journal of Experimental and Theoretical Physics Letters* **4**, 78 (1966).

[73] Fixsen, D. The temperature of the cosmic microwave background. *The Astrophysical Journal* **707**, 916 (2009).

[74] Longair, M. S. *High Energy Astrophysics* (Cambridge University Press, 2010).

[75] Verzi, V., Ivanov, D. & Tsunesada, Y. Measurement of energy spectrum of ultra-high energy cosmic rays. *Progress of Theoretical and Experimental Physics* **2017**, 12A103 (2017).

[76] Abu-Zayyad, T. *et al.* The cosmic-ray energy spectrum observed with the surface detector of the Telescope Array experiment. *The Astrophysical Journal Letters* **768**, L1 (2013).

[77] Abu-Zayyad, T. *et al.* The energy spectrum of ultra-high-energy cosmic rays measured by the Telescope Array FADC fluorescence detectors in monocular mode. *Astroparticle Physics* **48**, 16–24 (2013).

[78] Watson, A. High-energy cosmic rays and the Greisen–Zatsepin–Kuz'min effect. *Reports on Progress in Physics* **77**, 036901 (2014).

[79] Kampert, K.-H. & Tinyakov, P. Cosmic rays from the ankle to the cutoff. *Comptes Rendus Physique* **15**, 318–328 (2014).

[80] Aharonian, F. *et al.* First ground-based measurement of atmospheric Cherenkov light from cosmic rays. *Physical Review D* **75**, 042004 (2007).

[81] Chiarusi, T. & ANTARES Collaboration. Neutrino astrophysics with the ANTARES Cherenkov Detector. In *Journal of Physics Conference Series*, vol. 409 of *Journal of Physics Conference Series*, 012133 (2013).

[82] Allekotte, I. *et al.* The surface detector system of the Pierre Auger Observatory. *Nuclear Instruments and Methods in Physics Research Section A: Accelerators, Spectrometers, Detectors and Associated Equipment* **586**, 409–420 (2008).

[83] Čerenkov, P. A. Visible radiation produced by electrons moving in a medium with velocities exceeding that of light. *Physical Review* **52**, 378–379 (1937).

[84] Tamm, I. & Frank, I. Coherent radiation of fast electrons in a medium. In *Dokl. Akad. Nauk SSSR*, vol. 14, 107–112 (1937).

[85] Kalashev, O. E., Kuzmin, V. A. & Semikoz, D. V. Top-Down Models and Extremely High Energy Cosmic Rays. *arXiv e-prints* astro–ph/9911035 (1999).

[86] Mbarek, R. & Caprioli, D. Bottom-up acceleration of ultra-high-energy cosmic rays in the jets of active Galactic nuclei. *The Astrophysical Journal* **886**, 8 (2019).

[87] Fermi, E. On the origin of the cosmic radiation. *Physical Review* **75**, 1169–1174 (1949).

[88] Gaisser, T. K., Engel, R. & Resconi, E. *Cosmic Rays and Particle Physics* (Cambridge University Press, 2016).

[89] Grupen, C., Cowan, G., Eidelman, S. & Stroh, T. *Astroparticle Physics*, vol. 50 (Springer, 2005).

[90] Ellison, D. C. *et al.* Supernova remnants and the physics of strong shock waves. *Publications of the Astronomical Society of the Pacific* **106**, 780 (1994).

[91] Bell, A. The acceleration of cosmic rays in shock fronts – i. *Monthly Notices of the Royal Astronomical Society* **182**, 147–156 (1978).

[92] Linsley, J., Scarsi, L. & Rossi, B. Extremely energetic cosmic-ray event. *Physical Review Letters* **6**, 485 (1961).

[93] Tennent, R. The Haverah Park extensive air shower array. *Proceedings of the Physical Society (1958-1967)* **92**, 622 (1967).

[94] Bell, C. J. *et al.* The upper end of the observed cosmic ray energy spectrum. *Journal of Physics A: Mathematical, Nuclear and General* **7**, 990 (1974).

[95] Chiba, N. *et al.* Akeno Giant Air Shower Array (AGASA) covering 100 km^2 area. *Nuclear Instruments and Methods in Physics Research Section A: Accelerators, Spectrometers, Detectors and Associated Equipment* **311**, 338–349 (1992).

[96] Shinozaki, K., Teshima, M., Collaboration, A. *et al.* AGASA results. *Nuclear Physics B-Proceedings Supplements* **136**, 18–27 (2004).

[97] Baltrusaitis, R. *et al.* The Utah Fly's eye detector. *Nuclear Instruments and Methods in Physics Research Section A: accelerators, spectrometers, detectors and associated equipment* **240**, 410–428 (1985).

[98] Thomson, G. New results from the HiRes experiment. *Nuclear Physics B-Proceedings Supplements* **136**, 28–33 (2004).

[99] High Resolution Fly's Eye Collaboration *et al.* First observation of the Greisen-Zatsepin-Kuzmin suppression. *Physical Review Letters* **100**, 101101 (2008).

[100] Kawai, H. *et al.* Telescope Array Experiment. *Nuclear Physics B (Proceedings Supplements)* 221–226 (2008).

[101] Ogio, S. & Telescope Array Collaboration. Telescope Array Low energy Extension: TALE. In *Proceedings of 2016 International Conference on Ultra-High Energy Cosmic Rays UHECR2016* (2018).

[102] Sánchez, F. The AMIGA detector of the Pierre Auger Observatory: an overview. In *32nd International Cosmic Ray Conference*, vol. 3, 149–152 (2011).

[103] Aab, A. *et al.* Spectral calibration of the fluorescence telescopes of the Pierre Auger Observatory. *Astroparticle Physics* **95**, 44–56 (2017).

[104] Abraham, J. *et al.* Trigger and aperture of the surface detector array of the Pierre Auger Observatory. *Nuclear Instruments and Methods in Physics Research Section A: Accelerators, Spectrometers, Detectors and Associated Equipment* **613**, 29–39 (2010).

[105] Bertou, X. *et al.* Calibration of the surface array of the Pierre Auger Observatory. *Nuclear Instruments and Methods in Physics Research Section A: Accelerators, Spectrometers, Detectors and Associated Equipment* **568**, 839–846 (2006).

[106] Aab, A. *et al.* Reconstruction of events recorded with the surface detector of the Pierre Auger Observatory. *Journal of Instrumentation* **15**, P10021 (2020).

[107] Abraham, J. *et al.* The fluorescence detector of the Pierre Auger Observatory. *Nuclear Instruments and Methods in Physics Research Section A: Accelerators, Spectrometers, Detectors and Associated Equipment* **620**, 227–251 (2010).

[108] Wundheiler, B. for the Pierre Auger Collaboration. The AMIGA muon counters of the Pierre Auger Observatory: performance and studies of the lateral distribution function. In *The 34th International Cosmic Ray Conference*, vol. 236, 324 (SISSA Medialab, 2016).

[109] The Pierre Auger Collaboration. Design and implementation of the AMIGA embedded system for data acquisition. *Journal of Instrumentation* **16**, T07008 (2021).

[110] Mathes, T. Hermann-Josef for the Pierre Auger Collaboration. The HEAT telescopes of the Pierre Auger Observatory: Status and First Data. *Proceedings of the 32nd ICRC, Beijing, China* 153–156 (2011).

[111] Holt, E. M. for the Pierre Auger Collaboration. Recent results of the Auger Engineering Radio Array (AERA). In *35th International Cosmic Ray Conference (ICRC2017)*, vol. 301, 492 (2017).

[112] Bassi, P., Clark, G. & Rossi, B. Distribution of arrival times of air shower particles. *Physical Review* **92**, 441–451 (1953).

[113] Hersil, J., Escobar, I., Scott, D., Clark, G. & Olbert, S. Observations of extensive air showers near the maximum of their longitudinal development. *Physical Review Letters* **6**, 22–23 (1961).

[114] The Pierre Auger Collaboration. Reconstruction of inclined air showers detected with the Pierre Auger Observatory. *Journal of Cosmology and Astroparticle Physics* **2014**, 019 (2014).

[115] Dembinski, H., Billoir, P., Deligny, O. & Hebbeker, T. A phenomenological model of the muon density profile on the ground of very inclined air showers. *Astroparticle Physics* **34**, 128–138 (2010).

[116] Anastasi, G. A. & The Pierre Auger Collaboration. AugerPrime: The Pierre Auger Observatory upgrade. *Nuclear Instruments and Methods in Physics Research Section A: Accelerators, Spectrometers, Detectors and Associated Equipment* **1044**, 167497 (2022).

[117] Alvarez-Muniz, J. *et al.* Muon production and string percolation effects in cosmic rays at the highest energies. *arXiv* (2012). arXiv:1209.6474[hep-ph].

[118] Farrar, G. R. & Allen, J. D. A new physical phenomenon in ultra-high energy collisions. In *EPJ Web of Conferences*, vol. 53, 07007 (EDP Sciences, 2013).

[119] Anchordoqui, L. A., Goldberg, H. & Weiler, T. J. Strange fireball as an explanation of the muon excess in Auger data. *Physical Review D* **95**, 063005 (2017).

[120] Anchordoqui, L. A., Canal, C. G., Kling, F., Sciutto, S. J. & Soriano, J. F. An explanation of the muon puzzle of ultrahigh-energy cosmic rays and the role of the Forward Physics Facility for model improvement. *Journal of High Energy Astrophysics* **34**, 19–32 (2022).

[121] Rutherford, E. The scattering of α and β particles by matter and the structure of the atom. *Philosophical Magazine* **21**, 669–688 (1911).

[122] Van den Broek, A. The number of possible elements and Mendeléff's "cubic" periodic system. *Nature* **87**, 78 (1911).

[123] Aston, F. Neon. *Nature* **104**, 334 (1919).

[124] Chadwick, J. The existence of a neutron. *Proceedings of the Royal Society of London. Series A, Containing Papers of a Mathematical and Physical Character* **136**, 692–708 (1932).

[125] The Nobel Prize in Physics 1935. URL https://www.nobelprize.org/prizes/physics/1935/summary/.

[126] Thomson, M. *Modern Particle Physics* (Cambridge University Press, 2013).

[127] Snell, A. H. & Miller, L. C. *On the radioactive decay of the neutron* (US Atomic Energy Commission, Technical Information Division, 1948).

[128] Leung, H. W. *et al.* A measurement of the distance to the Galactic centre using the kinematics of bar stars. *Monthly Notices of the Royal Astronomical Society* **519**, 948–960 (2023).

[129] Medina-Tanco, G. A. & Watson, A. A. On the possible galactic sources of the ultra-high energy cosmic ray anisotropy at 1 EeV. In *27th International Cosmic Ray Conference*, vol. 2 of *Proceedings of the 27th International Cosmic Ray Conference*, 531 (2001).

[130] Crocker, R. M., Fatuzzo, M., Jokipii, J., Melia, F. & Volkas, R. R. The AGASA and SUGAR anisotropies and TeV gamma rays from the Galactic center: A possible signature of extremely high energy neutrons. *The Astrophysical Journal* **622**, 892 (2005).

[131] Gorski, K. M. *et al.* Healpix: A framework for high-resolution discretization and fast analysis of data distributed on the sphere. *The Astrophysical Journal* **622**, 759 (2005).

[132] Welcome to the healpy documentation. URL https://healpy.readthedocs.io.

[133] Cassiday, G. *et al.* Mapping the UHE sky in search of point sources. *Nuclear Physics B-Proceedings Supplements* **14**, 291–298 (1990).

[134] Li, T.-P. & Ma, Y.-Q. Analysis methods for results in gamma-ray astronomy. *The Astrophysical Journal* **272**, 317–324 (1983).

[135] Zech, G. Upper limits in experiments with background or measurement errors. *Nuclear Instruments and Methods in Physics Research Section A: Accelerators, Spectrometers, Detectors and Associated Equipment* **277**, 608–610 (1989).

[136] (H.E.S.S. Collaboration), Hinton, J. A. The status of the H.E.S.S. project. *New Astronomy Reviews* **48**, 331–337 (2004). 2nd VERITAS Symposium on the Astrophysics of Extragalactic Sources.

[137] (H.E.S.S. Collaboration) *et al.* Observations of the Crab nebula with H.E.S.S. *Astronomy & Astrophysics* **457**, 899–915 (2006).

[138] Ashton, T. *et al.* A NECTAr-based upgrade for the Cherenkov cameras of the H.E.S.S. 12-meter telescopes. *Astroparticle Physics* **118**, 102425 (2020).

[139] Lorimer, D. R. & Kramer, M. *Handbook of Pulsar Astronomy*, vol. 4 (2004).

[140] Hewish, A., Bell, S., Pilkington, J., Scott, P. & Collins, R. Nature, 217, 709. *Observation of a Rapidly Pulsating Radio Source* (1968).

[141] Backer, D. C., Kulkarni, S. R., Heiles, C., Davis, M. & Goss, W. A millisecond pulsar. *Nature* **300**, 615–618 (1982).

[142] ATNF pulsar catalogue. URL https://www.atnf.csiro.au/research/pulsar/psrcat/.

[143] Manchester, R. N., Hobbs, G. B., Teoh, A. & Hobbs, M. The Australia Telescope National Facility Pulsar Catalogue. *The Astronomical Journal* **129**, 1993 (2005).

[144] Kniffen, D. *et al.* Gamma radiation from the Crab Nebula above 35 MeV. *Nature* **251**, 397–399 (1974).

[145] Abdo, A. A. *et al.* The Second Fermi Large Area Telescope Catalog of Gamma-ray Pulsars. *The Astrophysical Journal Supplement Series* **208**, 17 (2013).

[146] Tananbaum, H. D. UHURU results on Galactic X-ray sources. In *X-and Gamma-Ray Astronomy*, 9–28 (Springer, 1973).

[147] LMXBCAT - Low-Mass X-ray Binary Catalog (4th Edition, 2007). URL https://heasarc.gsfc.nasa.gov/W3Browse/star-catalog/lmxbcat.html.

[148] Liu, Q., Van Paradijs, J. & Van Den Heuvel, E. A catalogue of low-mass X-ray binaries in the Galaxy, LMC, and SMC. *Astronomy & Astrophysics* **469**, 807–810 (2007).

[149] HMXBCAT - Catalog of High-Mass X-Ray Binaries in the Galaxy (4th Ed.). URL https://heasarc.gsfc.nasa.gov/W3Browse/star-catalog/hmxbcat.html.

[150] Liu, Q. Z., van Paradijs, J. & van den Heuvel, E. P. J. Catalogue of high-mass X-ray binaries in the Galaxy (4th Edition). *Astronomy & Astrophysics* **455**, 1165–1168 (2006).

[151] Mirabel, I. F. & Rodríguez, L. F. Microquasars in our galaxy. *Nature* **392**, 673–676 (1998).

[152] Chaty, S. Microquasars. URL http://www.aim.univ-paris7.fr/CHATY.

[153] Duncan, R. C. & Thompson, C. Formation of very strongly magnetized neutron stars – implications for gamma-ray bursts. *The Astrophysical Journal* **392**, L9–L13 (1992).

[154] Mereghetti, S., Pons, J. A. & Melatos, A. Magnetars: properties, origin and evolution. *Space Science Reviews* **191**, 315–338 (2015).

[155] Abuter, R. *et al.* A geometric distance measurement to the Galactic center black hole with 0.3% uncertainty. *Astronomy & Astrophysics* **625**, L10 (2019).

[156] Good, I. On the weighted combination of significance tests. *Journal of the Royal Statistical Society: Series B (Methodological)* **17**, 264–265 (1955).

APPENDIX A - COORDINATE SYSTEMS

In this work, we present methods to search for point sources of neutrons, i.e., a study of the angular distribution of the arrival directions of ultra-high-energy cosmic rays. To properly understand the analysis presented in this thesis, it is important to understand the coordinate systems used. In this appendix, we describe the coordinate systems in this thesis.

A.1 Local system

The local coordinate system is the one placed at the Observatory. The two angles used are the zenith (θ) and the azimuth (φ) angle. Since the Earth is rotating, the system is rotating together, and to define a unique direction in the sky, we also need to register the observation time. The z-axis points in the direction of the zenith of the Observatory. The x-axis direction points East, and the y-axis points North. The zenith angle is measured from the z-axis and the azimuth angle from the x-axis. We show a scheme of the local coordinate system in Figure A.1.

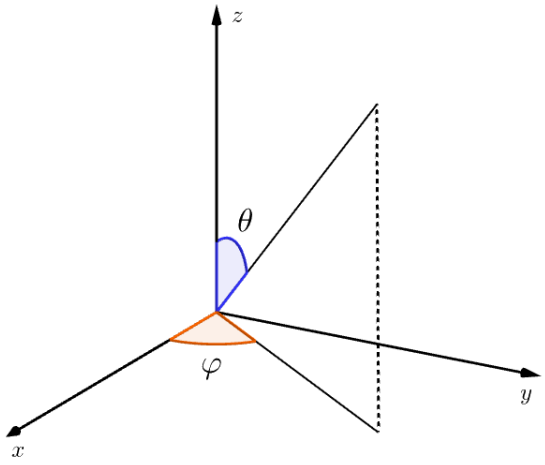

Figure A.1: The local coordinate system.

A.2 Equatorial coordinate system

In the equatorial coordinates system, the two angles are the right ascension α and the declination δ (Figure A.2). The fundamental plane in the equatorial system is the projection of Earth's equatorial plane onto the celestial sphere often called the celestial equatorial plane.

The right ascension is the angular distance measured eastward along the celestial equator from the first point of Aries. The first point of Aries is the position where the Sun is during the March equinox in the celestial equatorial plane, throughout its passage from the celestial southern hemisphere to the celestial northern hemisphere. The declination is the angular distance measured from the celestial equatorial plane. The right ascension varies between 0 and 360°, and the declination between −90° (South Pole) and +90° (North Pole). Due to the fact that the fundamental plane and the first point of Aries are relatively fixed with respect to the background stars, a position defined by the coordinates (α, δ) is unique.

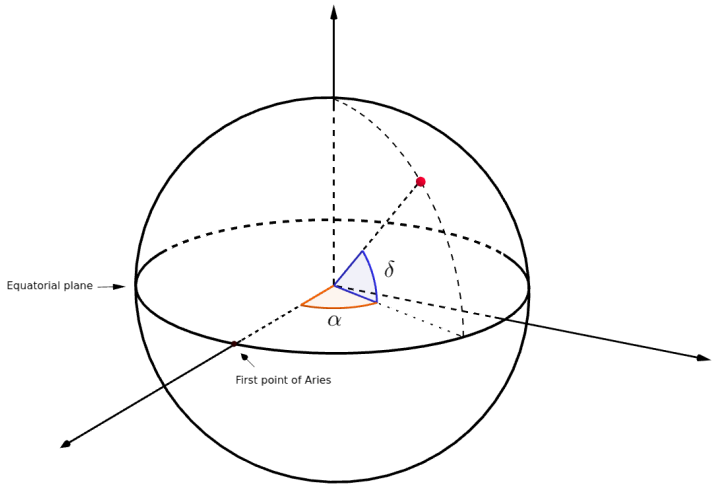

Figure A.2: The equatorial coordinate system.

A.3 Galactic coordinate system

The Galactic coordinates system uses two angles to establish a direction in the sky: the Galactic latitude, commonly represented by the symbol b[1], and the Galactic longitude, usually represented by the symbol ℓ. The fundamental plane is the Galactic plane. The Galactic latitude is the angular distance measured from the Galactic plane and it is in the range $-90° \leq b \leq +90°$. The Galactic longitude is the angular distance measured along the Galactic plane from the Galactic center in the range $-180° \leq \ell \leq +180°$. In Figure A.3, we show a representation of the Galactic coordinate system.

[1]Throughout this work, we used the Greek letter β to represent the Galactic latitude to distinguish from the expected number of events within a target region, represented by the letter b.

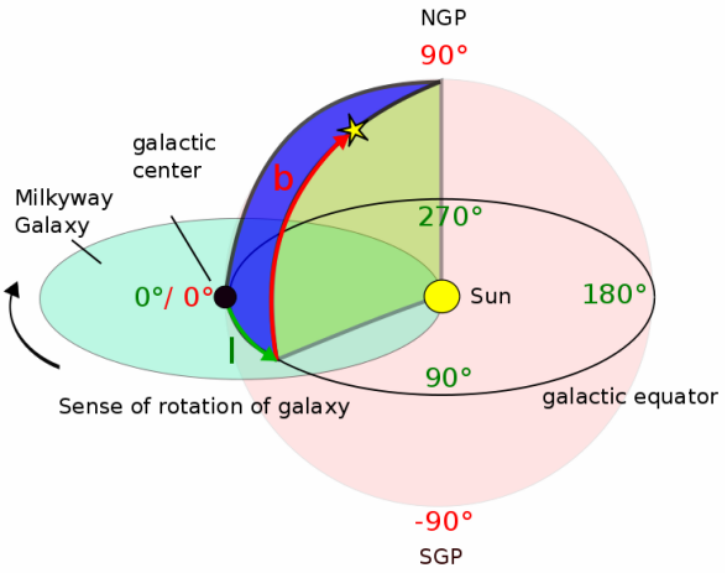

Figure A.3: The Galactic coordinate system. Figure extracted from https://auger.org/education/Auger_Education/galacticcoordinates.html.

APPENDIX B - SOME MATHEMATICAL DETAILS

B.1 Angular uncertainty derivation

In this section, we discuss the details of the derivation of the Equation 6.3. The reconstructed direction Ω of an event slightly differs from the true direction Ω_0. Therefore, we can write Ω as

$$\Omega = \Omega_0 + \Delta\Omega. \tag{B.1}$$

The angle between Ω and Ω_0, η, can be approximate as

$$\eta \approx \sin\eta = \|\Omega_0 \times \Omega\| = \|\Omega_0 \times \Delta\Omega\|. \tag{B.2}$$

We can write $\Delta\Omega$ in terms of the angular uncertainties in local coordinates $\Delta\theta$ and $\Delta\varphi$, corresponding to the uncertainties in the zenith and in the azimuth angle, respectively, as

$$\Delta\Omega = \Delta\theta\hat{\theta} + \sin\theta_0\Delta\varphi\hat{\varphi}. \tag{B.3}$$

Therefore, the cross product in Equation B.2 can be written as

$$\Omega_0 \times \Delta\Omega = \hat{r} \times (\Delta\theta\hat{\theta} + \sin\theta_0\Delta\varphi\hat{\varphi}) = \Delta\theta\hat{\varphi} - \sin\theta_0\Delta\varphi\hat{\theta}. \tag{B.4}$$

Replacing in Equation B.2, we obtain

$$\eta^2 = \|\Omega_0 \times \Delta\Omega\| = \Delta\theta^2 + \sin^2\theta_0\Delta\varphi^2. \tag{B.5}$$

The transformation between the local coordinates (θ,φ) to the planar coordinates (u,v) is the following:

$$\sin\theta = \sqrt{u^2+v^2} \tag{B.6}$$

$$\tan\varphi = \frac{v}{u}. \tag{B.7}$$

Expanding in first order the uncertainties $\Delta\theta$ and $\Delta\varphi$ and writing in terms of the fluctuations

in u and v, Δu and Δv, we obtain

$$\Delta\theta = \left(\frac{\partial\theta}{\partial u}\Delta u + \frac{\partial\theta}{\partial v}\Delta v\right)\Big|_{(u_0,v_0)} = \frac{u_0}{\sqrt{u_0^2+v_0^2}}\Delta u + \frac{v_0}{\sqrt{u_0^2+v_0^2}}\Delta v \tag{B.8}$$

$$\implies \Delta\theta = \frac{1}{\sin\theta_0}(u_0\Delta u + v_0\Delta v) \tag{B.9}$$

and

$$\Delta\varphi = \left(\frac{\partial\varphi}{\partial u}\Delta u + \frac{\partial\varphi}{\partial v}\Delta v\right)\Big|_{(u_0,v_0)} = -\frac{v_0}{u_0^2+v_0^2}\Delta u + \frac{u_0}{u_0^2+v_0^2}\Delta v \tag{B.10}$$

$$\implies \sin\theta_0\Delta\varphi = \frac{1}{\sin\theta_0}(-v_0\Delta u + u_0\Delta v). \tag{B.11}$$

Replacing Equations B.9 and B.11 in Equation B.5, we obtain

$$\eta^2 = \Delta\theta^2 + \sin^2\theta_0\Delta\varphi^2 = \Delta u^2 + \Delta v^2. \tag{B.12}$$

Assuming that the fluctuations Δu and Δv follow a Gaussian distribution with mean zero and the same standard deviation σ, we can normalize them by σ to obtain two standard normal variables[1],

$$\frac{\eta^2}{\sigma^2} = \frac{\Delta u^2}{\sigma^2} + \frac{\Delta v^2}{\sigma^2}. \tag{B.13}$$

Taking the expected value of Equation B.12, we obtain

$$\mathrm{E}[\Delta\theta^2] + \mathrm{E}[\Delta\varphi^2\sin^2\theta_0] = \mathrm{E}[\Delta\theta^2] + \mathrm{E}[\Delta\varphi^2]\sin^2\theta_0 = \mathrm{E}[\Delta u^2] + \mathrm{E}[\Delta v^2]. \tag{B.14}$$

Since the mean of all variables is zero, their expected value is equal to their variance,

$$\mathrm{Var}[\Delta\theta] + \mathrm{Var}[\Delta\varphi]\sin^2\theta_0 = \mathrm{Var}[\Delta u] + \mathrm{Var}[\Delta v] = 2\sigma^2 \tag{B.15}$$

$$\implies \sigma = \sqrt{\frac{\mathrm{Var}[\theta] + \sin^2\theta_0\mathrm{Var}[\varphi]}{2}} = \sqrt{\frac{\Delta\theta^2 + \sin^2\theta_0\Delta\varphi^2}{2}}. \tag{B.16}$$

B.2 Combined *p*-value

In this section, we are going to discuss some details about the derivation of Equation 8.6. The probability density function (PDF) of the product of m independent and identically uni-

[1] A standard normal random variable is a normally distributed random variable with mean $\mu = 0$ and standard deviation $\sigma = 1$.

formly distributed random variables is given by

$$f_{Z_m}(z) = \frac{(-\ln z)^{m-1}}{(m-1)!} \quad \text{(with } 0 \le z \le 1\text{)}, \tag{B.17}$$

resulting in cumulative distribution function (CDF) given by

$$\Pr[Z_{m+1} \le z] = z \sum_{j=0}^{m} \frac{(-\ln z)^j}{j!}. \tag{B.18}$$

We can demonstrate this result via induction. Let us start with two independent and identically uniformly distributed random variables in the interval between 0 and 1, X_1 and X_2. The CDF of the product $Z_2 = X_1 \cdot X_2$ is given by

$$F_{Z_2}(z) = \Pr[Z_2 \le z] = \int_0^1 \Pr\left[X_2 \le \frac{z}{x}\right] f_{X_1}(x)\,dx, \tag{B.19}$$

where

$$\Pr\left[X_2 \le z/x\right] = \begin{cases} \frac{z}{x}, & \text{if } x \ge z \\ 1, & \text{otherwise.} \end{cases} \tag{B.20}$$

Replacing Equation B.20 in Equation B.19, we obtain the following CDF:

$$F_{Z_2}(z) = \int_0^z dx + \int_z^1 \frac{z}{x}\,dx = z - z\ln z. \tag{B.21}$$

Therefore, the PDF is given by

$$f_{Z_2}(z) = -\ln z. \tag{B.22}$$

For the product of three independent and identically uniformly distributed random variables, X_1, X_2, and X_3, it is easy to verify that Equations B.17 and B.18 are satisfied. The CDF of the product $Z_3 = X_1 \cdot X_2 \cdot X_3$ is given by:

$$\begin{aligned} F_{Z_3}(z) = \Pr[Z_3 \le z] &= \int_0^1 \Pr\left[X_3 \le \frac{z}{x}\right] f_{Z_2}(x)\,dx \\ &= \int_0^z (-\ln x)\,dx + \int_z^1 \frac{z}{x}(-\ln x)\,dx = z - z\ln z + z\frac{\ln^2 z}{2}. \end{aligned} \tag{B.23}$$

Therefore, the PDF is given by

$$f_{Z_3}(z) = \frac{\ln^2 z}{2}. \tag{B.24}$$

Let us assume that Equation B.18 is true for k. Then, the PDF is

$$f_{Z_k}(z) = \frac{(-\ln z)^{k-1}}{(k-1)!}, \tag{B.25}$$

and the CDF for $k+1$ is given by

$$\begin{aligned} F_{Z_{k+1}}(z) = \Pr[Z_{k+1} \leq z] &= \int_0^1 \Pr\left[X_{k+1} \leq \frac{z}{x}\right] f_{Z_k}(x)\,dx \\ &= \int_0^z \frac{(-\ln x)^{k-1}}{(k-1)!}\,dx + \int_z^1 \frac{z}{x}\frac{(-\ln x)^{k-1}}{(k-1)!}\,dx. \end{aligned} \tag{B.26}$$

To solve Equation B.26, we need the result of the following integral:

$$I = \int (\ln x)^m\,dx. \tag{B.27}$$

We can solve this integral by doing an integration by parts using

$$u = (\ln x)^m \implies du = (m/x)(\ln x)^{m-1}dx \text{ and } dv = dx \implies v = x:$$

$$\begin{aligned} I &= x(\ln x)^m - m\int (\ln x)^{m-1}dx = x(\ln x)^m - mx(\ln x)^{m-1} + m(m-1)\int (\ln x)^{m-2}dx \\ &= (-1)^m x \sum_{j=0}^{m} m!\frac{(-\ln x)^j}{j!} \end{aligned} \tag{B.28}$$

Using this result in Equation B.26, we obtain

$$\begin{aligned} F_{Z_{k+1}}(z) &= \frac{(-1)^{2(k-1)}}{(k-1)!}x\sum_{j=0}^{k-1}(k-1)!\frac{(-\ln x)^j}{j!}\bigg|_0^z + \frac{(-1)^{k-1}z}{(k-1)!}\frac{(\ln x)^k}{k}\bigg|_z^1 \\ &= z\sum_{j=0}^{k-1}\frac{(-\ln z)^j}{j!} + \frac{z(-\ln z)^k}{k!} = z\sum_{j=0}^{k}\frac{(-\ln z)^j}{j!}, \end{aligned} \tag{B.29}$$

leading to

$$\Pr(Z_{k+1} \leq z) = z\sum_{j=0}^{k}\frac{(-\ln z)^j}{j!}. \tag{B.30}$$

To demonstrate the last step of Equation 8.6, we use the fact that Poisson(n,b) represents the probability of getting n or more events in the presence of a background fol-

lowing a Poisson distribution with mean b, implying that we can write

$$\text{Poisson}(n,b) = \sum_{j=n}^{\infty} f_p(j,b) = 1 - \sum_{j=0}^{n-1} f_p(j,b) = 1 - \sum_{j=0}^{n-1} \frac{b^j e^{-b}}{j!}. \tag{B.31}$$

Therefore, we can write

$$\text{Poisson}(N,-\ln\Pi_0) = 1 - \sum_{j=0}^{N-1} \frac{(-\ln\Pi_0)^j e^{-(-\ln\Pi_0)}}{j!} = 1 - \Pi_0 \sum_{j=0}^{N-1} \frac{(-\ln\Pi_0)^j}{j!}. \tag{B.32}$$

Reorganizing the terms, we obtain

$$\Pi_0 \sum_{j=0}^{N-1} \frac{(-\ln\Pi_0)^j}{j!} = 1 - \text{Poisson}(N,-\ln\Pi_0). \tag{B.33}$$

APPENDIX C - ADDITIONAL RESULTS: TARGETED SEARCH IN A WELL-DEFINED REGION

Since we did not identify any clear evidence of a neutron flux coming from any of the tested targets, we reported the results for the cumulative data sets[1] in Chapter 9, and we present the results for the other energy ranges in this appendix.

C.1 Vertical data set

In this section, we report the additional results for the vertical data set.

C.1.1 The most significant target in each target set

The tables C.1, C.2, and C.3 present the results for the most significant target in each target set for the vertical data set. The most significant target is the one with the smallest individual p-value. The tables show the position of the candidate source, the observed and expected number of events inside the target region, and the upper limit on the flux of neutrons and on the energy flux, in addition to the p-value and the penalized p-value.

[1] Cumulative data sets are the ones with events above 1 EeV for the vertical and inclined data sets and 0.1 EeV for the infill data set.

Table C.1: Results for the most significant target in each target set for the vertical data set and events with energy between 1 and 2 EeV.

Results for the targeted search - vertical data set - 1 EeV $< E \leq$ 2 EeV								
Class	**RA [deg]**	**Dec [deg]**	**Observed**	**Expected**	**Flux U.L.** $[\mathrm{km^{-2}\ yr^{-1}}]$	**E-flux U.L.** $[\mathrm{eV\ cm^{-2}\ s^{-1}}]$	p**-value**	p**-value (penalized)**
msec PSRs	283.11	−0.73	338	290	0.016	0.12	0.0029	0.34
γ-ray PSRs	271.43	6.26	230	191	0.017	0.13	0.0030	0.40
LMXB	257.55	−28.13	685	632	0.013	0.095	0.018	0.83
HMXB	195.32	−61.60	660	603	0.011	0.083	0.011	0.44
H.E.S.S. PWN	98.16	−17.37	550	520	0.011	0.078	0.095	0.67
H.E.S.S. other	288.40	4.93	225	209	0.011	0.080	0.13	0.89
H.E.S.S. UNID	286.79	8.50	185	163	0.014	0.10	0.045	0.72
Microquasars	287.96	4.98	231	209	0.012	0.091	0.066	0.59
Magnetars	237.73	−54.31	698	662	0.0095	0.069	0.082	0.88
Gal. Center	266.42	−29.01	577	640	0.0031	0.023	0.99	0.99

Table C.2: Results for the most significant target in each target set for the vertical data set and events with energy between 2 and 3 EeV.

Results for the targeted search - vertical data set - 2 EeV $< E \leq$ 3 EeV								
Class	**RA [deg]**	**Dec [deg]**	**Observed**	**Expected**	**Flux U.L.** $[\mathrm{km^{-2}\ yr^{-1}}]$	**E-flux U.L.** $[\mathrm{eV\ cm^{-2}\ s^{-1}}]$	p**-value**	p**-value (penalized)**
msec PSRs	286.70	0.92	38	24	0.0048	0.035	0.0040	0.43
γ-ray PSRs	284.39	1.73	41	23	0.0059	0.043	0.00034	0.056
LMXB	194.41	−69.29	61	45	0.0031	0.023	0.011	0.66
HMXB	98.83	5.55	29	18	0.0049	0.036	0.0081	0.35
H.E.S.S. PWN	279.41	−6.95	41	33	0.0033	0.024	0.086	0.63
H.E.S.S. other	282.12	−1.79	35	27	0.0035	0.026	0.067	0.65
H.E.S.S. UNID	284.40	2.97	34	21	0.0051	0.037	0.0044	0.12
Microquasars	262.75	−26.00	62	55	0.0027	0.020	0.17	0.91
Magnetars	245.69	−49.85	75	60	0.0033	0.024	0.030	0.53
Gal. Center	266.42	−29.01	62	57	0.0024	0.018	0.25	0.25

Table C.3: Results for the most significant target in each target set for the vertical data set and events with energy above 3 EeV.

Results for the targeted search - vertical data set - $E \geq 3$ EeV								
Class	**RA [deg]**	**Dec [deg]**	**Observed**	**Expected**	**Flux U.L.** [$\mathrm{km^{-2}\ yr^{-1}}$]	**E-flux U.L.** [$\mathrm{eV\ cm^{-2}\ s^{-1}}$]	p**-value**	p**-value (penalized)**
msec PSRs	327.50	−3.00	18	9	0.0033	0.024	0.0039	0.42
γ-ray PSRs	266.73	−32.67	29	18	0.0028	0.020	0.0081	0.75
LMXB	273.78	−12.10	21	12	0.0031	0.022	0.0088	0.57
HMXB	98.83	5.55	12	6	0.0031	0.023	0.014	0.53
H.E.S.S. PWN	84.43	−69.17	17	14	0.0013	0.0094	0.21	0.92
H.E.S.S. other	287.78	9.09	7	4	0.0030	0.022	0.081	0.72
H.E.S.S. UNID	280.95	−3.55	15	9	0.0028	0.020	0.032	0.59
Microquasars	237.50	−56.07	24	18	0.0017	0.013	0.085	0.68
Magnetars	286.81	9.32	8	4	0.0033	0.024	0.036	0.60
Gal. Center	266.42	−29.01	18	18	0.0014	0.010	0.48	0.48

C.1.2 Analysis combining targets

The results for the combined analysis are presented in Tables C.4, C.5, and C.6.

Table C.4: Results for the combined analysis for the vertical data set with events between 1 and 2 EeV.

Results for combined analysis - Vertical data set - 1 EeV $< E \leq$ 2 EeV			
Class	**Number of targets**	***P*-value (unweighted)**	***P*-value (weighted)**
msec PSRs	142	0.95	0.68
γ-ray PSRs	168	0.95	0.025
LMXB	95	0.75	0.46
HMXB	52	0.95	0.44
H.E.S.S. PWN	11	0.79	0.56
H.E.S.S. other	15	0.50	0.84
H.E.S.S. UNID	28	0.99	1.0
Microquasars	13	0.46	0.55
Magnetars	25	0.98	0.94
Gal. Center	1	0.99	0.99

Table C.5: Results for the combined analysis for the vertical data set with events between 2 and 3 EeV.

Results for combined analysis - Vertical data set - 2 EeV $< E \leq$ 3 EeV			
Class	**Number of targets**	***P*-value (unweighted)**	***P*-value (weighted)**
msec PSRs	142	0.11	0.22
γ-ray PSRs	168	0.56	0.95
LMXB	95	0.060	0.020
HMXB	52	0.43	0.82
H.E.S.S. PWN	11	0.59	0.075
H.E.S.S. other	15	0.37	0.69
H.E.S.S. UNID	28	0.18	0.44
Microquasars	13	0.74	0.52
Magnetars	25	0.66	0.94
Gal. Center	1	0.25	0.25

Table C.6: Results for the combined analysis for the vertical data set with events above 3 EeV.

Results for combined analysis - Vertical data set - $E \geq 3$ EeV			
Class	**Number of targets**	**P-value (unweighted)**	**P-value (weighted)**
msec PSRs	142	0.18	0.67
γ-ray PSRs	168	0.53	0.91
LMXB	95	0.90	0.76
HMXB	52	0.71	0.67
H.E.S.S. PWN	11	0.75	0.55
H.E.S.S. other	15	0.11	0.47
H.E.S.S. UNID	28	0.046	0.066
Microquasars	13	0.75	0.34
Magnetars	25	0.59	0.52
Gal. Center	1	0.48	0.49

C.2 Inclined data set

In this section, we present the results for the inclined data set.

C.2.1 The most significant target in each target set

We report in Tables C.7, C.8, and C.9 the results for the most significant target in each target set for the inclined data set.

Table C.7: Results for the most significant target in each target set for the inclined data set and events with energy between 1 and 2 EeV.

Results for the targeted search - inclined data set - 1 EeV $< E \leq$ 2 EeV								
Class	**RA [deg]**	**Dec [deg]**	**Observed**	**Expected**	**Flux U.L.** $[\mathrm{km^{-2}\ yr^{-1}}]$	**E-flux U.L.** $[\mathrm{eV\ cm^{-2}\ s^{-1}}]$	p**-value**	p**-value (penalized)**
msec PSRs	270.36	−32.18	12	4	0.055	0.40	0.00059	0.099
γ-ray PSRs	262.64	−33.84	11	4	0.051	0.37	0.0019	0.30
LMXB	267.60	−29.04	9	4	0.043	0.31	0.015	0.77
HMXB	195.49	−63.97	22	13	0.022	0.16	0.011	0.45
H.E.S.S. PWN	281.60	−2.97	5	4	0.027	0.20	0.29	0.99
H.E.S.S. other	276.56	−14.85	8	5	0.032	0.24	0.10	0.82
H.E.S.S. UNID	281.17	−3.09	9	4	0.046	0.34	0.015	0.39
Microquasars	262.75	−26.00	9	4	0.044	0.32	0.015	0.19
Magnetars	283.19	0.55	7	4	0.037	0.27	0.081	0.89
Gal. Center	266.42	−29.01	5	4	0.025	0.18	0.29	0.29

Table C.8: Results for the most significant target in each target set for the inclined data set and events with energy between 2 and 3 EeV.

Results for the targeted search - inclined data set - 2 EeV $< E \leq$ 3 EeV								
Class	**RA [deg]**	**Dec [deg]**	**Observed**	**Expected**	**Flux U.L.** [km^{-2} yr^{-1}]	**E-flux U.L.** [eV cm^{-2} s^{-1}]	p**-value**	p**-value (penalized)**
msec PSRs	287.72	−59.99	7	3	0.0055	0.040	0.023	0.98
γ-ray PSRs	304.44	−16.24	4	1	0.014	0.10	0.011	0.88
LMXB	236.98	−62.57	10	3	0.0069	0.050	0.00070	0.067
HMXB	275.12	−14.57	3	1	0.011	0.081	0.050	0.94
H.E.S.S. PWN	279.41	−6.95	4	2	0.0064	0.046	0.098	0.74
H.E.S.S. other	287.78	9.09	4	2	0.0062	0.045	0.098	0.81
H.E.S.S. UNID	279.36	−6.58	3	1	0.011	0.081	0.050	0.81
Microquasars	262.75	−26.00	3	1	0.011	0.078	0.050	0.51
Magnetars	162.53	−59.89	7	3	0.0055	0.040	0.023	0.45
Gal. Center	266.42	−29.01	1	2	0.0030	0.022	0.73	0.73

Table C.9: Results for the most significant target in each target set for the inclined data set and events with energy above 3 EeV.

Results for the targeted search - inclined data set - $E \geq 3$ EeV								
Class	**RA [deg]**	**Dec [deg]**	**Observed**	**Expected**	**Flux U.L.** $[\mathrm{km^{-2}\ yr^{-1}}]$	**E-flux U.L.** $[\mathrm{eV\ cm^{-2}\ s^{-1}}]$	p**-value**	p**-value (penalized)**
msec PSRs	269.31	−53.37	5	1	0.0064	0.046	0.0021	0.31
γ-ray PSRs	177.99	−61.14	7	2	0.0037	0.027	0.0028	0.41
LMXB	248.51	−47.39	3	1	0.0045	0.033	0.050	0.99
HMXB	266.19	−27.23	3	1	0.0046	0.033	0.050	0.94
H.E.S.S. PWN	279.41	−6.95	2	1	0.0040	0.029	0.17	0.91
H.E.S.S. other	258.25	−39.75	3	1	0.0045	0.033	0.050	0.56
H.E.S.S. UNID	292.15	17.78	4	1	0.0064	0.047	0.011	0.31
Microquasars	248.50	−47.43	2	1	0.0039	0.028	0.17	0.93
Magnetars	278.43	−8.52	3	1	0.0046	0.034	0.050	0.73
Gal. Center	266.42	−29.01	1	1	0.0033	0.024	0.45	0.45

C.2.2 Analysis combining targets

The results for the combined analysis are presented in Tables C.10, C.11, and C.12.

Table C.10: Results for the combined analysis for the inclined data set with events between 1 and 2 EeV.

Results for combined analysis - Inclined data set - 1 EeV $< E \leq$ 2 EeV			
Class	**Number of targets**	***P*-value (unweighted)**	***P*-value (weighted)**
msec PSRs	175	0.020	0.076
γ-ray PSRs	188	0.36	0.11
LMXB	99	0.45	0.34
HMXB	55	0.54	0.35
H.E.S.S. PWN	13	0.94	0.88
H.E.S.S. other	16	0.98	0.98
H.E.S.S. UNID	33	0.011	0.086
Microquasars	14	0.26	0.96
Magnetars	26	0.88	0.92
Gal. Center	1	0.29	0.29

Table C.11: Results for the combined analysis for the inclined data set with events between 2 and 3 EeV.

Results for combined analysis - Inclined data set - 2 EeV $< E \leq$ 3 EeV			
Class	**Number of targets**	***P*-value (unweighted)**	***P*-value (weighted)**
msec PSRs	175	0.93	0.98
γ-ray PSRs	188	0.61	0.35
LMXB	99	0.48	0.81
HMXB	55	0.77	0.50
H.E.S.S. PWN	13	0.65	0.20
H.E.S.S. other	16	0.97	0.87
H.E.S.S. UNID	33	0.89	0.84
Microquasars	14	0.40	0.43
Magnetars	26	0.67	0.67
Gal. Center	1	0.73	0.73

Table C.12: Results for the combined analysis for the inclined data set with events above 3 EeV.

Results for combined analysis - Inclined data set - $E \geq 3$ EeV			
Class	**Number of targets**	**P-value (unweighted)**	**P-value (weighted)**
msec PSRs	175	0.70	0.94
γ-ray PSRs	188	1.0	0.61
LMXB	99	0.99	0.72
HMXB	55	0.94	0.48
H.E.S.S. PWN	13	0.96	0.40
H.E.S.S. other	16	0.23	0.047
H.E.S.S. UNID	33	0.52	0.37
Microquasars	14	0.97	0.59
Magnetars	26	0.49	0.82
Gal. Center	1	0.45	0.44

C.3 Infill data set

In this section, we report the additional results for the infill data set.

C.3.1 The most significant target in each target set

We report in Tables C.13, C.14, and C.15 the results for the most significant target in each target set for the infill data set.

Table C.13: Results for the most significant target in each target set for the infill data set and events with energy between 0.1 and 0.2 EeV.

Results for the targeted search - infill data set - 0.1 EeV < $E \leq$ 0.2 EeV								
Class	**RA [deg]**	**Dec [deg]**	**Observed**	**Expected**	**Flux U.L.** [$\mathrm{km^{-2}\ yr^{-1}}$]	**E-flux U.L.** [$\mathrm{eV\ cm^{-2}\ s^{-1}}$]	p**-value**	p**-value (penalized)**
msec PSRs	280.76	−14.80	303	265	2.6	19.	0.011	0.63
γ-ray PSRs	274.29	−17.70	337	286	2.9	21.	0.0016	0.20
LMXB	273.63	−17.16	322	282	2.5	19.	0.0097	0.58
HMXB	170.31	−60.62	382	339	2.2	16.	0.011	0.39
H.E.S.S. PWN	169.75	−61.40	386	336	2.5	18.	0.0038	0.041
H.E.S.S. other	259.49	−37.44	406	385	1.6	12.	0.14	0.82
H.E.S.S. UNID	273.34	−12.69	273	250	2.1	15.	0.075	0.71
Microquasars	275.50	−37.02	413	384	1.8	13.	0.071	0.55
Magnetars	162.53	−59.89	376	342	2.0	14.	0.035	0.55
Gal. Center	266.42	−29.01	346	357	0.95	6.9	0.72	0.72

Table C.14: Results for the most significant target in each target set for the infill data set and events with energy between 0.2 and 0.3 EeV.

Results for the targeted search - infill data set - 0.2 EeV < $E \leq$ 0.3 EeV								
Class	**RA [deg]**	**Dec [deg]**	**Observed**	**Expected**	**Flux U.L.** [km^{-2} yr^{-1}]	**E-flux U.L.** [eV cm^{-2} s^{-1}]	p**-value**	p**-value (penalized)**
msec PSRs	284.57	−22.28	52	38	0.68	5.0	0.015	0.74
γ-ray PSRs	285.51	−51.10	63	45	0.67	4.9	0.0054	0.52
LMXB	255.71	−48.79	61	46	0.60	4.4	0.017	0.78
HMXB	283.88	−2.61	36	25	0.83	6.1	0.019	0.57
H.E.S.S. PWN	282.23	−0.04	37	24	0.96	7.0	0.0066	0.070
H.E.S.S. other	81.26	−69.64	61	44	0.68	5.0	0.0074	0.078
H.E.S.S. UNID	250.26	−46.30	54	46	0.47	3.4	0.12	0.87
Microquasars	255.50	−48.00	57	46	0.52	3.8	0.057	0.47
Magnetars	266.42	−29.01	52	42	0.54	4.0	0.066	0.79
Gal. Center	266.42	−29.01	52	42	0.54	4.0	0.066	0.066

Table C.15: Results for the most significant target in each target set for the infill data set and events with energy above 0.3 EeV.

Results for the targeted search - infill data set - $E \geq 0.3$ EeV								
Class	**RA [deg]**	**Dec [deg]**	**Observed**	**Expected**	**Flux U.L.** $[\mathrm{km^{-2}\ yr^{-1}}]$	**E-flux U.L.** $[\mathrm{eV\ cm^{-2}\ s^{-1}}]$	p**-value**	p**-value (penalized)**
msec PSRs	278.93	−32.99	26	17	0.44	3.2	0.020	0.84
γ-ray PSRs	273.35	−12.77	21	12	0.55	4.0	0.0088	0.70
LMXB	256.56	−43.04	30	17	0.52	3.8	0.0021	0.17
HMXB	190.71	−63.06	26	17	0.41	3.0	0.020	0.60
H.E.S.S. PWN	277.85	−9.90	15	11	0.41	3.0	0.12	0.75
H.E.S.S. other	84.00	−67.59	25	17	0.37	2.7	0.033	0.31
H.E.S.S. UNID	273.34	−12.69	20	12	0.52	3.8	0.016	0.23
Microquasars	253.75	−40.00	28	17	0.48	3.5	0.0069	0.073
Magnetars	237.73	−54.31	24	17	0.36	2.6	0.052	0.71
Gal. Center	266.42	−29.01	14	16	0.21	1.5	0.68	0.68

C.3.2 Analysis combining targets

The results for the combined analysis are presented in Tables C.16, C.17, and C.18.

Table C.16: Results for the combined analysis for the infill data set with events above between 0.1 and 0.2 EeV.

Results for combined analysis - Infill data set - 0.1 EeV $< E \geq$ 0.2 EeV			
Class	**Number of targets**	***P*-value (unweighted)**	***P*-value (weighted)**
msec PSRs	90	0.23	0.52
γ-ray PSRs	136	0.65	0.92
LMXB	89	0.66	0.77
HMXB	45	0.21	0.84
H.E.S.S. PWN	11	0.20	0.086
H.E.S.S. other	11	0.61	0.75
H.E.S.S. UNID	16	0.72	0.64
Microquasars	11	0.27	0.25
Magnetars	23	0.81	0.53
Gal. Center	1	0.72	0.72

Table C.17: Results for the combined analysis for the infill data set with events between 0.2 and 0.3 EeV.

Results for combined analysis - Infill data set - 0.2 EeV $E \geq$ 0.3 EeV			
Class	**Number of targets**	***P*-value (unweighted)**	***P*-value (weighted)**
msec PSRs	90	0.37	0.96
γ-ray PSRs	136	0.87	0.84
LMXB	89	0.95	0.34
HMXB	45	0.69	0.82
H.E.S.S. PWN	11	0.031	0.0068
H.E.S.S. other	11	0.34	0.56
H.E.S.S. UNID	16	0.72	0.67
Microquasars	11	0.35	0.20
Magnetars	23	0.93	1.0
Gal. Center	1	0.066	0.063

Table C.18: Results for the combined analysis for the infill data set with events above 0.3 EeV.

Results for combined analysis - Infill data set - $E \geq$ 0.3 EeV			
Class	**Number of targets**	P**-value (unweighted)**	P**-value (weighted)**
msec PSRs	90	0.43	0.21
γ-ray PSRs	136	0.95	0.46
LMXB	89	0.022	0.68
HMXB	45	0.34	0.59
H.E.S.S. PWN	11	0.67	0.68
H.E.S.S. other	11	0.65	0.41
H.E.S.S. UNID	16	0.072	0.22
Microquasars	11	0.0084	0.037
Magnetars	23	0.82	0.76
Gal. Center	1	0.68	0.68

APPENDIX D - ADDITIONAL RESULTS: PROBABILITY DENSITY METHOD

Since we did not identify any clear evidence of a neutron flux coming from any of the tested targets, we reported the results for the cumulative data sets[1] in Chapter 11, and we present the results for the other energy ranges in this appendix for the targeted search using the probability density method.

D.1 Vertical data set

In this section, we report the additional results for the vertical data set.

D.1.1 The most significant target in each target set

The tables D.1, D.2, and D.3 present the results for the most significant target in each target set for the vertical data set. The most significant target is the one with the smallest individual p-value. The tables show the position of the candidate source, the observed and expected number of events inside the target region, and the upper limit on the flux of neutrons and on the energy flux, in addition to the p-value and the penalized p-value.

[1] Cumulative data sets are the ones with events above 1 EeV for the vertical and inclined data sets and 0.1 EeV for the infill data set.

Table D.1: Results for the most significant target in each target set for the vertical data set and events with energy between 1 and 2 EeV.

Results for the targeted search - vertical data set - 1 EeV $< E \geq$ 2 EeV								
Class	**RA [deg]**	**Dec [deg]**	**Observed ρ [deg^{-2}]**	**Expected ρ [deg^{-2}]**	**Flux U.L. [km^{-2} yr^{-1}]**	**E-flux U.L. [eV cm^{-2} s^{-1}]**	**p-value**	**p-value (penalized)**
msec PSRs	284.56	−54.34	101.64	97.15	0.011	0.081	0.036	0.99
γ-ray PSRs	296.64	−54.06	105.01	97.25	0.015	0.11	0.00080	0.13
LMXB	129.35	−42.90	95.85	91.80	0.012	0.085	0.038	0.97
HMXB	195.32	−61.60	103.20	97.58	0.012	0.086	0.016	0.56
H.E.S.S. PWN	154.50	−58.92	102.07	97.33	0.011	0.080	0.033	0.30
H.E.S.S. other	288.40	4.93	46.74	44.22	0.012	0.089	0.10	0.80
H.E.S.S. UNID	286.79	8.50	39.56	37.62	0.012	0.085	0.15	0.99
Microquasars	253.75	−40.00	93.64	90.59	0.011	0.078	0.092	0.71
Magnetars	237.73	−54.31	99.79	96.66	0.0096	0.070	0.10	0.94
Gal. Center	266.42	−29.01	80.05	83.88	0.0046	0.033	0.96	0.96

Table D.2: Results for the most significant target in each target set for the vertical data set and events with energy between 2 and 3 EeV.

Results for the targeted search - vertical data set - 2 EeV $< E \leq$ 3 EeV								
Class	**RA [deg]**	**Dec [deg]**	**Observed ρ [deg^{-2}]**	**Expected ρ [deg^{-2}]**	**Flux U.L. [km^{-2} yr^{-1}]**	**E-flux U.L. [eV cm^{-2} s^{-1}]**	**p-value**	**p-value (penalized)**
msec PSRs	284.90	3.22	11.86	8.50	0.0048	0.035	0.0038	0.42
γ-ray PSRs	284.45	2.77	12.66	8.62	0.0053	0.039	0.0012	0.18
LMXB	267.02	−24.78	16.77	14.19	0.0036	0.027	0.024	0.90
HMXB	98.83	5.55	10.89	7.91	0.0045	0.033	0.0072	0.31
H.E.S.S. PWN	279.41	−6.95	12.55	10.84	0.0032	0.023	0.079	0.60
H.E.S.S. other	259.49	−37.44	18.59	15.85	0.0037	0.027	0.021	0.28
H.E.S.S. UNID	284.40	2.97	12.35	8.57	0.0051	0.037	0.0022	0.060
Microquasars	262.75	−26.00	15.51	14.36	0.0027	0.019	0.18	0.93
Magnetars	245.69	−49.85	19.21	16.72	0.0030	0.022	0.040	0.64
Gal. Center	266.42	−29.01	13.87	14.81	0.0015	0.011	0.77	0.77

Table D.3: Results for the most significant target in each target set for the vertical data set and events with energy above 3 EeV.

Results for the targeted search - vertical data set - $E \geq 3$ EeV								
Class	**RA [deg]**	**Dec [deg]**	**Observed ρ [deg^{-2}]**	**Expected ρ [deg^{-2}]**	**Flux U.L. [km^{-2} yr^{-1}]**	**E-flux U.L. [eV cm^{-2} s^{-1}]**	**p-value**	**p-value (penalized)**
msec PSRs	264.45	−8.19	11.57	7.53	0.0025	0.018	0.0098	0.75
γ-ray PSRs	238.92	−29.14	14.31	9.99	0.0024	0.018	0.0082	0.75
LMXB	117.14	−67.75	16.64	11.93	0.0017	0.013	0.016	0.78
HMXB	283.88	−2.61	9.94	6.74	0.0022	0.016	0.029	0.78
H.E.S.S. PWN	281.60	−2.97	8.51	6.83	0.0016	0.012	0.14	0.81
H.E.S.S. other	81.26	−69.64	14.80	12.08	0.0013	0.0093	0.10	0.80
H.E.S.S. UNID	284.40	2.97	8.34	5.81	0.0021	0.015	0.056	0.80
Microquasars	237.50	−56.07	12.65	11.45	0.0012	0.0086	0.25	0.98
Magnetars	286.81	9.32	6.87	4.69	0.0020	0.014	0.072	0.85
Gal. Center	266.42	−29.01	9.23	9.98	0.00089	0.0065	0.66	0.66

D.1.2 Analysis combining targets

The results for the combined analysis are presented in Tables D.4, D.5, and D.6.

Table D.4: Results for the combined analysis for the vertical data set with events between 1 and 2 EeV.

Results for combined analysis - Vertical data set - 1 EeV $< E \leq$ 2 EeV			
Class	**Number of targets**	***P*-value (unweighted)**	***P*-value (weighted)**
msec PSRs	142	0.98	0.81
γ-ray PSRs	167	0.88	0.0039
LMXB	95	0.97	0.59
HMXB	52	0.91	0.19
H.E.S.S. PWN	11	0.72	0.85
H.E.S.S. other	15	0.84	0.87
H.E.S.S. UNID	28	1.0	1.0
Microquasars	13	0.51	0.54
Magnetars	25	1.0	0.95
Gal. Center	1	0.96	0.96

Table D.5: Results for the combined analysis for the vertical data set with events between 2 and 3 EeV.

Results for combined analysis - Vertical data set - 2 $< E \leq$ 3 EeV			
Class	**Number of targets**	***P*-value (unweighted)**	***P*-value (weighted)**
msec PSRs	142	0.029	0.097
γ-ray PSRs	167	0.13	0.91
LMXB	95	0.32	0.30
HMXB	52	0.61	0.98
H.E.S.S. PWN	11	0.74	0.054
H.E.S.S. other	15	0.66	0.80
H.E.S.S. UNID	28	0.40	0.40
Microquasars	13	0.83	0.59
Magnetars	25	0.70	0.96
Gal. Center	1	0.77	0.77

Table D.6: Results for the combined analysis for the vertical data set with events above 3 EeV.

Results for combined analysis - Vertical data set - $E \geq 3$ EeV			
Class	**Number of targets**	**P-value (unweighted)**	**P-value (weighted)**
msec PSRs	142	0.57	0.87
γ-ray PSRs	167	0.86	0.24
LMXB	95	0.84	0.34
HMXB	52	0.76	0.62
H.E.S.S. PWN	11	0.74	0.87
H.E.S.S. other	15	0.35	0.64
H.E.S.S. UNID	28	0.030	0.087
Microquasars	13	0.82	0.60
Magnetars	25	0.66	0.69
Gal. Center	1	0.66	0.67

D.2 Inclined data set

In this section, we present the results for the inclined data set.

D.2.1 The most significant target in each target set

We report in Tables D.7, D.8, and D.9 the results for the most significant target in each target set for the inclined data set.

Table D.7: Results for the most significant target in each target set for the inclined data set and events with energy between 1 and 2 EeV.

Results for the targeted search - Inclined data set - 1 EeV < $E \geq$ 2 EeV								
Class	**RA [deg]**	**Dec [deg]**	**Observed ρ [deg^{-2}]**	**Expected ρ [deg^{-2}]**	**Flux U.L. [km^{-2} yr^{-1}]**	**E-flux U.L. [eV cm^{-2} s^{-1}]**	**p-value**	**p-value (penalized)**
msec PSRs	270.36	−32.18	8.68	4.06	0.048	0.35	0.00030	0.051
γ-ray PSRs	285.39	−1.42	6.49	3.76	0.036	0.26	0.0095	0.83
LMXB	201.11	−63.22	14.70	9.96	0.023	0.17	0.0062	0.46
HMXB	195.49	−63.97	17.04	10.85	0.025	0.18	0.00070	0.038
H.E.S.S. PWN	298.26	29.48	8.90	7.49	0.017	0.12	0.18	0.92
H.E.S.S. other	276.56	−14.85	5.16	3.68	0.027	0.20	0.086	0.76
H.E.S.S. UNID	288.68	11.72	6.70	4.33	0.030	0.22	0.025	0.56
Microquasars	284.67	22.66	8.94	6.01	0.027	0.20	0.020	0.25
Magnetars	281.23	−2.95	4.96	3.74	0.024	0.18	0.13	0.97
Gal. Center	266.42	−29.01	4.71	3.95	0.020	0.15	0.24	0.24

Table D.8: Results for the most significant target in each target set for the inclined data set and events with energy between 2 and 3 EeV.

Results for the targeted search - Inclined data set - 2 EeV < $E \leq$ 3 EeV								
Class	**RA [deg]**	**Dec [deg]**	**Observed ρ [deg^{-2}]**	**Expected ρ [deg^{-2}]**	**Flux U.L. [km^{-2} yr^{-1}]**	**E-flux U.L. [eV cm^{-2} s^{-1}]**	**p-value**	**p-value (penalized)**
msec PSRs	293.39	−62.20	7.92	4.47	0.0038	0.028	0.017	0.95
γ-ray PSRs	309.90	−56.29	7.66	3.41	0.0057	0.042	0.0024	0.36
LMXB	142.33	−31.38	4.96	2.07	0.0066	0.048	0.0067	0.49
HMXB	223.21	−59.82	7.05	3.88	0.0041	0.030	0.017	0.60
H.E.S.S. PWN	279.41	−6.95	3.78	1.88	0.0056	0.041	0.035	0.37
H.E.S.S. other	287.78	9.09	3.54	2.12	0.0045	0.033	0.084	0.75
H.E.S.S. UNID	286.79	8.50	3.87	2.10	0.0051	0.037	0.053	0.83
Microquasars	248.50	−47.43	3.92	2.59	0.0038	0.027	0.12	0.82
Magnetars	162.53	−59.89	8.40	3.92	0.0051	0.037	0.0016	0.041
Gal. Center	266.42	−29.01	2.03	2.02	0.0027	0.019	0.45	0.45

Table D.9: Results for the most significant target in each target set for the inclined data set and events with energy above 3 EeV.

Results for the targeted search - Inclined data set - $E \geq 3$ EeV								
Class	**RA [deg]**	**Dec [deg]**	**Observed ρ [deg^{-2}]**	**Expected ρ [deg^{-2}]**	**Flux U.L. [km^{-2} yr^{-1}]**	**E-flux U.L. [eV cm^{-2} s^{-1}]**	**p-value**	**p-value (penalized)**
msec PSRs	305.50	25.00	9.05	3.89	0.0029	0.021	0.0071	0.71
γ-ray PSRs	177.99	−61.14	11.67	3.70	0.0034	0.025	0.0010	0.17
LMXB	259.70	−32.18	5.26	1.83	0.0035	0.026	0.014	0.74
HMXB	266.19	−27.23	4.45	1.74	0.0032	0.023	0.032	0.83
H.E.S.S. PWN	279.41	−6.95	2.97	1.66	0.0022	0.016	0.14	0.85
H.E.S.S. other	81.26	−69.64	10.46	5.74	0.0018	0.013	0.027	0.36
H.E.S.S. UNID	292.15	17.78	6.35	2.33	0.0035	0.025	0.0075	0.22
Microquasars	248.50	−47.43	5.32	2.32	0.0027	0.020	0.033	0.37
Magnetars	275.57	−16.07	5.10	1.65	0.0038	0.028	0.0074	0.18
Gal. Center	266.42	−29.01	1.98	1.77	0.0014	0.010	0.36	0.36

D.2.2 Analysis combining targets

The results for the combined analysis are presented in Tables D.10, D.11, and D.12.

Table D.10: Results for the combined analysis for the inclined data set with events between 1 and 2 EeV.

Results for combined analysis - Inclined data set - 1 EeV $< E \leq$ 2 EeV			
Class	**Number of targets**	**P-value (unweighted)**	**P-value (weighted)**
msec PSRs	175	0.12	0.11
γ-ray PSRs	187	0.33	0.16
LMXB	99	0.72	0.29
HMXB	55	0.46	0.44
H.E.S.S. PWN	13	0.93	0.89
H.E.S.S. other	16	0.97	0.95
H.E.S.S. UNID	33	0.014	0.049
Microquasars	14	0.46	0.92
Magnetars	26	0.89	0.95
Gal. Center	1	0.24	0.24

Table D.11: Results for the combined analysis for the inclined data set with events between 2 and 3 EeV.

Results for combined analysis - Inclined data set - 2 $< E \leq$ 3 EeV			
Class	**Number of targets**	**P-value (unweighted)**	**P-value (weighted)**
msec PSRs	175	0.21	0.63
γ-ray PSRs	187	0.072	0.16
LMXB	99	0.48	0.77
HMXB	55	0.46	0.12
H.E.S.S. PWN	13	0.41	0.068
H.E.S.S. other	16	0.73	0.84
H.E.S.S. UNID	33	0.47	0.65
Microquasars	14	0.57	0.74
Magnetars	26	0.49	0.35
Gal. Center	1	0.45	0.45

Table D.12: Results for the combined analysis for the inclined data set with events above 3 EeV.

Results for combined analysis - Inclined data set - $E \geq 3$ EeV			
Class	**Number of targets**	**P-value (unweighted)**	**P-value (weighted)**
msec PSRs	175	0.31	0.87
γ-ray PSRs	187	0.78	0.66
LMXB	99	0.59	0.22
HMXB	55	0.71	0.58
H.E.S.S. PWN	13	0.88	0.22
H.E.S.S. other	16	0.18	0.056
H.E.S.S. UNID	33	0.066	0.14
Microquasars	14	0.74	0.31
Magnetars	26	0.24	0.95
Gal. Center	1	0.36	0.36

D.3 Infill data set

In this section, we report the additional results for the infill data set.

D.3.1 The most significant target in each target set

We report in Tables D.13, D.14, and D.15 the results for the most significant target in each target set for the infill data set.

Table D.13: Results for the most significant target in each target set for the infill data set and events with energy between 0.1 and 0.2 EeV.

Results for the targeted search - Infill data set - 0.1 EeV < $E \geq$ 0.2 EeV								
Class	**RA [deg]**	**Dec [deg]**	**Observed ρ [deg^{-2}]**	**Expected ρ [deg^{-2}]**	**Flux U.L. [km^{-2} yr^{-1}]**	**E-flux U.L. [eV cm^{-2} s^{-1}]**	**p-value**	**p-value (penalized)**
msec PSRs	280.76	−14.80	73.08	66.04	3.4	25.0	0.0022	0.18
γ-ray PSRs	274.29	−17.70	78.72	70.14	3.6	27.0	0.00040	0.053
LMXB	273.63	−17.16	77.44	69.40	3.6	26.0	0.00080	0.069
HMXB	170.31	−60.62	90.32	84.38	2.5	18.0	0.018	0.55
H.E.S.S. PWN	98.16	−17.37	73.72	69.63	2.4	18.0	0.049	0.43
H.E.S.S. other	276.56	−14.85	68.50	66.06	2.0	15.0	0.15	0.84
H.E.S.S. UNID	197.31	−5.49	52.56	50.01	2.4	18.0	0.11	0.85
Microquasars	274.88	−16.42	72.64	68.36	2.5	18.0	0.043	0.39
Magnetars	162.53	−59.89	89.58	85.02	2.2	16.0	0.049	0.68
Gal. Center	266.42	−29.01	83.39	82.77	1.4	10.0	0.41	0.41

Table D.14: Results for the most significant target in each target set for the infill data set and events with energy between 0.2 and 0.3 EeV.

Results for the targeted search - Infill data set - 0.2 EeV < E ≥ 0.3 EeV								
Class	**RA [deg]**	**Dec [deg]**	**Observed ρ [deg^{-2}]**	**Expected ρ [deg^{-2}]**	**Flux U.L. [km^{-2} yr^{-1}]**	**E-flux U.L. [eV cm^{-2} s^{-1}]**	**p-value**	**p-value (penalized)**
msec PSRs	284.57	−22.28	18.60	15.66	0.66	4.8	0.029	0.93
γ-ray PSRs	69.32	−47.25	23.33	18.79	0.74	5.4	0.0050	0.49
LMXB	255.71	−48.79	22.37	18.83	0.64	4.7	0.020	0.83
HMXB	116.85	−53.33	22.03	18.96	0.58	4.2	0.037	0.82
H.E.S.S. PWN	282.23	−0.04	13.76	9.79	1.2	8.5	0.00060	0.0066
H.E.S.S. other	81.26	−69.64	21.45	18.04	0.64	4.7	0.021	0.20
H.E.S.S. UNID	279.36	−6.58	14.04	11.84	0.69	5.1	0.051	0.57
Microquasars	255.50	−48.00	22.13	18.79	0.63	4.6	0.025	0.25
Magnetars	274.71	−15.99	17.36	14.25	0.73	5.3	0.019	0.36
Gal. Center	266.42	−29.01	18.35	16.86	0.49	3.6	0.17	0.17

Table D.15: Results for the most significant target in each target set for the infill data set and events with energy above 0.3 EeV.

Results for the targeted search - Infill data set - $E \geq 0.3$ EeV								
Class	**RA [deg]**	**Dec [deg]**	**Observed ρ [deg^{-2}]**	**Expected ρ [deg^{-2}]**	**Flux U.L. [km^{-2} yr^{-1}]**	**E-flux U.L. [eV cm^{-2} s^{-1}]**	**p-value**	**p-value (penalized)**
msec PSRs	201.68	−47.50	16.09	11.80	0.44	3.2	0.0094	0.57
γ-ray PSRs	273.35	−12.77	13.48	8.63	0.58	4.3	0.0012	0.15
LMXB	256.56	−43.04	17.06	11.67	0.51	3.7	0.0016	0.13
HMXB	190.71	−63.06	15.94	12.01	0.40	2.9	0.018	0.56
H.E.S.S. PWN	277.85	−9.90	10.42	8.22	0.39	2.8	0.072	0.56
H.E.S.S. other	84.00	−67.59	14.47	11.86	0.32	2.3	0.073	0.57
H.E.S.S. UNID	273.34	−12.69	13.22	8.62	0.57	4.2	0.0018	0.028
Microquasars	275.50	−37.02	15.50	11.39	0.45	3.3	0.0096	0.10
Magnetars	15.18	−72.19	14.61	11.70	0.34	2.5	0.057	0.74
Gal. Center	266.42	−29.01	11.45	10.66	0.26	1.9	0.30	0.30

D.3.2 Analysis combining targets

The results for the combined analysis are presented in Tables D.16, D.17, and D.18.

Table D.16: Results for the combined analysis for the infill data set with events between 0.1 and 0.2 EeV.

Results for combined analysis - Infill data set - 0.1 EeV $< E \leq$ 0.2 EeV			
Class	**Number of targets**	***P*-value (unweighted)**	***P*-value (weighted)**
msec PSRs	90	0.31	0.69
γ-ray PSRs	136	0.82	0.92
LMXB	89	0.91	0.50
HMXB	45	0.49	0.84
H.E.S.S. PWN	11	0.58	0.13
H.E.S.S. other	11	0.72	0.60
H.E.S.S. UNID	16	0.62	0.53
Microquasars	11	0.41	0.13
Magnetars	23	0.54	0.42
Gal. Center	1	0.41	0.40

Table D.17: Results for the combined analysis for the infill data set with events between 0.2 and 0.3 EeV.

Results for combined analysis - Infill data set - 0.2 EeV $< E \leq$ 0.3 EeV			
Class	**Number of targets**	***P*-value (unweighted)**	***P*-value (weighted)**
msec PSRs	90	0.74	0.96
γ-ray PSRs	136	0.93	0.82
LMXB	89	0.98	0.25
HMXB	45	0.59	0.61
H.E.S.S. PWN	11	0.037	0.018
H.E.S.S. other	11	0.12	0.72
H.E.S.S. UNID	16	0.88	0.58
Microquasars	11	0.34	0.22
Magnetars	23	0.70	0.97
Gal. Center	1	0.17	0.17

Table D.18: Results for the combined analysis for the infill data set with events above 0.3 EeV.

Results for combined analysis - Infill data set - $E \geq$ 0.3 EeV			
Class	**Number of targets**	P**-value (unweighted)**	P**-value (weighted)**
msec PSRs	90	0.64	0.40
γ-ray PSRs	136	0.86	0.56
LMXB	89	0.072	0.61
HMXB	45	0.12	0.84
H.E.S.S. PWN	11	0.34	0.66
H.E.S.S. other	11	0.63	0.36
H.E.S.S. UNID	16	0.019	0.17
Microquasars	11	0.0056	0.011
Magnetars	23	0.77	0.66
Gal. Center	1	0.30	0.30